

DEVELOPMENT OF ATLAS-GUIDED DIFFUSE OPTICAL TOMOGRAPHY TO
INVESTIGATE AGE-DEPENDENT HUMAN COGNITIVE FUNCTIONS
UNDER RISK DECISION MAKING

by

LIN LI

Presented to the Faculty of the Graduate School of
The University of Texas at Arlington in Partial Fulfillment
of the Requirements
for the Degree of

DOCTOR OF PHILOSOPHY

THE UNIVERSITY OF TEXAS AT ARLINGTON

MAY 2015

Copyright © by LIN LI

All Rights Reserved



Acknowledgements

First of all, I would like to give my sincere thanks to my supervisor Dr. Hanli Liu. She has spent a huge amount of time in the past five years to supervise my research work. She has helped me build up my scientific ability by teaching me fundamental and advanced knowledge in medical imaging and guiding me for critical thinking. She has also helped me greatly improve my scientific writing and reading skills. Moreover, she has encouraged me to explore new research ideas in conjunction with my own strength and interest.

I would like to thank Dr. Mary Cazzell for her patience and guidance during my doctoral dissertation study. She helped me start up my research project that was not within my previous training area. I also appreciate her close collaboration with our research group in the past four years, particularly I am grateful for her time and efforts spent with me on data collection, results interpretation, and detailed assistance with my writing skills.

Thanks also go to many others who have helped me during my doctoral study. My sincere appreciation goes to Dr. Li Zeng, who has guided me comprehensively in statistical analysis; to Dr. George Alexandrakis and Dr. Bohong Yuan, who have helped me with my fundamental knowledge in optical imaging and provided me with constructive feedback for my dissertation; and to Dr. Zi-jing Lin for his assistance for my image processing skills.

Finally I would like to thank my parents, my wife and other loving members of my family for their great supports during my doctoral study period.

May 15, 2015

Abstract

DEVELOPMENT OF ATLAS-GUIDED DIFFUSE OPTICAL TOMOGRAPHY TO INVESTIGATE AGE-DEPENDENT HUMAN COGNITIVE FUNCTIONS UNDER RISK DECISION MAKING

Lin Li, PhD

The University of Texas at Arlington, 2015

Supervising Professor: Hanli Liu

To better understand the age effect on neural correlates under risk decision-making stimulations, studies using advanced neuroimaging with a sufficient statistical power are desired. Diffuse optical tomography (DOT) of human brain functions is an emerging non-invasive neuroimaging technology. Compared to magnetic resonance imaging (MRI), DOT is more cost-effective, more portable, and easier to conduct studies targeting on different age groups. However, current DOT is limited by its low spatial resolution and depth accuracy. It is thus imperative to develop a technique that can improve imaging quality of DOT and be used to investigate age-dependent human brain functions under risk decision making.

My doctoral study targets the needed development with three specific aims. The first aim is to develop human brain atlas-guided diffuse optical tomography (atlas-DOT) integrated with a 3D forward modeling technique and depth compensation algorithm, which greatly improves the image quality and depth accuracy in DOT. In my second aim, I utilize statistical modeling to implement a general linear model (GLM) with atlas-DOT to obtain more accurate identification of brain activation regions under a risk decision-making protocol. A total of 100 subjects (40 young adults; 60 older adults) have

participated in my functional DOT measurements under the Balloon Analogue Risk Task (BART), a conventional risk decision-making stimulation protocol. The results indicate that age differences exist in cortical activation patterns, brain activation amplitudes, and behavior-brain function correlations. In particular, larger cortical activation with reduced amplitudes in the prefrontal cortex (PFC) are observed in older adults, not in young adults, when they face the same decision-making task. Behavior-brain function correlations indicate that young adults are more “risk-taking” while older adults tend to be more “risk-averse”. In the third aim, graph theory analysis (GTA) has been implemented with atlas-DOT to further quantify the resting-state functional brain connectivity between two age groups. Age-related differences are found in resting-state brain network metrics: Older adults show reduced global efficiency and hub numbers in prefrontal regions. My dissertation is the first study using the fDOT technique to investigate the aging and gender effect on brain responses under risk decision making, and it is also the first time to combine GTA with atlas-DOT to investigate brain network changes in young and older adults. Overall, my dissertation demonstrates the high feasibility of atlas-DOT to be used for assessment of age-related brain activations in both resting-state and under risk decision making.

Table of Contents

Acknowledgements	iii
Abstract	iv
List of Illustrations	xii
List of Tables	xviii
Chapter 1 Introduction.....	1
1.1 Age effect on brain functions	1
1.2 Modern neuroimaging techniques	2
1.3 Specific aims and dissertation outline	4
Chapter 2 Development of Atlas-guided Diffuse Optical Tomography	8
2.1 Introduction	8
2.2 Atlas-guided diffuse optical tomography with depth compensation algorithm	10
2.2.1 Strategies of atlas-guided diffuse optical tomography	10
2.2.2 Atlas-guided technique in forward problem	11
2.3 Depth compensation algorithm in atlas-fDOT	14
2.3.1 Optode arrangement	14
2.3.2 Forward Light Modeling.....	16
2.3.3 Inverse problem with depth compensation algorithm.....	17
2.4 Optimization of depth compensation parameter.....	18
2.4.1 Preliminary results of computer simulation in the brain atlas- guided model along vertical directions.	18
2.4.2 Preliminary result of simulation process to Optimize adjusted power for DCA.	19
2.5 Summary	20

Chapter 3 Assessment of Measurement Reliability of Atlas-DOT for Brain

Imaging.....	22
3.1 Introduction.....	22
3.2 A guideline to assess measurement reliability in functional brain imaging using intraclass correlation coefficient.....	24
3.2.1 Mathematical model of intraclass correlation coefficient.....	24
3.2.1.1 Unified ANOVA model	24
3.2.1.2 Six forms of ICC.....	27
3.2.1.3 ICC criteria to assess reliability of measurements.....	31
3.2.2 Addressing the Selection of ICCs.....	32
3.2.2.1 Properties of ICCs.....	32
3.2.2.2 Guidelines on ICC Selection	33
3.2.2.3 Determination of one-way model vs. two-way model	33
3.2.2.4 Determination of two-way random-effect model vs. mixed- effect model.....	34
3.2.2.5 General guidelines	36
3.3 Risk decision-making using balloon analog risk task	36
3.3.1 Introduction of balloon analog risk task.....	36
3.3.2 Development of MATLAB-based BART protocol	38
3.4 Experimental setup	41
3.4.1 Participants and paradigms.....	41
3.4.2 Data processing.....	43
3.5 Results	44
3.5.1 Hemodynamic Response under BART Stimulation	44
3.5.2 Reliability Assessment Using Intraclass Correlation Coefficient.....	47

3.6 Discussion	50
3.6.1 Simple Procedure for ICC Selection.....	50
3.6.2 Pitfalls in Test-retest Reliability Assessment.....	51
3.7 Summary	53
Chapter 4 Implement of General Linear Model in Atlas-DOT	54
4.1 Introduction	54
4.2 Implement of general linear model in atlas-guided diffuse optical tomography	55
4.2.1 General linear model	55
4.2.2 Strategies of GLM-based atlas-DOT algorithm	59
4.3 Participants and experimental setup	62
4.4 Results	64
4.4.1 Active versus Passive Mode in BART Paradigm	64
4.4.2 Gender Difference in Active Mode	65
4.4.3 Improvement of Depth Sensitivity by DCA	68
4.5 Discussion	71
4.5.1 Comparison with Previous Studies.....	72
4.5.2 Atlas-DOT in Brain Research	75
4.5.3 Limitations and future work	76
4.6 Summary	78
Chapter 5 Assessment of Age and Gender Effect on Brain Activation under Risk Decision-making.....	80
5.1 Introduction	80
5.1.1 Background and significance	80
5.1.2 Age- and gender-effect on neurocognitive functions.....	81

5.1.3 fNIRS and BART	82
5.1.4, Study aims and purpose.....	83
5.2 Material and method	83
5.2.1 Study design.....	83
5.2.2 Participants.....	84
5.2.3 Experimental set up.....	85
5.2.4 Data processing.....	87
5.2.5 Statistical analysis	89
5.3 Results.....	90
5.3.1 Participants.....	90
5.3.2 Brain maps for two phases.....	90
5.3.3 Statistical analysis for age effect.....	94
5.3.3.1 Behavioral measures	94
5.3.3.2 Brain hemodynamic responses	95
5.3.4 Statistical analysis for gender effect.....	96
5.3.4.1 Gender differences in young adults	96
5.3.4.2 Gender differences in older adults.....	97
5.3.5 Correlations between behavioral measures and hemodynamic responses	99
5.4. Discussion	101
5.4.1 Age effects.....	102
5.4.2 Gender effects.....	103
5.4.2.1 Gender effect in young adults	103
5.4.2.2 Gender effect in older adults.....	105
5.4.3 Study limitations and future work	106

5.5 Summary	107
Chapter 6 Implement of Graph Theory Analysis to Atlas-DOT to Investigate	
Age-related Brain Functional Connectivity.....	109
6.1. Introduction	109
6.1.1 Significance, backgrounds and goals.....	109
6.1.2 Characteristics of brain networks along aging	110
6.1.3 Atlas-guided diffuse optical tomography implemented with graph theory analysis.....	111
6.1.4 Study aims and purpose.....	112
6.2 Material and method.....	112
6.2.1 Participants and data acquisition.....	112
6.2.2 Data processing.....	114
6.2.3 Construction of functional brain networks	116
6.2.4 Graph theory analysis	121
6.2.5 Statistical analysis	123
6.3 Results.....	124
6.3.1 Mapping of nodes and edges	124
6.3.2 Global and small-world metrics in brain network.....	125
6.3.2.1 Global network metrics	125
6.3.2.2 Small-world functional network	126
6.3.3 Network hubs.....	127
6.4 Discussion	129
6.4.1 Graph formation in atlas-DOT	130
6.4.2 Global integration and small-world features in two age groups	131
6.4.3 Node betweenness centrality and age-related changes	132

6.5 Summary	133
Chapter 7 Summary and Future Work	135
7.1 Summary	135
7.2 Limitations and future work.....	137
Appendix A Additional Figures for Chapter 2.....	139
Appendix B Derivation of the Six Forms of ICC in Chapter 3	142
Appendix C Matlab Program for BART Protocol.....	146
Appendix D Matlab Program for 3D Imaging	167
References.....	169
Biographical Information	187

List of Illustrations

Figure 1-1 Flow chart of technological process and contents of this thesis.	5
Figure 2-1 Workflow of atlas-DOT	11
Figure 2-2 T1-weighted MRI images in: (a) sagittal, (b) axial, and (c) coronal view of the ICBM 152 brain atlas.....	12
Figure 2-3 (a) Segmentations of four ROIs, namely, scalp (blue), skull (green), gray matter (red) and white matter (yellow); (b) surface mesh generation based on the ROI segmentations, from left to right are the surface mesh of scalp, skull, gray matter, white matter, respectively.	13
Figure 2-4 Optical properties showed in volumetric meshes in different colors: scalp (green), skull (blue), gray matter (red) and white matter (yellow), respectively. (a) Stereo vision; (b) sagittal view.	14
Figure 2-5 Co-registration optodes from real space to MNI space. (a) Optodes placement in real space; (b) projected Optodes in MNI ICBM 152 head model	15
Figure 2-6 Illustration of computer simulation object in the fixed depth of 20 mm, varying γ from 0 to 3.0. From left to right showed the reconstructed object on sagittal view (upper line) and coronal view (lower line) with respect to $\gamma = 0.5, 1.0, 1.5, 2.0, 2.5$ and 3.0	19
Figure 2-7 Dependence of (a) CNR and (b) PE of reconstructed images on object depth, z , and γ for an object ($d = 15\text{mm}$). They are generated when simulations moved the object along vertical direction below the head surface, while γ value increased from 0 to 3. The dashed rectangles outline the uniform value of CNR and PE.	20
Figure 3-1 BART risk decision-making task outcomes in both active and passive modes: (a) Stop balloon inflations and collect \$\$ ["You Win!!"] or (b) Balloon explodes and lose accrued \$\$ for that balloon ["You Lose!!"].....	39

Figure 3-2 Schematic diagram depicting 15 task blocks. Each block includes an activation period (5 to 6 seconds, variable among participants) and a 15-second recovery time.	41
Figure 3-3 (a) Continuous wave (CW) fNIRS brain imaging system (Cephalogics, Ishington Univ., USA); (b) Optode placement on a participant's forehead.	42
Figure 3-4 (a) Optode locations co-registered to the ICBM152 brain template; (b) the geometry of the probe, where circles represent the detectors and crosses represent the sources.	43
Figure 3-5 Coronal, sagittal and axial view of fNIRS activation group level maps from visit 1 (red), the overlap (white), and visit 2 (yellow). Upper images show reaction areas under the "win" stimulus, while bottom images represent those under the "lose" stimulus.	45
Figure 3-6 Bar plots of mean amplitude for two visits in (a) "win" and (b) "lose" case.	46
Figure 3-7 fNIRS activation subject-specific cerebral activation maps from visit 1 (red), the overlap (white), and visit 2 (yellow). Upper images show reaction areas under the "win" stimulus, and bottom images represent those under the "lose" stimulus.	47
Figure 3-8 Flow chart of the procedure for ICC selection	51
Figure 4-1 The schematic illustrations of an experimental design of BART and the random-effect analysis. (a) A schematic of protocol and regressor design of BART. (b) Schematic diagram of two-stage random-effects analysis.	59
Figure 4-2 Procedures of GLM-based atlas-guided diffuse optical tomography	60
Figure 4-3 Experimental protocol and regressor design. (a) The BART protocol for decision-making phase (left) and reaction phase (right); (b) block design of the BART protocol; (c) illustration of regressor for the decision-making phase; (d) illustration of regressor for reaction phase.	61

Figure 4-4 Activation images generated at the group-level when performing the (a) active and (b) passive BART modes. (c) Axial and coronal views of activation maps with sliced location	64
Figure 4-5 Brain activation maps from subjects performing BART decision-making/performance phase with different genders. (a) Female win case; (b) female lose case; (c) male win case; and (d) male lose case. Threshold is set as $p < 0.01$ (FDR corrected). Notice that “R” represents the right and “L” represents the left side of the brain.	66
Figure 4-6 Activation images under BART stimulus during outcome phase. Brain activation maps in response to active BART mode when female subjects ($N = 21$) saw the outcome (a) in the “win” case, (b) in the “lose” case, and when male subjects ($N = 16$) saw the outcome (c) in the “win” case, and (d) in the “lose” case.	67
Figure 4-7 Group-level atlas-guided images of overlapped activation voxels across all participants. Shown are a axial, coronal, and sagittal views of brain activations across all participants during decision-making phase and reaction/outcome phase: (a), (c) Without DOCA and (b), (d) with DCA), respectively.....	69
Figure 5-1 Experimental protocol and regressor design. (a) The BART protocol for decision-making phase (left) and outcome phase (right); (b) block design of the BART protocol; (c) illustration of regressor for the decision-making phase; (d) illustration of regressor for outcome phase.	84
Figure 5-2 Optode probes for (a) older adults and (b) young adults. Images were plotted as the outcome of 3D co-registration.	86
Figure 5-3 Optical sensitivity matrices for (a) older adults and (b) young adults.....	87
Figure 5-4 (a) Group-level brain activations (t -maps) for phase 1; images are displayed by groups of older adults and young adults. (b) Group-level brain activations for phase 2;	

from top to bottom showed young adult-win, older adult-win, young adult-lose, and older adult-lose, respectively. Images are obtained from the voxel-wise t -map threshold at $p < 0.05$ (FDR corrected).	92
Figure 5-5 Brain activation regions for males and females in young adult (a) and older adult (b) groups. Brain activation regions for male, female, and overlaps are presented in red, yellow, and white color, respectively. Upper images showed the brain activation regions in win case for young adults (left) and older adults (right). Lower images showed the brain activation regions in lose case for young adults (left) and older adults (right)...	94
Figure 5-6 (a) Behavioral data for the age-effect analysis; (b) brain activity data for age-effect analysis. Columns showed the bar plot of mean and standard deviation (one-sided) for young-win, old-win, young-lose, and older-lose groups, respectively. **: $p < 0.001$ * $p < 0.05$	95
Figure 5-7 Gender comparisons in young adults. (a) Bar plot for means and standard deviations of behavioral data; (b) bar plot for means and standard deviations of hemodynamic data. Columns showed the mean and standard deviation (one-sided) for “young male win”, “young female win”, “young male lose,” and “young female lose” groups, respectively. **: $p < 0.001$ * $p < 0.05$	97
Figure 5-8 Gender comparisons in older adults. (a) Bar plot for means and standard deviations of behavioral data; (b) bar plot for means and standard deviations of hemodynamic data. Columns showed the bar plot of mean and standard deviation for “older male win”, “older female win”, “older male lose” and “older female lose” groups, respectively.	98
Figure 5-9 Correlation plots between the behavioral measure (AAP) and hemodynamic changes (ΔHbO) for male (blue) and females (red) in young adults (upper) and older adults (lower) groups.....	100

Figure 6-1 Experimental setup and detection regions. (a) Optical probe placement in the forehead of a participant. (b) Optodes co-registration in the ICBM 152 brain atlas. Region of detection (ROD) majorly located at frontal and prefrontal cortex, covered a 20×10×4 cm regions with 32615 voxels.	114
Figure 6-2 Region of interest (ROI) based on Automatic Anatomical Labelling (AAL). (a) Placement of 116 AAL regions with ICBM 152 brain template. (b) 34 node positions extracted based on the detected regions and AAL 116 templates.	117
Figure 6-3 (a) Illustration of temporal plots of HbO values within 10 minutes of resting state at 34 nodes. (b) The adjacency matrix generated by cross-correlation of ΔHbO values at 34 nodes; x-axis and y-axis represent the node numbers; red color represents high correlations between the temporal profiles of two nodes, while blue color represents low correlations. (c) The spatial representation of nodes and edges based on DOT measurements. (d) The binary matrix threshold by sparsity of 0.26.	120
Figure 6-4 Eight views of nodes and edges from subject 1 (in young adult group). Colors of nodes represent the different brain anatomical regions, while colors of edges represent the strength of connections between two nodes.	125
Figure 6-5 Comparison of young and older adult group in global network metrics. The plot for (a) global efficiency; (b) clustering coefficient and (c) shortest path length with respect to the sparsity from 0.05 to 5.0.	126
Figure 6-6 Small-world parameters, namely (a) normalized clustering coefficient (γ), (b) normalized characteristic path length (λ) and (c) small-worldness (σ) of young adult (blue) and older adult group (red).	127
Figure 6-7 Hubs for older adults and young adults. The hubs are grouped as nodal degree, nodal efficiency and betweenness centrality. Yellow represents the default mode	

network, light blue represents the frontal-parietal network, and dark blue represents the sensorimotor network.....	129
--	-----

List of Tables

Table 2-1 Optical properties of head tissues for modeling	13
Table 3-1 Overview of fNIRS/fMRI reliability studies using ICCs	23
Table 3-2 General data format.....	24
Table 3-3 ANOVA models as basis of ICCs	27
Table 3-4 Variance decomposition in the ANOVA models	29
Table 3-5 Definition of ICCs and computation formula	31
Table 3-6 Individual level mean ROI HbO (μM).....	47
Table 3-7 Intraclass correlation coefficients with 95% CI for assessing test-retest reliability	48
Table 3-8 ANOVA table* in the “win” case.....	49
Table 3-9 ANOVA table in the “lose” case	49
Table 4-1 Participant Demographic Information	63
Table 4-2 Activation overlapping ratio between brain and non-brain region	69
Table 5-1 Brain activation regions (ROI volume) in phase 2	94
Table 5-2 Descriptive statistics of behavioral measures (AAP) and hemodynamic responses [ΔHbO (μM)] in young and older adults.....	96
Table 5-3 Descriptive statistics of behavioral measures (AAP) and hemodynamic responses [ΔHbO (μM)] in males and females	98
Table 5-4 Correlation coefficients (r) of behavioral measures and hemodynamic amplitude changes in males and females within young and older adult groups.....	101
Table 6-1 Node positions in this study	117
Table 6-2 Regions of hubs in two age groups	128

Chapter 1

Introduction

1.1 Age effect on brain functions

Studies of age effects on brain function are recent hot topics in the field of neuroscience. Two of the major findings related to the age-effect on neuronal changes are introduced as follows. First, the prefrontal cortex (PFC) is observed as the most affected region by the age-related decline compared to other parts of the brain, such as the temporal lobe, hippocampus and striatum [1], [2]. Second, theories of neurocognitive aging suggests a compensation mechanism in older adults; the brain could recruit additional neural cells in the neighboring functional regions to maintain the work load as seen in young adults [3]–[8]. These age-effects are observed on high-order brain functions, such as memory, learning, information processing, and decision making [9]. More specifically, a review study indicate that older adults engage more expansive areas of the PFC than young adults across a variety of externally-driven cognitive tasks [4]. Researchers of fMRI studies under gambling simulations also indicate that older adults exhibit increased neural activations in either the superior PFC, left orbitofrontal cortex (OFC) [5] and bilateral ventromedial prefrontal cortex (vmPFC;[6]).

However, the neurophysiological mechanisms led by age-related changes, such as risk decision-making [10], economic decision-making [11] and outcome-based learning [12], are still largely unexplored. It is known that the risk decision-making is a complex neuronal process, which is involved with multi-function, such as emotion, learning and decision. For instance, it has been found that emotional regulation, highly related to OFC (or equally vmPFC) and dorsolateral prefrontal cortex (DLPFC), dominated neurocognitive differences in risk decision making [11]–[13]. Risk-averse performances or risk avoidance behavior are observed in older adults than young adults, where a

Decision-Gamble task has been performed to 177 health participants (age from 17 to 77 years) and reveal that the increase of age is associated with reduction of risk tolerance factor (risk behavior to judge personal risk). In dealing with the complexity of age-effect under risk decision-making process, it is thus critically demanded to perform rigorous investigations on the neural correlates between behaviors and brain activations. Moreover, it is also desire to introduce an efficient neuroimaging tool to obtain the adequate study power in assessment of the age-effects.

1.2 Modern neuroimaging techniques

Functional brain imaging methods have been dramatically developed in recent decades. Neuroimaging tools such as functional magnetic resonance imaging (fMRI), functional near-infrared spectroscopy (fNIRS), position-emission tomography (PET) and electroencephalography (EEG) or magnetoencephalography (MEG) are the major modalities for functional brain imaging. Each of these modalities has its benefits and drawbacks. The current gold standard for functional neuroimaging, namely fMRI, has limitations for older adults due to restrictive body confinement and contraindications based on certain health conditions. Functional diffuse optical tomography (fDOT) of the human brain is an emerging functional neuroimaging technology that allows non-invasive imaging of human brain functions by injecting near infrared (NIR) light into the human head and taking optical measurements on the human scalp. Compared to fMRI, fDOT has the advantages of cost efficiency, portability, and comprehensive hemodynamic imaging capability. However, current fDOT technique is insufficient in its spatial resolution, limited by its depth penetration and a lack of reliable and repeatable functional mapping. It is thus a desire to develop a fDOT technique that can significantly improve the image quality in lateral resolution and depth accuracy.

Data analysis methods also need to be improved to fit for the nature of the neuropsychological and neurobiological signals obtained from brain activation. A classical way of defining brain activation induced by stimulation tasks in fDOT [14]–[16] involves the following steps: (1) Defining the maximum activation period in a time series of oxygenated hemoglobin changes (ΔHbO) from the fNIRS measurements. (2) Reconstructing temporally averaged fDOT images over the chosen activation period. (3) Determining the region of brain activation by full width at half maximum (FWHM) in reconstructed images. However, the method stated above has an obvious drawback in that the maximum activation or post-activation period has to be subjectively defined without much statistical or mathematical basis. To overcome this limitation, many research groups [17]–[22] have followed an analysis method commonly utilized by fMRI researchers, namely, the general linear model (GLM) based analysis. It examines whether or not the experimental fNIRS data and a designed linear model are matched over the entire experimental time course. This approach rests on a physiology-based principle or model that hemodynamic signals measured in response to brain stimulation result from a convoluted effect between the stimulation task and hemodynamic response function (HRF), where the latter two functions are already given. Thus, with GLM, there is no need to select the activation and/or post-activation period in order to determine the activation regions in the brain.

Another method which critically improved the understanding of neurobiological signals is the new, multidisciplinary approach known as graph theory analysis (GTA) [23], [24]. This approach describes properties of complex brain networks by quantifying topologies of their respective network characteristics. Evidence accumulated by investigators show that functional networks throughout the brain are necessary, particularly for higher cognitive functions such as memory, planning and decision-making

[22], [25], [26]. It is more and more acknowledged that the brain should be conceived as a set of complex networks of dynamical systems. For instance, consider that the brain consists of numerous functional interactions between local and distant areas [23], [27], [28]. As people aging, alterations in human brain structure and function happen, and these changes are associated with the alteration in cognitive function[29]–[34]. Understanding of these the aging process of the brain also require an understanding changes in brain networks, network patterns and characteristics during the process. Thus, it is critically important to implement and utilize GTA with fDOT in order to further understand the functional brain network changes in aging process.

1.3 Specific aims and dissertation outline

The goal of my dissertation is to develop an efficient tool that can enhance the current functional DOT method in order to extensively assess the neural correlates of age-related brain response changes under risk decision making and to investigate functional brain networks between young and older adults. To accomplish the goals, three aims are listed as follows:

Aim 1: to develop an atlas-guided, finite element method (FEM)-based human brain model and integrate it with depth-compensated functional diffuse optical tomography (atlas-DOT).

Aim 2: to combine newly developed atlas-DOT with a general linear model (GLM) to investigate age effects under a risk decision-making paradigm.

Aim 3: to utilize graph theory analysis with atlas-DOT to investigate the age-dependent, complex brain networks in resting state.

To better illustrate the aims and respective Chapters, a flow chart is presented in Figure 1-1 to demonstrate the whole technological process of this dissertation.

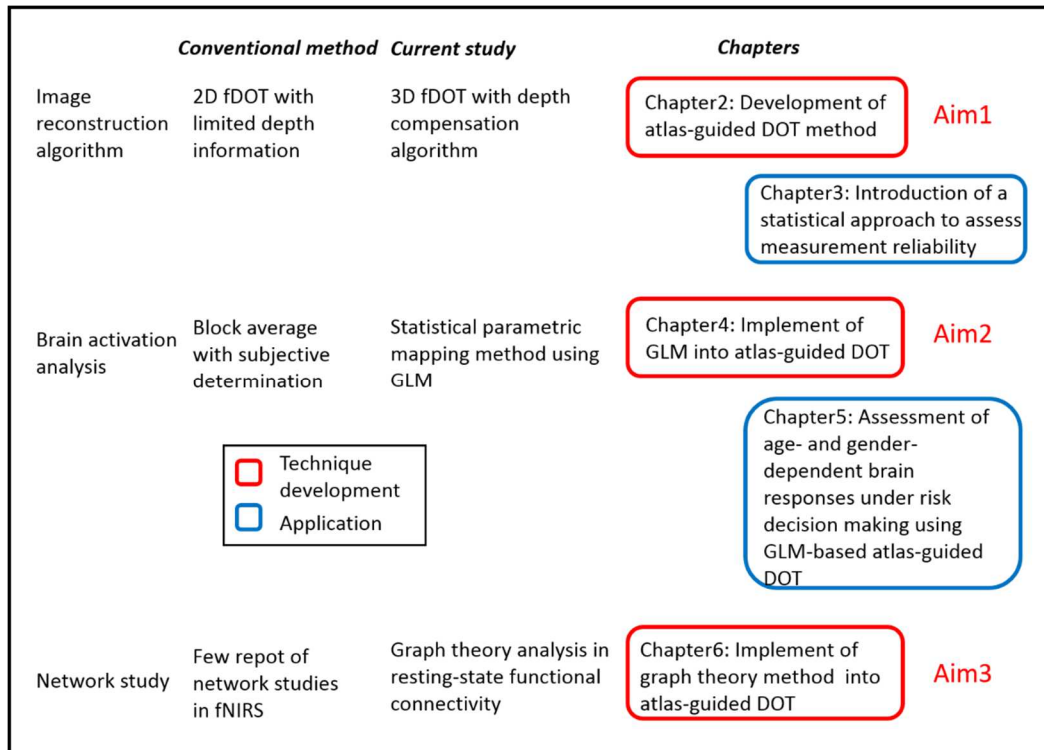


Figure 1-1 Flow chart of technological process and contents of this thesis.

According to the points discussed above, this dissertation is divided into four parts. In the first part of my work (Chapter 2), the major technique in this dissertation, namely, atlas-guided diffuse optical tomography (atlas-DOT), is developed. With two procedures, atlas-DOT is able to improve the image quality and depth accuracy in diffuse optical imaging. Specifically, a forward brain modeling has been introduced by using a computationally efficient finite element method (FEM) with a depth compensation algorithm (DCA). The inverse imaging reconstruction is established by utilizing the forward brain modeling. Computer simulations are conducted to test the quality of this algorithm based on calculations of contrast to noise ratio (CNR) and position error (PE). Preliminary results demonstrate that atlas-DOT is capable of imaging the hemodynamic

responses up to 25 mm below the human scalp surface with improved image resolution and localization accuracy.

In the second part of my dissertation (Chapter 3), an inter-test reliability or reproducibility study with atlas-DOT is performed in nine health adults under the Balloon Analogue Risk Task (BART). BART is a computer-based program that has been widely used to evoke the brain activation under risk decision making. I also reviewed and summarized six forms of the intraclass correlation coefficients (ICCs) for neuroimaging applications as well as introduced a guideline to properly use ICC for assessment of the test-retest reliability in the functional brain imaging field. Results on brain activation patterns and amplitudes reveal moderate to high reproducibility for atlas-DOT in assessment of brain responses under risk decision making.

In the third part of my dissertation (Chapter 4 & 5), a general linear model (GLM) is implemented with atlas-DOT to investigate age- and gender- dependent brain responses under BART stimulation. Specifically, two age groups of participants (40 young adults, age from 25 to 42 years; 60 older adults, age from 65 to 92 years) has been measured for their prefrontal responses under the two-phase BART stimulation. The results indicate that age differences exist in cortical activation patterns, brain activation amplitudes, and behavior-brain function correlations. Results also show the presence of gender effect within two age groups. Consistent findings with other studies reveal the feasibility of atlas-DOT for assessment of age-related changes under risk decision-making stimulation.

In the last part of my work (Chapter 6), a more advanced technique, namely, graph theory analysis (GTA), is implemented with atlas-DOT to further study the brain network changes in resting state functional connectivity between the young and older adults. Both age groups reveal a small-worldness characteristic. Older adults also show

reduced global efficiency and hub numbers in prefrontal regions, which is consistent with results from other functional brain imaging studies. This is the first study using the fDOT technique to investigate the aging and gender effect on brain responses under risk decision making, and it is also the first time to combine GTA with atlas-DOT to investigate brain network changes in young and older adults.

Chapter 2

Development of Atlas-guided Diffuse Optical Tomography

2.1 Introduction

Functional near-infrared spectroscopy (fNIRS) is a non-invasive imaging technique which measures the hemodynamic changes resulting from brain activity while the subject performs different mental tasks. Light around the 650 to 900 nm (also called 'optical window') wavelength can penetrate several centimeters into biological tissue due to low absorption properties within this wavelength range [35]. Functional NIRS uses this near-infrared light to monitor local changes of blood supply due to cortical activation by measuring changes in light absorption. These absorption changes are mainly caused by concentration changes of oxygenated (HbO), and deoxygenated (Hb), and total (HbT) hemoglobin. It has been shown that fNIRS has great potential to be used in neurological and psychiatric applications [36].

Based on different image formation methodology, fNIRS provides two types of brain images: topographic and tomographic images. The former uses pairs of sources and detectors to formulate spatially smoothed, two dimensional (2D) maps of hemodynamic changes by linearly interpolating the channel-wise fNIRS data [46]. The latter, named diffuse optical tomography (DOT), also uses multiple source-detector measurements to capture cortical activities during mental tasks [14], [15], [39], [40]. Diffuse optical tomography is classified into three modes based on the type of signal measured: Time domain (TD), frequency domain (FD) and continuous wave (CW). In my dissertation, only the CW mode is introduced based on the available facilities in my lab. Image reconstruction in DOT involves both the forward and the inverse problems. The forward problem uses the diffusion equation to predict the distribution of reemitted light on the basis of presumed parameters for both the light source and the object. The

inverse problem uses the forward problem to reconstruct the distributions of the optical properties of the object from a measured data set.

However, DOT has a number of limitations. Specifically, DOT is known for its insufficient spatial resolution, limited depth penetration, restricted field of view, and lack of reliable and repeatable functional mapping [41]. The need for the development of a more advanced fDOT technology that can provide three-dimensional (3D) tomographic imaging capability with improved lateral resolution and localization accuracy is highly demanding. A model-based approach combined with the depth compensation method can thus spatially improve the DOT image quality and depth accuracy. The focus of this chapter is on a novel approach to the development and application of atlas-DOT.

To address the spatial limitation in DOT, several studies have reconstructed DOT images using MRI-based 3D human head structure templates [41]–[43] to greatly improve 3D visualization and spatial localization/identification of activated cortical regions under respective stimulations [40], [44]. For the depth limitation, several DOT reconstruction algorithms including hard-prior usage [42], spatial variant regularization (SVR) [45], [46], and depth-compensation algorithm (DCA) [47] have been developed to compensate or counter-balance the sensitivity of DOT which exponentially attenuates with the increase of penetration depth in order to reduce the localization error of brain activation with respect to the depth. Although solutions to each of the given three limitations are explored in the positive directions respectively, only a small number of publications have reported a convincing methodology to improve or minimize all of the limitations.

2.2 Atlas-guided diffuse optical tomography with depth compensation algorithm

2.2.1 *Strategies of atlas-guided diffuse optical tomography*

As mentioned in 2.1, the current DOT routines are restricted by its low-resolution and deficiency of depth information. In this chapter, an atlas-guided, depth compensated diffuse optical technique is introduced to overcome the shortage of spatial resolution and depth information of current DOT algorithm. Figure 2-1 demonstrates the workflow of the atlas-DOT. A brief description of the workflow is as follows: the three main steps involved are differentiated using colors. The first main step is three-dimensional (3D) modelling (marked in black color), which is divided into four sub-steps. Details of 3D modeling are discussed in chapter 2.2.2. The second main step is the forward problem (marked in dark blue), in which the 3D model generated in the first step is used in computing the forward model of diffuse theory using finite-element method. Details of forward problem are discussed in chapter 2.2.3. The third main step is inverse problem, in which the results of the forward problem (is adapted) and the depth compensation algorithm is applied. Details of inverse problem are discussed in chapter 2.2.4. In the last part (chapter 2.2.5) of this chapter, a simulation is performed in order to optimize the DCA parameter by comparing the position error (PE) and contrast-to-noise ratio (CNR) in the reconstructed images at different depths.

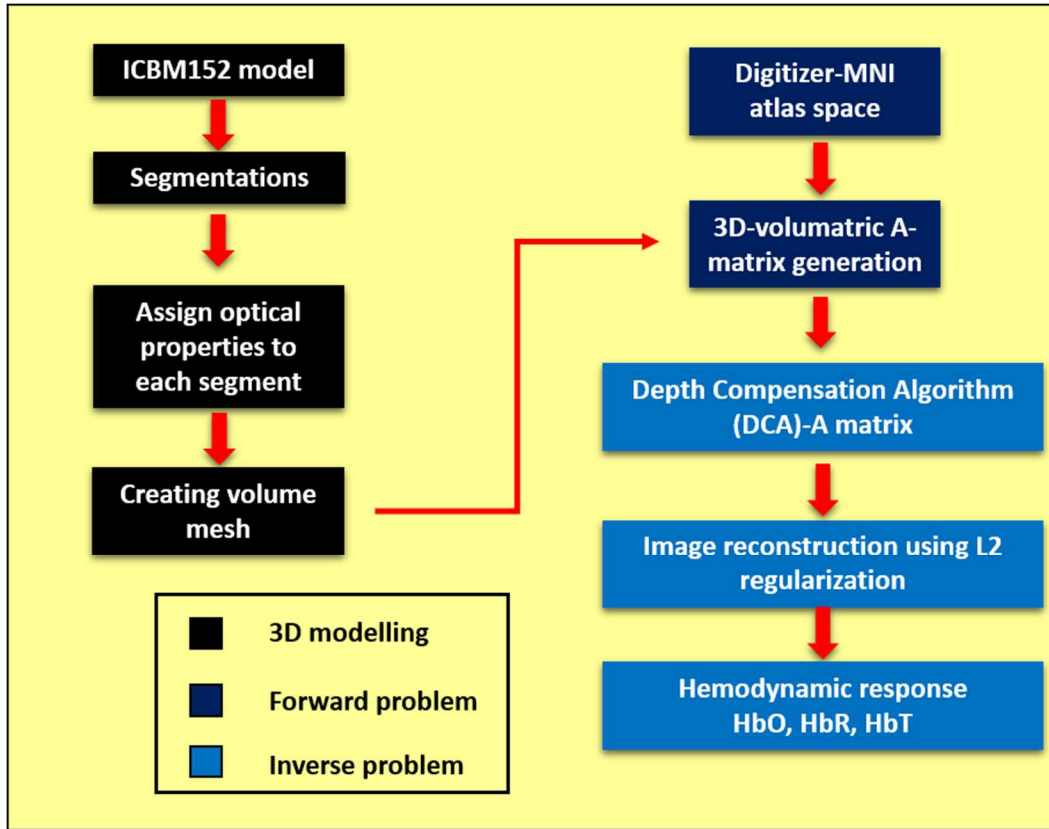


Figure 2-1 Workflow of atlas-DOT

2.2.2 Atlas-guided technique in forward problem

Spatial resolution can be enhanced by meticulously applying a voxel-based template as the medium in forward calculation [44], [48]. In this chapter, the ICBM (International Consortium for Brain Mapping) 152 MNI (Montreal Neurological Institution) template is selected as the atlas of the human head. The ICBM152 template is the most common stereotaxic platform for tomographic functional brain mapping method [37]. ICBM152 template was obtained by averaging the scans of 152 normal subjects. Each MR scan was normalized to MNI space using nine parameter affine transformations. The ICBM 2009c Nonlinear Asymmetric template was selected to generate the head model. The files also included T1-weighted, T2-weighted and proton density-weighted

modalities. The resolution of the ICBM152 template is $229 \times 193 \times 193$ with $1\text{mm} \times 1\text{mm} \times 1\text{mm}$ voxel size. The T1 weighted sagittal, transverse, and coronal section of MR images are shown in Figure 2-2.

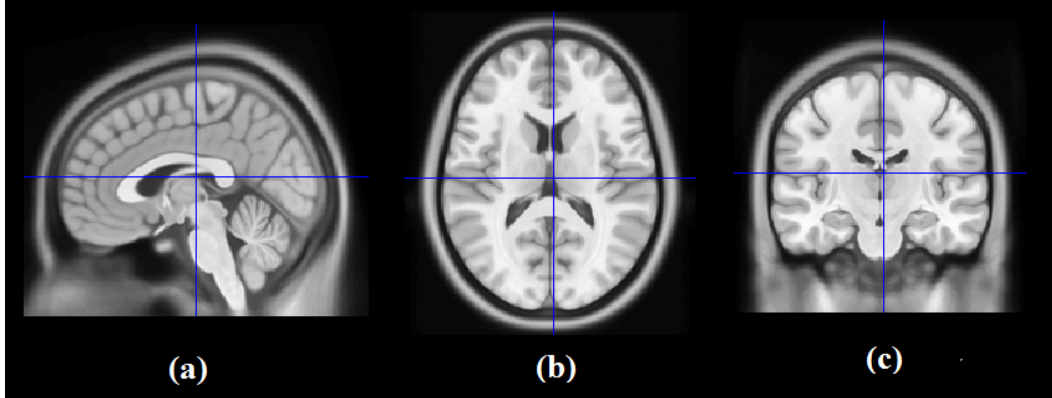


Figure 2-2 T1-weighted MRI images in: (a) sagittal, (b) axial, and (c) coronal view of the ICBM 152 brain atlas.

ICBM 152 template was then imported into Nirview [49], which is a strong finite-element 3D medical image segmentation tool. In MR image sequence, four regions of interest (ROIs), namely scalp, skull, gray matter and white matter, were identified and segmented. Four boundaries of each region were extracted from transverse MR sequence images, as shown in Figure.2-3 (a). After four layers were segmented, the surface meshes were generated based on the binary surface from the segmented data, as shown in Figure.2-3 (b). The quality of the surface is controlled by the ratio of overlap triangles ($< 3\%$).

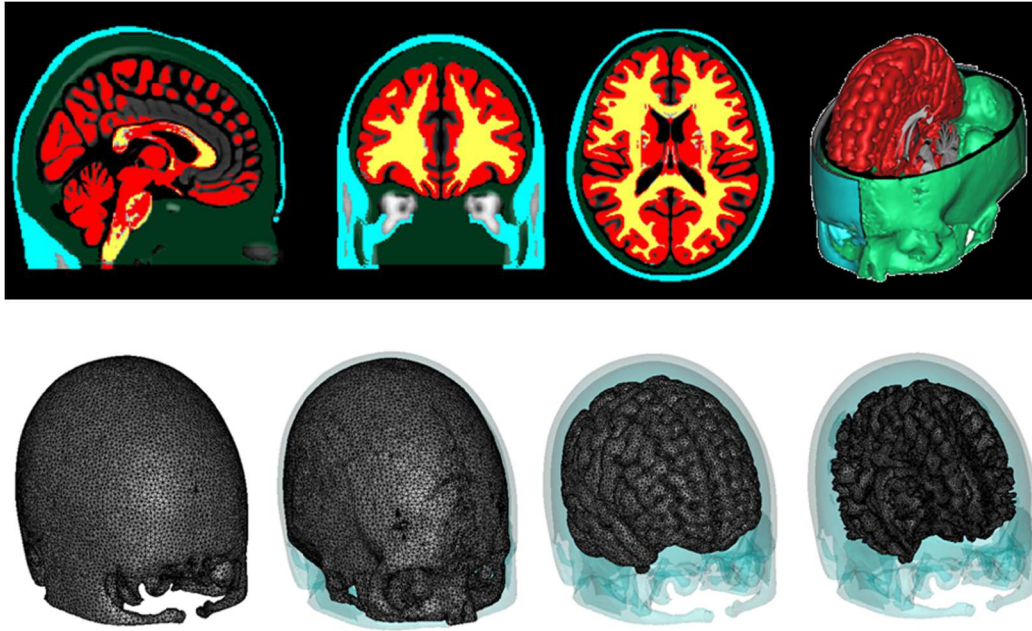


Figure 2-3 (a) Segmentations of four ROIs, namely, scalp (blue), skull (green), gray matter (red) and white matter (yellow); (b) surface mesh generation based on the ROI segmentations, from left to right are the surface mesh of scalp, skull, gray matter, white matter, respectively.

Table 2-1 Optical properties of head tissues for modeling

	Scalp		Skull		Gray Matter		White Matter	
	750nm	850nm	750nm	850nm	750nm	850nm	750nm	850nm
$\mu_a(\text{mm}^{-1})$	0.017	0.019	0.012	0.014	0.018	0.019	0.017	0.021
$\mu_s'(\text{mm}^{-1})$	0.740	0.640	0.940	0.840	0.836	0.673	1.191	1.011

After the surface meshes were generated, the Three-dimensional finite element model (FEM) meshes were then generated by an inside growing process from the surface meshes. This mesh model contains approximately 2×10^5 nodes, which correspond to approximately 106 linear tetrahedral elements. Each node was labeled by one of four ROIs and the node locations were assigned the particular tissue optical properties and were shown in Figure 2-4. The optical properties were obtained from

published literature [39] and listed in Table 2-1. The layer of cerebrospinal fluid (CSF), which was located between the boundary of the inner skull and gray matter and within some gray and white matter, was also extracted (not shown). The CSF layer was not included since the layer between the boundary of the inner skull and gray matter is thin and CSF optical properties are relatively small in both absorption and scattering. Moreover, CSF within a deeper location of the brain does not affect the reconstruction results due to the limited penetration depth of the near infrared light. More details of the 3D volume mesh is indicated in **Appendix A – Figure 1**.

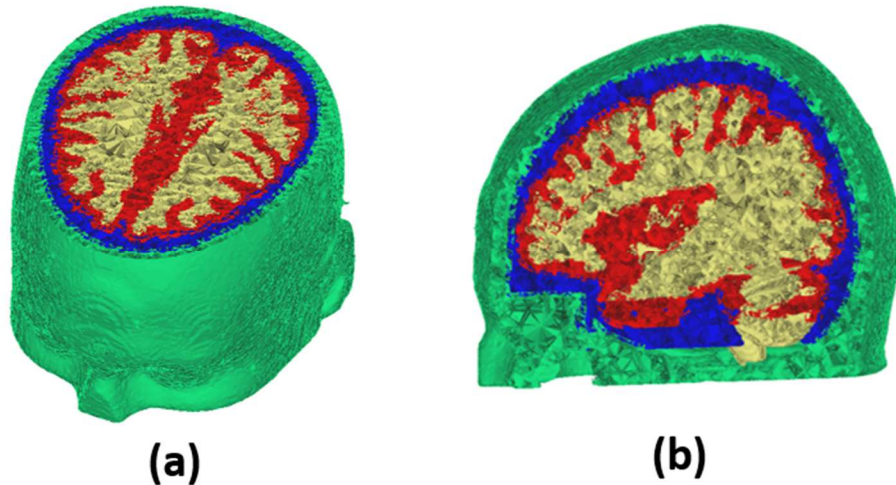


Figure 2-4 Optical properties showed in volumetric meshes in different colors: scalp (green), skull (blue), gray matter (red) and white matter (yellow), respectively. (a) Stereo vision; (b) sagittal view.

2.3 Depth compensation algorithm in atlas-fDOT

2.3.1 Optode arrangement

The sparse optode geometry is used in forward modeling. The optode array consisted of 18 sources and 18 detectors with a nearest inter-optode distance of 25 mm, as shown in Figure 2-5. To simulate real measurement, only first nearest neighbor

measurements are selected to calculate forward problem. The full tomographic data set contained a total of 75 source-detector pairs for one wavelength measurement (Figure 2-5).

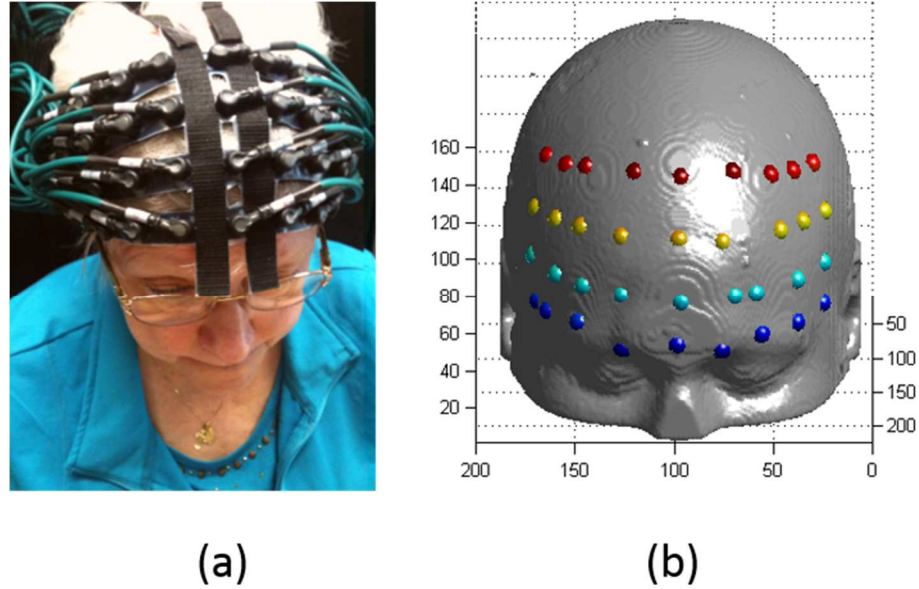


Figure 2-5 Co-registration optodes from real space to MNI space. (a) Optodes placement in real space; (b) projected Optodes in MNI ICBM 152 head model

The projection of optode locations measured from a subject's head in real world (RW) coordinates to the human atlas template is developed, and an affine transformation, is utilized[50]. Briefly, optode positions on a subject's forehead are measured by a 3D Patriot™ digitizer (Polhemus Inc., Colchester, VT). Moreover, I selected several anatomical landmarks based on the EEG international 10-20 system of electrodes placement as anchors for co-registration. These landmarks are Nz (nasion), In (inion), AL (left ear), AR (right ear), and Cz (central position). They are also measured on the subject's head by the 3D digitizer. The MNI coordinates of 10-20 scalp position for ICBM152 are obtained from Cutini et al [51]. The transformation matrix W is then

calculated. With the affine transformation matrix, the optode locations on the MNI head template are obtained by:

$$P_{MNI_O} = P_{RW_O} \times W \quad (2-1)$$

Where P_{RW_O} represents the coordinates of fNIRS optodes in the RW space, P_{MNI_O} represents the coordinates of fNIRS optodes in the MNI head template space, W is the transformation matrix. Coordinates of projected optodes in z-axis are further adjusted by projecting the transformed optode locations in MNI space along the averaged norm of patches from ICBM152 head model. The optode projected onto the surface of the head model is depicted in Figure 2-5 (a) and (b). The region of interest (ROI) is determined as the volume covered by the optode array.

2.3.2 Forward Light Modeling

Photon migration in the ICBM152 head model is performed using a FEM-based MATLAB package, NIRFAST[52], to obtain the Jacobian matrix (also called the sensitivity matrix) J . Matrix J represented changes in measured signals induced by a small absorption perturbation within the brain volume interrogated by the optode pairs. The forward model for light propagation inside the human head used Rytov approximation[53] and is then written as:

$$\Delta y = J_h \Delta x \quad (2-2)$$

where Δy represents a matrix of measured changes in optical density[i.e., $OD = \log\left(\frac{initialsignal}{changedsignal}\right)$] at all source-detector pairs between the initial baseline (y_0) and transient reaction to the BART paradigm (y), i.e., $\Delta y = \log(y_0) - \log(y)$; J_h is the Jacobian matrix derived from the voxel-wise ICBM152 head model; Δx represents a matrix of changes in absorption at each node within the 3D atlas-based coordinates system.

2.3.3 Inverse problem with depth compensation algorithm

The process of image reconstruction is to recover temporal changes of absorption due to the brain response to the stimulus at each FEM node. With the DOT measurement from multiple source-detector pairs, the inverse image reconstruction problem is solved using Moore-Penrose generalized approach[54] with Tikhonov regularization:

$$\Delta x = J_h^T (J_h J_h^T + \lambda I)^{-1} \Delta y \quad (2-3)$$

where λ is the regularization factor and is chosen as (10-2) times the maximum of diagonal of the matrix $J_h J_h^T$ and I is the identity matrix. The depth compensation algorithm (DCA) is utilized here to compensate for the fast decay of sensitivity with the increase of depth. The details on DCA can be found in Niu et al[47] and is briefly described here. The key point of DCA is to compensate for the sensitivity decay by introducing a weighting matrix M , which counter-balances the sensitivity along the depth. Accordingly, the measurement sensitivity matrix J_h within the ICBM152 head model can be decomposed into layer-based sub-matrices based on the distances from the scalp surface to each node below the scalp. Then, the M matrix is formed as:

$$M = (\text{diag}(M(J_{hL}), M(J_{hL-1}), \dots, M(J_{h2}), M(J_{h1})))^\gamma \quad (2-4)$$

where γ is an adjustment power, and $M(J_{hi})$ represents the maximum singular value for measurement sensitivity J_h at the i th layer, where $i = 1 \dots L$; L represents the layers counted from superficial (the surface of scalp which is covered by the optode array) to deep layers. The adjustment power, γ , in equation 2-4 can control the compensating weight in M ; γ is the empirical parameter with an optimal range of 0.5 to 1.5 that is demonstrated by Aim 1.3. $\gamma = 1.0$ is used in this Chapter. Accordingly, an

adjusted sensitivity matrix $J_h^\#$ defined as $J_h^\# = J_h M$ is used in the inverse calculation.

After replacing J_h by $J_h^\#$ in eq. (2-3), I expressed the image reconstruction equation after DCA is applied as follows:

$$\hat{\Delta x} = J_h^{\#T} \left(J_h^\# J_h^{\#T} + \lambda I \right)^{-1} \Delta y = M J_h^T \left(J_h M^2 J_h^T + \lambda I \right)^{-1} \Delta y \quad (2-5)$$

Image indicates DCA effects on the sensitivity matrix is shown in **Appendix A – Figure 2**. The image shows the axial view of the Jacobin matrix respect to the changes of adjustment power from 0.1 to 3.0 with the interval of 0.1.

Consequently, determination of absorption changes at two wavelengths leads to reconstructed images of relative changes in ΔHbO , ΔHbR , and ΔHbT concentrations, based on spectral decomposition of the extinction coefficients for both wavelengths[42].

2.4 Optimization of depth compensation parameter

In order for DCA to work optimally, I needed to investigate how to correctly select the γ value for the new sensitivity matrix $J_h^\#$, since γ critically determines the depth sensitivity in reconstruction. To do so, I performed computer simulations to understand the dependence of quality of reconstructed images on γ .

2.4.1 Preliminary results of computer simulation in the brain atlas-guided model along vertical directions.

I performed multiple simulations with the object being located from the top surface along with the vertical line direction with a maximum depth of 40mm. The size of the absorber used is 15mm in diameter and the absorption coefficient is two times that of the surrounding background. As the depth increased, the type of surrounding tissue changes to scalp, skull, gray matter and white matter respectively Therefore, the absorption coefficient of the object will alter twice as the surrounding tissue, as listed in Table1. Gaussian random noise (0.1%) was introduced in the simulation based on noise

levels observed in our actual experiments. Figure. 2-6 demonstrates the computer simulated object at the depth of 20 mm and the reconstructed image wherever $\gamma = 0.5, 1.0, 1.5, 2.0, 2.5, 3.0$. It is observed that as the γ increases, the shape of the reconstructed object is enlarged, and the center position of the object is moved along the vertical line direction. It is clearly illustrated that as the adjusted power γ increases, the more compensation to the sensitive matrix A and thus the larger shift of the reconstructed object.

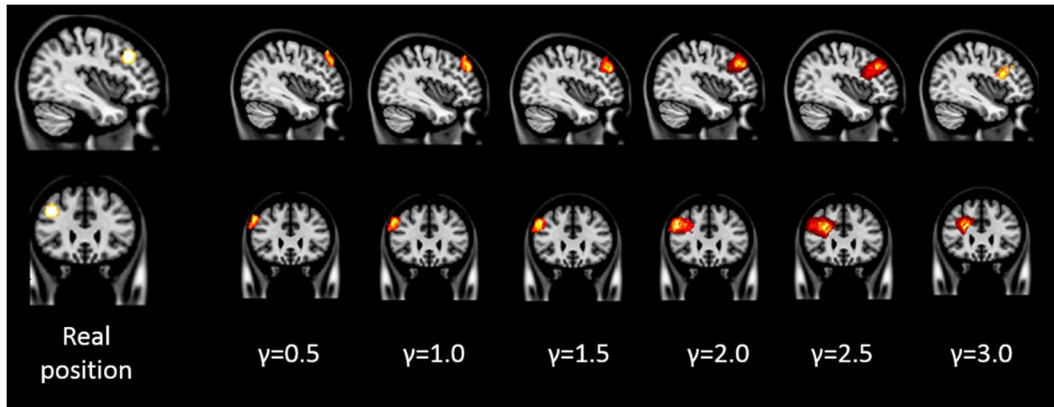


Figure 2-6 Illustration of computer simulation object in the fixed depth of 20 mm, varying γ from 0 to 3.0. From left to right showed the reconstructed object on sagittal view (upper line) and coronal view (lower line) with respect to $\gamma = 0.5, 1.0, 1.5, 2.0, 2.5$ and 3.0 .

2.4.2 Preliminary result of simulation process to Optimize adjusted power for DCA.

At each object depth, the γ value is varied from 0.0 to 3.0 with the interval of 0.1 to investigate how γ affected the quality of reconstructed images. For each depth and γ value, an image is reconstructed based on the adjusted matrix $J^\#$. The image quality is evaluated by (1) the contrast-to-noise ratio (CNR) and (2) the position error (PE). The CNR is defined as the difference between the averaged absorption coefficient within the region of interest (ROI) and the region of background (ROB) divided by the weighted average of the standard deviations in the ROI and ROB[55]. The PE is defined as the

distance between the centers of real and reconstructed objects[56]. Larger CNR and smaller PE values indicate better quality of reconstructed image.

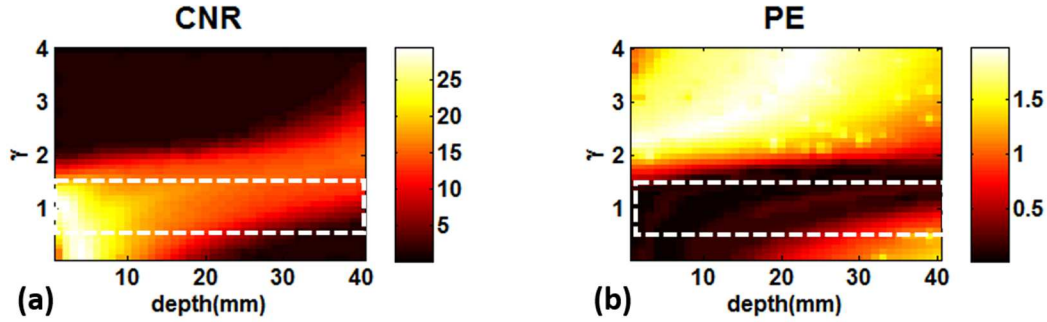


Figure 2-7 Dependence of (a) CNR and (b) PE of reconstructed images on object depth, z , and γ for an object ($d = 15\text{mm}$). They are generated when simulations moved the object along vertical direction below the head surface, while γ value increased from 0 to 3. The dashed rectangles outline the uniform value of CNR and PE.

Fig.2-7 (a) and (b) indicate the computed CNR and PE results as function of object depth, z and adjustment power γ . These simulated results clearly demonstrate that with the depth compensation matrix, M , there exist a small range of γ values between 0.5 to 1.5 (as outlined by the dashed boxes in the Figure), providing best CNR and PE outputs, while the object depth varies from $z = 0$ to -40 mm. These Figures imply that with an optimal selection of γ , an embedded object in tissue can be reconstructed through fDOT with accurate depth localization at both superficial (e.g. 10 mm) and deep (e.g., 25 mm or deeper) tissue locations.

2.5 Summary

In this chapter, an atlas-guided diffuse optical tomography system has been developed. Specifically, a standard brain atlas based on ICBM152 template is generated. The co-registration process overlaid the optical sources and detectors on the surface of brain atlas. Finite-element forward calculation provided a three dimensional optical

sensitivity matrix. Tikhonov regularization reconstructed the distributions of the optical properties of the object from the scalp, skull and cortex. An simulation has been conducted to validate the imaging depth accuracy. Results indicate that the atlas-DOT is capable to accurately reconstruct the objects from 20 mm below the scalp. In addition, adjustment power has been selected by optimizing the position error and contrast to noise ratio. Overall, this chapter introduced the development of computational tools that significantly increased the fDOT image lateral resolution and image depth.

Chapter 3

Assessment of Measurement Reliability of Atlas-DOT for Brain Imaging

3.1 Introduction

Test-retest reliability is one of the basic aspects in the examination of scientific measurements and physiological or psychological quantifications. In the field of behavioral sciences, the intraclass correlation coefficient (ICC) has been a common parameter or index used to estimate measurement reliabilities induced by human errors and variations among judges or raters. Shrout and Fleiss reviewed a class of ICCs and provided guidelines for use in rater reliability in behavioral sciences research [57]. McGraw and Wong gave a more complete review of various forms of ICC and inference procedures in the same context for behavioral sciences research [58]. Weir discussed issues in the use of ICCs for quantifying reliability in movement sciences [59]. These studies provided statistical foundation for reliability assessment and emphasized that there are different forms of ICC, which may lead to different results when applied to the same data. Therefore, it is important to choose an appropriate form of ICC which matches with the experimental design and concerns in a specific study.

Recently, in the neuroimaging field, a few groups have adapted ICCs for assessing test-retest reliability in different applications of functional brain imaging. For example, Plichta et al. and Bhambhani et al. applied ICC(1,1) and ICC(1,2) in the quantification of test-retest reliability in functional near infrared spectroscopy (fNIRS) studies [60], [61]. Braun et al. used ICC(3,1) and ICC(2,1) to study the reliability of a functional magnetic resonance imaging (fMRI)-based graph theoretical approach [62]. Table 3-1 lists a number of recently published papers on fMRI and fNIRS where ICCs are used to measure test-retest reliabilities. Though different forms of ICC have been used in existing studies, no justification of their choice is provided in any of them. As a result, it is

not clear whether the chosen ICC metrics fit the study, making it difficult to compare results from different studies. Moreover, most literature discussing ICCs has been in the context of rater reliability studies in which a set of targets are rated by several judges, while neuroimaging researchers are concerned about the measurement reliability of a certain image modality in repeated tests. This essential difference must be made clear in the adaptation of ICCs. However, no explanation on this aspect is given in the publications listed in Table 3-1.

Table 3-1 Overview of fNIRS/fMRI reliability studies using ICCs

Study reference	Modality	ICC type
[61]	fNIRS	Not provided
[60]	fNIRS	ICC(1,1), ICC(1,k)
[18]	fNIRS	ICC(1,1), ICC(1,k)
[63]	fNIRS	ICC(1,1), ICC(1,k)
[64]	fMRI	ICC(1,1), ICC(1,k)
[65]	fMRI	ICC(3,1),
[62]	fMRI	ICC(2,1), ICC(3,1)
[66]	fNIRS	ICC(1,1), ICC(1,k)
[67]	fMRI	ICC(2,1)
[68]	fNIRS	ICC(1,k)
[69]	fMRI	ICC(2,1)
[70]	fMRI	ICC(2,1)

Since the ICCs are derived under different assumptions, their values would be meaningless and misleading if those assumptions are not met. In addition, there are many issues regarding the inference and interpretation of ICCs in measurement reliability assessment. As far as we know, no current work has been done on such issues. The aim of this Chapter is to bridge the gap in the literature by reviewing the statistical rationale of ICCs in the context of measurement reliability assessment and providing general guidelines on the selection of ICCs, particularly for functional diffuse optical tomography (fDOT). Specifically, we will demonstrate the approach by assessing the measurement reliability of f DOT with a risk decision- making protocol. It is noteworthy that our study

represents a common subject on test-retest reliability of neuroimaging measurements and thus has broad applicability to various neuroimaging modalities.

3.2 A guideline to assess measurement reliability in functional brain imaging using intraclass correlation coefficient

3.2.1 Mathematical model of intraclass correlation coefficient

3.2.1.1 Unified ANOVA model

In order to assess test-retest reliability, data as shown in Table 3-2 are usually collected. Assume that n subjects ($j=1, \dots, n$) are used in this study, and k repeated tests ($i=1, \dots, k$; $k=2$ for a test-retest case) are conducted on each subject. Let y_{ij} be the recorded quantity of the j th subject in the i th test/measurement. Note that in the context of rater reliability assessment, considered in most ICC literature, a set of targets is rated by several judges; the reliability of the raters is determined. In contrast, in the context of test-retest reliability assessment, a set of subjects is measured in two or more repeated tests or measures; the measurement reliability of the tests is the intention of the researcher to quantify. Thus, “subjects” and “tests or measures” in our study correspond to “targets” and “judges”, respectively, in the rater reliability study.

Table 3-2 General data format

Test ($i = 1, \dots, k$)	Subject ($j=1, \dots, n$)			
	$j=1$	$j=2$...	$j=n$
1	y_{11}	y_{12}	...	y_{1n}
2	y_{21}	y_{22}	...	y_{2n}
...
k	y_{k1}	y_{k2}	...	y_{kn}

*: In our study, y_{ij} represents ΔHbO from the j th subject in the i th measurement.

Appropriate ANOVA models are the basis of ICCs. Eq. (3-1) below expresses the unified ANOVA model for the data in Table 3-2:

$$y_{ij} = \mu + S_j + T_i + e_{ij} \quad (3-1)$$

where μ is the overall population mean, S_j is the deviation from the population mean of the j th subject, T_i is the systematic error in the i th test, and e_{ij} is the random error in the measurement of the j th subject in the i th test. This model rests on the idea that the measurement is a combination of the true status of the subject (i.e., $\mu + S_j$) and measurement errors (i.e., $T_i + e_{ij}$). There are two types of measurement errors, the systematic error of the test (T_i) and the random error (e_{ij}) [59]. Different systematic errors in the tests (i.e., T_1, T_2, \dots, T_k) may be caused by different measurement conditions in the tests (e.g., different devices are used in the tests, or the tests are conducted at different locations or time slots), or the “learning effects” in repeated testing (e.g., subjects tend to become more and more skilled in later tests). The random error is the error due to uncontrollable random factors such as patient factors, environmental factors and operator errors.

Assumptions on each term in the model are as follows:

(A1) “Subject” is a random factor and S_j represents the random effect of this factor which is assumed to follow a normal distribution with mean 0 and variance

$$S_j \sim N(0, \sigma_s^2) \quad (3-2)$$

Here the term “random factor” means that subjects involved in this study are viewed as randomly selected from a larger population of possible subjects. Accordingly, the variance represents the heterogeneity among this population.

(A2) “Test” can be treated as a random factor or a fixed factor and T_i is the systematic error in the i th test. When it is treated as a random factor, T_i represents the random effect of this factor which is assumed to follow a normal distribution with mean 0 and variance. When it is treated as a fixed factor, T_i represents the fixed effect of this

factor and it is assumed that the sum of the effects is 0. Equations (3-3) and (3-4) explain these two effects in mathematical expressions:

$$\text{Random effect: } T_i \sim N(0, \sigma_T^2) \quad (3-3)$$

$$\text{Fixed effect: } \sum_{i=1}^k T_i = 0 \quad (3-4)$$

The difference between random factor and fixed factor is that in the former case, the repeated k tests conducted in the study are viewed as random samples from a larger population of possible tests/measurements, and accordingly the variance represents the variability of this population. In the latter case, the repeated k tests are not representative of possible tests; the concern is only the effect of these particular tests conducted in the study instead of a generalization to the underlying population of possible tests. Note that T_i is a random variable in the case of random factor and a fixed, unknown quantity in the case of fixed factor.

(A3) The random error is assumed to follow a normal distribution with mean zero and variance , as written

$$e_{ij} \sim N(0, \sigma_e^2) \quad (3-5)$$

(A4) The effect of interaction between “Subject” and “Test” (i.e., “Subject × Test”) is assumed to be insignificant and thus ignored in Eq. (3-1). This means that the systematic error of each test is similar for all subjects, which is reasonable in most cases. In situations where this assumption is violated (i.e., the systematic error varies from subject to subject), this interaction effect is mingled with the random error and not identifiable using the data shown in Table 3-2 since there is no replicate under each combination of “Subject” and “Test”. In this case, the formulas of ICCs are the same as in the case without the interaction effect.

Based on the unified ANOVA model, several special models can be obtained by adopting different assumptions regarding whether the effect of “Test” is significant and whether to treat “Test” as a random or fixed factor in (A2) above. Different forms of ICC can be derived from those special models as shown in the following section.

3.2.1.2 Six forms of ICC

The ICCs reviewed by Shrout and Fleiss are based on three special models derived from the unified model: one-way random-effect model (Model 1), two-way random-effect model (Model 2), and two-way mixed-effect model (Model 3) [57]. These models are listed in Table 3-3. If we assume that the effect of “Test” is not significant (i.e., systematic error is negligible or systematic errors in the repeated tests do not differ significantly), the term T_i can be removed from the unified model, which leads to the one-way random-effect model. When the effect of “Test” cannot be ignored and “Test” is treated as a random factor given in (A2) by Eq. (3-3), the unified model becomes a two-way random-effect model. If “Test” is treated as a fixed factor as given in (A2) by Eq. (3-4), the unified model becomes a two-way mixed-effect model. The name “mixed effect” comes from the fact that the model contains both random effect (i.e., S_j) and fixed effect (i.e., T_i).

Table 3-3 ANOVA models as basis of ICCs

Model	Form	Assumptions
one-way random-effect model	$y_{ij} = \mu + S_j + e_{ij}$ $i=1, \dots, k; \quad j=1, \dots, n$	$S_j \sim N(0, \sigma_s^2); \quad e_{ij} \sim N(0, \sigma_e^2);$ Systematic error of test is insignificant.
two-way random-effect model	$y_{ij} = \mu + S_j + T_i + e_{ij}$ $i=1, \dots, k; \quad j=1, \dots, n$	$S_j \sim N(0, \sigma_s^2); \quad T_i \sim N(0, \sigma_T^2); \quad e_{ij} \sim N(0, \sigma_e^2)$

Table 3-3—Continued

two-way mixed-effect model	$y_{ij} = \mu + S_j + T_i + e_{ij}$ $i=1, \dots, k; \quad j=1, \dots, n$	$S_j \sim N(0, \sigma_s^2); \quad \sum_{i=1}^k T_i = 0; \quad e_{ij} \sim N(0, \sigma_e^2)$
----------------------------	---	---

Table 3-4 shows the variance decomposition in each of the three models, including the degree of freedom (df), mean squares (MS) and expected mean squares (EMS) of each variance component. Specifically, in the one-way random-effect model, the total variance of measurements is decomposed into two components: between-subjects variance and within-subjects variance, which are estimated by the between-subjects mean squares (MSB) and within-subjects mean squares (MSW) respectively:

$$MS_B = \frac{k}{n-1} \sum_{j=1}^n (\bar{y}_{.j} - \bar{y}_{..})^2 \quad (3-6)$$

$$MS_W = \sum_{i=1}^k \sum_{j=1}^n (y_{ij} - \bar{y}_{.j})^2 \quad (3-7)$$

where $\bar{y}_{.j}$ is the mean of measurements on the j^{th} subject (i.e., data in the j^{th} column of Table 2), and $\bar{y}_{..}$ is the mean of all the measurements in Table 3-2. In the two-way random-effect and mixed-effect models, the total variance is decomposed into three components: between-subjects variance, between-tests variance and random error variance, which are estimated by the between-subjects mean squares (MSB), between-tests mean squares (MST) and residual mean squares (MSE). MSB has the same formula as in the one-way random-effect model, and MST and MSE are defined by

$$MS_T = \frac{n}{k-1} \sum_{i=1}^k (\bar{y}_{i.} - \bar{y}_{..})^2 \quad (3-8)$$

$$MS_E = \frac{1}{(n-1)(k-1)} \sum_{i=1}^k \sum_{j=1}^n (y_{ij} - \bar{y}_{i.} - \bar{y}_{.j} + \bar{y}_{..})^2 \quad (3-9)$$

where $\bar{y}_{i.}$ is the mean of measurements in the i th test (i.e., data in the i th row of

Table 3-2). It is worth mentioning that the mean squares can be obtained automatically from the software output in ANOVA analysis.

Table 3-4 Variance decomposition in the ANOVA models

	df	MS	EMS
one-way random-effect model			
Between subjects	$n-1$	MS_B	$k\sigma_S^2 + \sigma_e^2$
Within subjects (Error)	$n(k-1)$	MS_W	σ_e^2
two-way random-effect model			
Between subjects	$n-1$	MS_B	$k\sigma_S^2 + \sigma_e^2$
Within subjects			
Between tests	$k-1$	MS_T	$n\sigma_T^2 + \sigma_e^2$
Error	$(n-1)(k-1)$	MS_E	σ_e^2
two-way mixed-effect model			
Between subjects	$n-1$	MS_B	$k\sigma_S^2 + \sigma_e^2$
Within subjects			
Between tests	$k-1$	MS_T	$\frac{n}{k-1} \sum_{i=1}^k T_i^2 + \sigma_e^2$
Error	$(n-1)(k-1)$	MS_E	σ_e^2

The ICC is rigorously defined as the correlation between the measurements on a subject in the repeated tests [57]. Intuitively, if this correlation is high, that means the

neuroimaging modality yields very similar measurements in the tests (or test and retest when $k=2$), an indicator of high reliability. A more technical interpretation of ICC is that it is a measure of the proportion of variance due to subjects [58]. Following this interpretation, the ICC can be defined in two ways: as measure of test (absolute) agreement and as measure of test consistency [58]. Eq. (3-10) and (3-11) are the expressions of the two definitions

$$\text{Reliability (Agreement)} = \frac{\text{between-subjects variance}}{\text{between-subjects variance} + \text{between-tests variance} + \text{random error}} \quad (3-10)$$

$$\text{Reliability (Consistency)} = \frac{\text{between-subjects variance}}{\text{between-subjects variance} + \text{random error variance}} \quad (3-11)$$

For each of the three models, the ICC as defined in Eq. (3-10) or Eq. (3-11) can be adopted. Under each definition, reliability of a single measurement and reliability of the average of the k measurements (called reliability of the average measurement for simplicity hereafter) will be considered. This gives a total of $3 \times 2 \times 2 = 12$ possible forms of ICC. The six forms of ICC developed by Shrout and Fleiss which have been widely used in the literature are summarized in Table 3-5. Following the notations in the primary reference by [57], these ICCs are designated as ICC(1,1), ICC(1,k), ICC(2,1), ICC(2,k), ICC(3,1) and ICC (3,k), where the first index indicates one of the three underlying ANOVA models (see Table 3-3), and the second index indicates whether the reliability of a single measurement ($=1$) or that of the average measurement (over k repeated tests) is considered. Derivations of these ICCs and their respective parameters or formulas listed in Tables 3-4 and 3-5 are given in **Appendix B**.

Table 3-5 Definition of ICCs and computation formula

Designation	Model	Definition	Computation formula
ICC(1,1)	one-way random-effect model	$\frac{\sigma_S^2}{\sigma_S^2 + \sigma_e^2}$	$\frac{MS_B - MS_W}{MS_B + (k-1)MS_W}$
ICC(1,k)		$\frac{\sigma_S^2}{\sigma_S^2 + \sigma_e^2 / k}$	$\frac{MS_B - MS_W}{MS_B}$
ICC(2,1)	two-way random-effect model	$\frac{\sigma_S^2}{\sigma_S^2 + \sigma_T^2 + \sigma_e^2}$	$\frac{MS_B - MS_E}{MS_B + (k-1)MS_E + k(MS_T - MS_E)/n}$
ICC(2,k)		$\frac{\sigma_S^2}{\sigma_S^2 + (\sigma_T^2 + \sigma_e^2) / k}$	$\frac{MS_B - MS_E}{MS_B + (MS_T - MS_E)/n}$
ICC(3,1)	two-way mixed-effect model	$\frac{\sigma_S^2}{\sigma_S^2 + \sigma_e^2}$	$\frac{MS_B - MS_E}{MS_B + (k-1)MS_E}$
ICC(3,k)		$\frac{\sigma_S^2}{\sigma_S^2 + \sigma_e^2 / k}$	$\frac{MS_B - MS_E}{MS_B}$

3.2.1.3 ICC criteria to assess reliability of measurements

Since ICCs measure a correlating relationship with a value between 0 and 1, it is practically important to have standard criteria used to assess reliability of measurements. According to published literature [71], [72], criteria of ICC values for medical or clinical applications are grouped into 4 categories, listed as follows. The level of clinical significance is considered poor, fair, good, and excellent when $ICC < 0.40$, $0.40 < ICC < 0.59$, $0.60 < ICC < 0.74$, and $0.75 < ICC < 1.00$, respectively. In the present study, we follow the same criteria since most of the previous publications in the neuroscience field have utilized the same or very similar criteria [62]–[65], [70], [73], [74]. Note that different applications may vary the ICC range in large extent based on specific needs and

definitions given by individual clinical applications [75], [76]. In general, using $ICC = 0.40$ as the floor of an acceptable range for reliability of measurements is still reasonable as most of fMRI results have ICC values of 0.33-0.66, which are commonly considered reliable.

3.2.2 Addressing the Selection of ICCs

One critical issue or puzzle in applying ICCs to assess the reliability of neuroimaging measurements is how to select appropriate ICCs from the six forms given in Table 5 for a specific study. How to make an appropriate selection is the topic of this subsection. We will first present several properties on the interpretations and magnitudes of the ICCs and then provide detailed guidelines on ICC selection.

3.2.2.1 Properties of ICCs

The six forms of ICC given in Table 5 have the following properties:

Property 1: $ICC(1,1)/ICC(1,k)$ and $ICC(2,1)/ICC(2,k)$ are measures of test agreement (i.e., as defined by Eq. (3-10)) as the between-tests variance is included in their denominators; $ICC(3,1)/ICC(3,k)$ are measures of test consistency (i.e., as defined by Eq. (3-11)) as the between-tests variance is not included in their denominators.

Property 2: Among the three ICCs for a single measurement, the relationship of $ICC(1,1) \square ICC(2,1) \square ICC(3,1)$ exists in most cases. Specifically, when the effect of “Test” is not significant, namely, σ^2_{Test} is small, these three ICCs have similar values as their denominators are close to each other (see Eqs. (3-10) and (3-11)). When the effect of “Test” is significant, the correlation between measurements will be underestimated in the one-way random-effect model [57], that is, $ICC(1,1) < ICC(2,1)$. In this case, we expect that $ICC(2,1) < ICC(3,1)$ because the denominator of $ICC(3,1)$ does not include the between-tests variance and thus is smaller than that of $ICC(2,1)$.

Property 3: ICCs of the average measurement are larger than their counterparts for a single measurement. The reason is that averaging over repeated measurements deduces the variance of measurement/test errors, leading to a decrease in between-tests variance and an increase in overall ICCs, as interpreted by Eq. (3-10).

3.2.2.2 Guidelines on ICC Selection

To appropriately assess reliability of neuroimaging measurements, appropriate ICCs need to be chosen based on the specific study. Usually both the ICC of a single measurement and that of the average measurement will be used, so the primary issue here is how to choose the most appropriate ANOVA model among the three alternatives, Model 1 (one-way random-effect model), Model 2 (two-way random-effect model), and Model 3 (two-way mixed-effect model). Two decisions need to be made by answering the following questions: (1) do we choose one-way model or two-way model? (2) Do we choose two-way random-effect model or mixed-effect model? Clear and confident decisions can be done by integrating expert knowledge on the study and statistical testing. Guidelines on making the two decisions are provided as follows.

3.2.2.3 Determination of one-way model vs. two-way model

There are two considerations regarding the choice between the one-way model and two-way model:

First, we need to consider the significance of the effect of “Test”. If we believe that the systematic error is negligible or the systematic errors in all the tests are similar, the one-way model should be chosen; otherwise, the two-way model should be chosen. This can also be decided by statistical testing on the significance of this effect. Specifically, a two-way model (either the random-effect model or mixed-effect model) is first constructed through ANOVA. This analysis will automatically conduct F test on the effect of “Test” and yield a p-value as part of its output. If the p-value is small (e.g.,

<0.05), it means that the effect of “Test” is significant and thus the two-way model is the correct model; otherwise, the one-way model is the correct model. However, when the effect of “Test” is not significant, though the one-way model is the correct model, ICCs derived from the two-way models will still have similar values to those derived from the one-way model (based on Property 2). Thus, in terms of reliability assessment, the two-way model (i.e., either Model 2 or 3) is more robust and can be used regardless of the significance of the “Test” effect.

Second, we need to pay attention to the design of experiment. Shrout and Fleiss (1979) give one example (Case 1 in the paper) where the one-way model must be used in the context of rater reliability assessment. In that example, each target is rated by a different set of judges, or in other words, each judge only rates one target [57]. McGraw and Wong provide two other examples similar to this case, called “unordered data” and “unmatched data” [58]. The first example represents the situation where the data on the same target are collected in such a way that their ordering is irrelevant, while the second example represents the instance where each observation is made under unique measurement conditions. Essentially, these examples reflect two situations where the one-way model should be used: when there is no way to assign data to measurement categories (such as “Test” and “Retest”), or when the data in the same measurement category are obtained under different conditions. The second situation may occur in the test-retest reliability assessment. For example, during one test, some subjects may be measured using different devices, at different locations, or during different time slots from others.

3.2.2.4 Determination of two-way random-effect model vs. mixed-effect model

To choose between the two-way random-effect model and mixed-effect model, we need to have a clear understanding of these two models in the following aspects:

First, we need to be aware of the distinction between random-effect vs. fixed effect. As mentioned previously, “Test” is treated as a random factor in the two-way random-effect model. In technical terms, this means that all possible tests/measurements by the studied neuroimaging modality are interchangeable. In practical terms, it means that the systematic errors in all possible tests are random and do not have any pattern (e.g., systematic error in later tests is smaller or larger than that in previous tests); in other words, the results from the particular k tests conducted in this study can be generalized to all possible tests. In contrast, “Test” is treated as a fixed factor in the two-way mixed-effect model. This means that the results from the conducted tests are not random and thus cannot be generalized to all possible tests or such a generalization is not of interest.

Second, we need to correctly interpret ICCs in terms of absolute agreement vs. consistency between measurements from the repeated tests. By Property 1, $ICC(2,1)/ICC(2,k)$ and $ICC(3,1)/ICC(3,k)$ have different interpretations, as measure of absolute agreement between the tests vs. consistency of them. Technically, the two interpretations differ in whether the between-tests variance is taken into consideration in reliability assessment: absolute agreement measures include between-tests variance, while consistency measures do not. Thus, $ICC(3,1)/ICC(3,k)$ should be used in cases where the between-tests variance is an irrelevant source of variation [58]. One example is when the concern is not the absolute measurements of subjects in each test, but their relative differences in the test (correspondingly, deviation of each measurement from the average of all subjects in the test will be used in the analysis).

3.2.2.5 General guidelines

Based on the above explanations and comprehensions, general guidelines on selecting the most appropriate ICCs from the popular forms of ICC listed in Table 5 are summarized below:

- i. If the subjects in the same test and/or neuroimaging measurement are not measured under the same conditions (device, location, time slots, etc.), ICC(1,1)/ICC(1,k) should be used.
- ii. If the between-tests variance is not significant according to the F test in ANOVA, ICC(1,1), ICC(2,1) and ICC(3,1) have similar values and thus any of them can be used in reliability assessment. If the between-tests variance is significant, ICCs from the two-way models should be used.
- iii. If (a) it is reasonable to generalize the results in a study to all possible tests and (b) absolute agreement of measurements in repeated tests is concerned, ICC(2,1)/ICC(2,k) should be used.
- iv. If (a) it is not reasonable to generalize the results to all possible tests or (b) consistency of measurements in repeated tests is concerned, ICC(3,1)/ICC(3,k) should be used.

3.3 Risk decision-making using balloon analog risk task

3.3.1 *Introduction of balloon analog risk task*

Developed in 2002 by Lejuez et al., Department of Psychology at the University of Maryland—College Park, BART provides a simulated context in which actual performances of risk-taking propensity can be assessed [77]. Currently, BART is the most broadly used and tested risk task behavioral tool [78]. BART has been administered to a broad range of populations (adolescents through young adults), is psychometrically sound, and has been correlated to “real-world” risk taking [77], [79]–[81]. BART consists

of a set of 30 computer-simulated balloon pumping trials. Increasing balloon inflation is associated with greater reward (5¢/pump), but each balloon can potentially explode at any point, causing any accumulated reward for that balloon to disappear. Decisions to continue (increase potential reward) or cease balloon inflations (collect accrued \$\$) must balance potential gain against any potential risk of losing the accrued reward. A larger balloon is associated with increased probability of explosion or risk-taking.

The original BART offers subjects the voluntary choice to determine the risk level (end size) for each balloon and resulting monetary winnings. Rao et al (2008), Neurology Department at the University of Pennsylvania, modified BART for use with fMRI and administered BART in both active (voluntary) and passive (involuntary) decision-making modes to 14 participants between 21 and 35 years [82]. The active choice mode did not differ from the “original” BART because participants chose when to discontinue inflating the balloons. In the passive mode, participants had no choice and are forced to observe computer-generated balloon inflations where balloon end-size and corresponding monetary reward outcomes are randomly determined. Rao et al. separated measurements of neural substrates of risk from decision-making in young adults. The passive risk decision-making mode demonstrated only visual pathway activation, while active choice mode elicited robust activations in midbrain, striatum, anterior insula, dorsal lateral PFC and anterior cingulate cortex/medial PFC.

Differing slightly from Rao et al.’s (2008) fMRI-BART protocol, I modified the original BART protocol into a MATLAB™-based graphical user interface (GUI). In the next part, the details of MATLAB™-based BART protocol is introduced. This protocol is used as the assessment tool of risk decision-making in multiple studies. Specifically, in this chapter, BART is used as the risk decision-making protocol to test the reliability of atlas-DOT technique. This protocol is also used in the rest of chapters as the tool of

assessment of risk decision-making. Specifically, in chapter 4, BART is used to compare the GLM-based DOT with conventional block-average method. In chapter 5 and 6, BART is used in two applications, which are age-effect study and gender-effect study under risk decision-making.

3.3.2 Development of MATLAB-based BART protocol

In order to assess age-related risk decision-making changes, the original BART protocol is modified into MATLAB™-based GUI. Several changes are made compare to the original BART protocol. Firstly, user interface is added in order to provide the options to choose “active task” or “passive task”. Meanwhile, the starting up of data acquisition and the beginning of protocol are synchronized by push either “active task” or “passive task” button. Secondly, the protocol is changed into a two phases block/event-related design. As showed in Figure 3-1, This fNIRS BART paradigm included risk decision making tasks within two modes: the active (voluntary) and the passive (involuntary) modes. two phases are clearly presented in this protocol. The first phase named “decision-making” phase and the second phase named “outcome” phase.

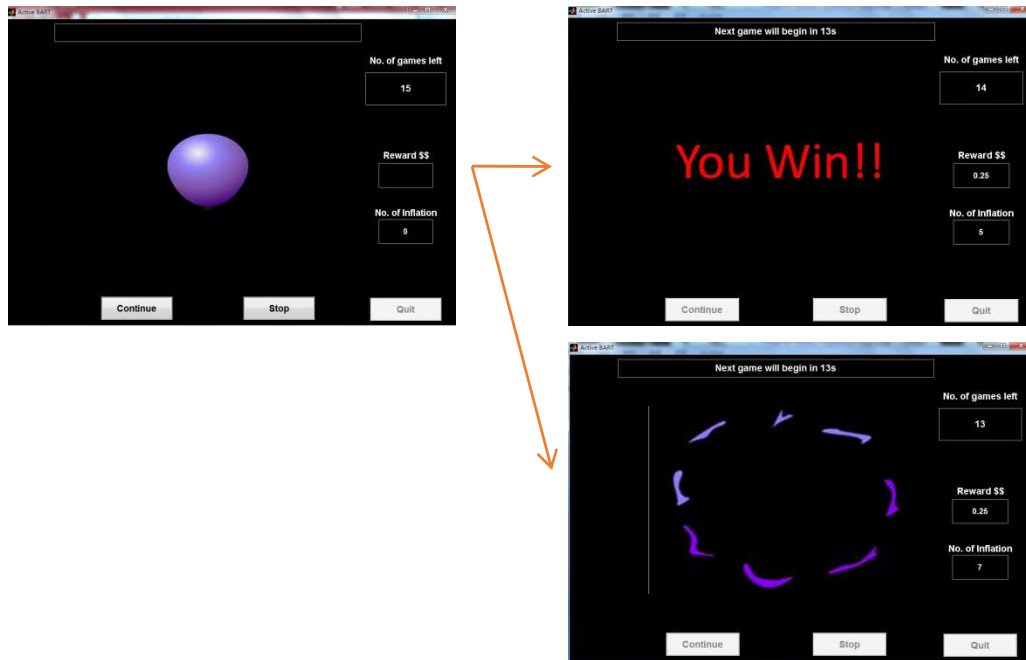


Figure 3-1 BART risk decision-making task outcomes in both active and passive modes: (a) Stop balloon inflations and collect \$\$ ["You Win!!"] or (b) Balloon explodes and lose accrued \$\$ for that balloon ["You Lose!!"].

Even though the probability of risk of balloon explosion is set by the program; the maximum number of inflations per balloon that participants could make is twelve. Since the current study replicated the fMRI-BART protocol, refer to Table 1 in Rao et al. (2008) for information on risk of explosion, actual probability of explosion, value of winnings, and reward variance associated with balloon inflation [82]. Prior to the start of the study, the following instructions are given to each participant to read, ensuring the correction operation and procedures for the fNIRS-BART protocol:

1. You will complete 2 versions of BART—one where you make choices (Active) and one where the computer decides for you (Passive).
2. At the beginning of each version, you will see a realistic image of a balloon on the laptop computer screen.

3. You will be given 15 balloon trials for each of the 2 versions. There will be a 15 second pause between balloons.

4. Each balloon could grow larger or explode—the goal is to maximize the on-screen “virtual” monetary reward. (“Virtual” monetary reward does not equal “actual” monetary reward).

5. Each balloon could explode at any size.

6. Larger balloons are associated with greater risk of explosion and higher “virtual” monetary reward.

7. The researcher will let you know what version you are doing first.

For the Active Version:

1. To inflate the balloon: click “Start” with mouse.

2. To stop inflating and collect \$\$: click “Stop” with mouse. You will see money added to your account.

3. If a balloon explodes, you will lose any money accrued for that balloon, but you will not lose money that you have already collected from other balloons.

For the Passive Version:

Click mouse once on “Start” to begin each balloon and observe what computer decides to do with each of the 15 balloons.

Before each task, baseline imaging data are measured for five minutes with participants asked to keep their eyes closed. Each protocol, whether for active or passive modes, included 15 repeated blocks (Figure 3-2). In the beginning of each block, the participants are given a balloon image on the computer screen (Figure 3-1) and instructed to inflate it by clicking the mouse as many times as they wished before either the balloon exploded or the decision of “Collect \$\$” is made which stopped balloon inflations for that particular balloon. It took about 5 or 6 seconds for the participants to

make the decision and/or observe the outcome (either win or lose) on the computer screen. After completing the risk decision-making process, the participants had a 15-second recovery time (Figure 2). Overall, it takes 20 to 21 seconds to finish one block and approximately 5 to 6 minutes to complete an entire fNIRS-BART protocol, in either passive or active mode. More details of the BART protocol is introduced in **Appendix C**.

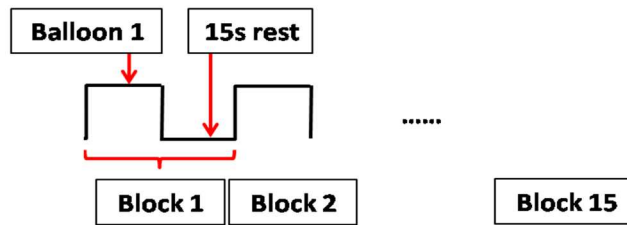


Figure 3-2 Schematic diagram depicting 15 task blocks. Each block includes an activation period (5 to 6 seconds, variable among participants) and a 15-second recovery time.

3.4 Experimental setup

3.4.1 Participants and paradigms

Nine healthy right-handed subjects (5 males and 4 females, between 25-39 years) were recruited for this study. Written informed consents were obtained from all the subjects; the study protocol were approved by the University of Texas at Arlington Institutional Review Board. All the subjects were scanned twice with the mean test-retest interval of three weeks. No subjects reported any known diseases, such as musculoskeletal, neurological, visual, or cardio-respiratory dysfunctions. A continuous wave (CW) fNIRS brain imaging system (Cephalogics, Ishington Univ., USA) was applied to each subject's forehead to record the hemodynamic variation during risk decision-making tasks (Figure 3-3). The mobile optical tracking unit (MOTU) included two sets of 24-bit A/D conversion with 96 kHz sampling rate. The detector boxes included 24 sets of Hamamatsu c5460-01 avalanche photo diodes, with the noise equivalent power (NEP) $< 4 \times 10^{-14} \text{ W}/\sqrt{\text{Hz}}$ and the dynamic range $> 10^6$. Each source fiber included three 750 nm

LEDs power and one 850 nm LED. The powers of LED sources were set approximately 1.2 mW and 1.6 mW for 750nm and 850nm wavelengths, respectively. Note that a total 24 sources and 24 detector channels were provide by this device. The signal-to-noise-ratio (SNR) was kept lower than 5% for each channel before data acquisition.

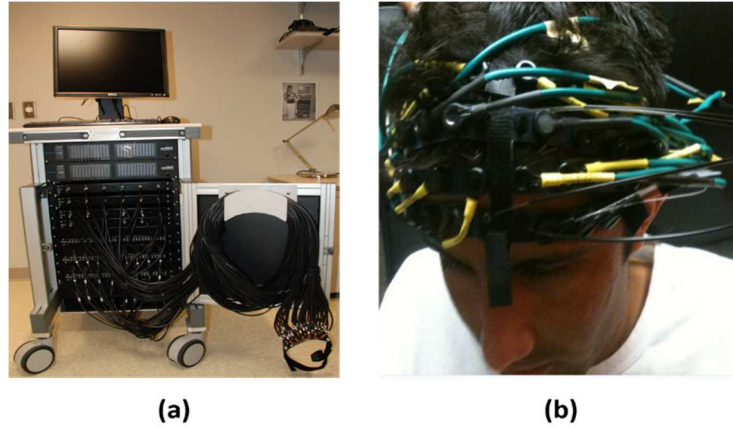


Figure 3-3 (a) Continuous wave (CW) fNIRS brain imaging system (Cephalogics, Ishington Univ., USA); (b) Optode placement on a participant's forehead.

The detected fNIRS signals were acquired in the frequency of 10.8 Hz over PFC areas continuously. Oxygenated hemoglobin (ΔHbO) and deoxygenated hemoglobin (ΔHHb) were computed through two wavelengths. fNIRS optode array used in this study consists of 12 sources and 16 detectors with a nearest inter-optode distance of ~ 3.25 cm, forming 40 measurement channels totally and covering the forehead entirely, as seen in Figure 3-4 (b). Figures 3-4(a) shows the probe geometry overlaid on the anatomical images of a human brain template in the PFC and frontal cortices. Specifically, the areas covered by the fNIRS probes are mainly over the Brodmann area (BA 10, BA9, and part of BA46; [83]). For this test-retest reliability study, only active mode was considered since passive mode does not induce much significant changes in hemodynamic signals in the frontal cortex of each subject [16]. Hemodynamic responses along two cases in the

outcome phases (namely, win and lose) were measured for each subjects. Average hemodynamic changes were quantified by the atlas-DOT algorithm (details see chapter 2).

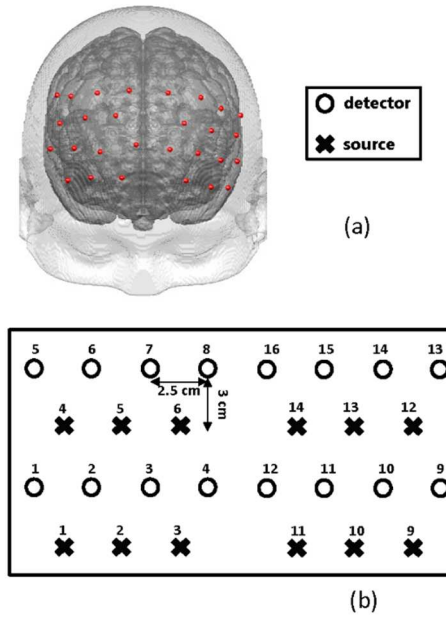


Figure 3-4 (a) Optode locations co-registered to the ICBM152 brain template; (b) the geometry of the probe, where circles represent the detectors and crosses represent the sources.

3.4.2 Data processing

The raw temporal data was first put into a band-pass filter (0.03 Hz for high-pass corner and 0.2 Hz for low-pass corner) to remove instrument drift and physiological noises [84]. Then a block-average process was performed to the data in order to enhance the signal-to-noise ratio (SNR). The atlas-DOT was used to generate the reconstructed 3D images after the preprocessing. More details of atlas-DOT are introduced in Chapter 2. To identify the activated areas and volumes in the cortex, the regions of interest (ROI) were defined or identified based on the reconstructed ΔHbO

values from the voxels within the field of view (FOV) by the 9 cm × 20 cm optode-covered area (see Figure. 3-2). As mentioned above, 12 sources and 16 detectors (with a nearest inter-optode distance of 3.25 cm) formed 40 measurement channels, which enable to form voxel-wise DOT with a detection layer up to 3 cm. Any voxel with a ΔHbO value higher than a half of the maximum ΔHbO determined over the FOV would be included or counted within the ROI. Namely, the ROIs are selected using the full-width-at-half-maximum (FWHM) approach based on a single maximum ΔHbO value across both cortical sides of FOV.

3.5 Results

3.5.1 Hemodynamic Response under BART Stimulation

In our experimental study, the BART risk decision-making task is performed by the nine young healthy participants twice (visit 1 and visit 2). ΔHbO values within the FOV are computed during each visit. The activated pixels are extracted by the FWHM threshold. Figure 3-5 shows the reconstructed ΔHbO maps of brain activations on the cortical surface with three different views: coronal (left), sagittal (middle) and axial (right). This figure clearly illustrates the brain activation areas in both visits for “win” (upper image) and “loss” (bottom image) cases. The group averaged activated pixels are highlighted as red (for visit 1) and yellow (for visit 2). All responses to BART from visit 1 and visit 2 robustly evoked hemodynamic signal increases in their respective anatomical target regions. It is observed that both “win” and “loss” cases in the two visits revealed strong positive activations in both left and right DLPFC regions.

Specifically, there is a more focused brain activation region in the “win” case than in the “loss” case in visit 1 (Figure 3-5, red) and visit 2 (Figure 3-5, yellow). Also, all brain images revealed a higher left DLPFC activation level and a bigger area than those in the right DLPFC region. These results, which are consistent with reported findings in the

literature, suggest that specific neural regions (the lateral PFCs and dorsal anterior cingulate) support cognitive control over thoughts and behaviors, and that these regions could potentially contribute to adaptive and more risk-averse decision making [16], [82].

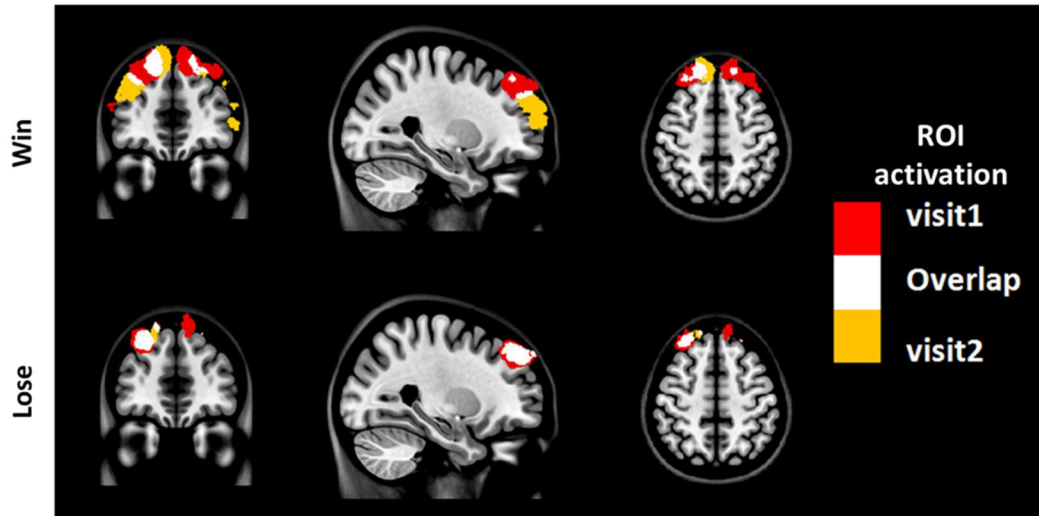


Figure 3-5 Coronal, sagittal and axial view of fNIRS activation group level maps from visit 1 (red), the overlap (white), and visit 2 (yellow). Upper images show reaction areas under the “win” stimulus, while bottom images represent those under the “lose” stimulus.

To test the statistical differences between visit 1 and visit 2, a pairwise t-test is performed to the mean amplitude in both “win” and “lose” cases. Figure 3-6 shows the mean and standard deviation of the group level ΔHbO values. No significant difference is found in both the “win” ($1.42 \pm 0.39 \mu\text{M}$ in visit 1 and $2.12 \pm 0.34 \mu\text{M}$ in visit 2, $n = 9$, $p\text{-value} = 0.19$) and “lose” case ($2.97 \pm 0.90 \mu\text{M}$ in visit 1 and $2.74 \pm 0.59 \mu\text{M}$ in visit 2, $n = 9$, $p\text{-value} = 0.84$). The results indicate that there is no significant difference between the two visits at the group-mean amplitude level.

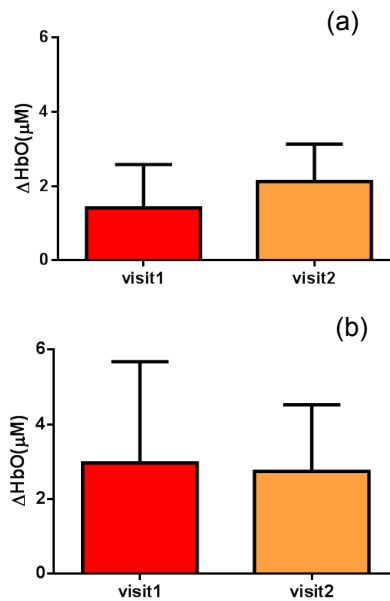


Figure 3-6 Bar plots of mean amplitude for two visits in (a) "win" and (b) "lose" case.

The individual activation maps (coronal view) of the subjects are displayed in Figure 3-7. The upper images show activation areas in the "win" case, and the bottom images represent activation areas in the "lose" case. Compared to the group level results (Figure 3-5), the individual level activation maps reveal a more diverging pattern. In general, most of the subjects demonstrated a strong activation in the Brodmann's Area (BA) 9 bilaterally and the dorsolateral prefrontal cortex (DLPFC). Table 3-6 lists the mean amplitude of ΔHbO over activated pixels of each subject, which will be used for reliability assessment in the following subsection.

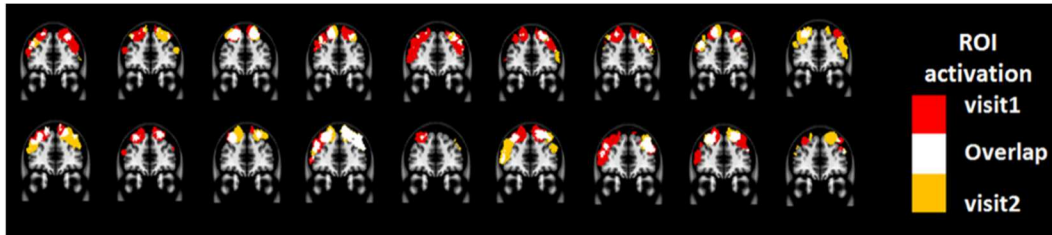


Figure 3-7 fNIRS activation subject-specific cerebral activation maps from visit 1 (red), the overlap (white), and visit 2 (yellow). Upper images show reaction areas under the “win” stimulus, and bottom images represent those under the “lose” stimulus.

Table 3-6 Individual level mean ROI HbO (μM)

Subject(ID)	Win (ΔHbO in μM)		Lose (ΔHbO in μM)	
	Visit 1	Visit 2	Visit 1	visit2
1	1.04	3.27	1.74	0.68
2	4.15	3.95	5.06	4.86
3	2.36	2.25	6.58	5.62
4	1.09	1.36	1.56	3.80
5	0.64	1.59	7.68	2.28
6	0.92	1.02	0.92	0.58
7	0.70	1.08	0.44	1.34
8	0.45	1.87	1.20	2.30
9	1.39	2.69	1.58	3.24

3.5.2 Reliability Assessment Using Intraclass Correlation Coefficient

To assess the test-retest reliability of fDOT in the two cases (“win” and “lose”), we computed the six forms of ICC as defined in Table 3-5 using the mean ROI-based $\square\text{HbO}$ values in Table 3-6. The values of the ICCs are presented in Table 3-7. Note that $k=2$ in this study. It is observed that in the “lose” case, the ICCs of a single measurement and ICCs of the average measurement are relatively consistent, whereas those in the “win” case vary considerably and thus will lead to different conclusions. For example, if $\text{ICC}(1,1)$ is used, we would conclude that the test-retest reliability is fair ($0.4 < \text{ICC} < 0.6$), while if $\text{ICC}(3,1)$ is used, a good reliability ($0.6 < \text{ICC} < 0.75$) could be concluded. This clearly illustrates the necessity and importance of ICC selection as discussed in the Introduction.

Table 3-7 Intraclass correlation coefficients with 95% CI for assessing test-retest reliability

Task	ICC(1,1)	ICC(2,1)	ICC(3,1)	ICC(1,2)	ICC(2,2)	ICC(3,2)
Win	0.58(-0.05,0.89)	0.61(-0.02,0.90)	0.72(0.16,0.93)	0.73(-0.01,0.94)	0.76(-0.04,0.95)	0.84(0.27,0.96)
Lose	0.56(-0.08,0.88)	0.54(-0.19,0.88)	0.52(-0.17,0.87)	0.71(-0.18,0.93)	0.7(-0.46,0.94)	0.68(-0.41,0.93)

The appropriate ICCs in the two cases can be determined following the guidelines summarized in Section 3.2.2:

Guideline i: Since the experimental conditions for all subjects are the same in each visit, this rule does not apply here.

Guideline ii: To decide whether to choose the one-way model or two-way model, we conducted two-way ANOVA analysis to find the significance of between-tests variance. The resulting ANOVA tables in the “win” case and “lose” case are given in Tables 3-8 and 3-9, respectively. In the “win” case, the p-value of the F test is 0.03, indicating that the between-tests variance is significant (assuming significance level=0.05). The calculated magnitudes of the ICCs have the order of $ICC(1,1) < ICC(2,1) < ICC(3,1)$, which is consistent with Property 2 given in Section 3.2.2. According to Guideline ii, the two-way model should be chosen in this case. In the “lose” case, the p-value is 0.77, indicating the insignificance of the between-tests variance. The magnitudes of the ICCs are close to each other, which is also consistent with Property 2. By Guideline ii, ICCs based on any of the three models can be used in this case.

Guideline iii and iv: A further determination is needed on whether to choose the two-way random-effect model or mixed-effect model for the “win” case. First, we believe that the systematic error of our experimental system is random (assuming minimal

learning effects in our study since the time interval between the two visits is long enough) and results in this study can be generalized to all possible tests on the system. Such a generalization is also desirable as the ultimate goal of our study is to test the general feasibility of the fDOT as a tool for assessing risk decision-making. Second, we concern the absolute agreement of measurements in the test-retest reliability analysis. By Guideline iii, ICCs based on the two-way random-effect model should be used.

Table 3-8 ANOVA table* in the “win” case

Source	df	SS	MS	F	p-value
Test	1	2.23	2.23	6.62	0.03
Subject	8	16.43	2.05	6.09	0.01
Residual	8	2.70	0.34		
Total	17	21.37			

*: Summary of ANOVA results which is standard output from software.

SS: sum of squares; MS: mean squares; $MS=SS/df$

F: statistic in the F test

Table 3-9 ANOVA table in the “lose” case

Source	df	SS	MS	F	p-value
Test	1	0.24	0.24	0.09	0.77
Subject	8	63.85	7.98	3.14	0.06
Residual	8	20.34	2.54		
Total	17	84.43			

In summary, ICC(2,1)/ICC(2,2) should be used in the “win” case, and any of the three types of ICCs, i.e., ICC(1,1)/ICC(1,2), ICC(2,1)/ICC(2,2), ICC(3,1)/ICC(3,2), could be used in the “lose” case. Based on the values of the chosen ICCs in Table 3-7, we conclude that in the “win” case, a single measurement has fair reliability and the average of test-retest measurements has good reliability, while in the “lose” case, a single measurement has fair reliability and the average of test-retest measurements has good

reliability. Note that in Table 3-7, ICCs of the average measurement are always larger than their counterparts based on a single measurement, which is consistent with Property 3 in Section 3.2.2. However, in the practice, we should always choose the ICC matrix in a consistent way to deal with the same data set. As showed above, only ICC(2,1)/ICC(2,2) matrix are fitted for “win” case, we should ignore other options (e.g. ICC(1,1)/ICC(1,2) and ICC(3,1)/ICC(3,2)) of ICC matrix and select only ICC(2,1)/ICC(2,2) for “lose” case to keep consistency.

3.6 Discussion

3.6.1 Simple Procedure for ICC Selection

To provide convenience in practice for test-retest reliability assessment of neuroimaging measurements, the guidelines given in Section 3.2.2 are summarized into a simple procedure for ICC selection considering general settings in neuroimaging studies. The flow chart of the procedure is shown in Figure 3-6. The procedure consists of two steps. *Step 1* is to determine if the “Test” effect is negligible. At this step, the unified ANOVA model (i.e., two-way random-effect or two-way mixed-effect ANOVA model) would be constructed using the actual data. The significance of the between-tests variance is indicated by the p -value which is often given as part of the ANOVA output. If it is not significant, it means that the “Test” effect is negligible. Accordingly, the one-way random-effect model should be chosen, and ICC(1,1)/ICC(1, k) are the appropriate reliability measures. If the between-tests variance is significant, then the “Test” effect is not negligible, and thus two-way models should be used. *Step 2* is to determine whether the “Test” effect is random. Expert knowledge on the experimental system will be used to make the decision. If the systematic error is believed to be random, then the two-way random-effect model should be chosen and ICC(2,1)/ICC(2, k) are appropriate reliability measures. If the researcher is not sure about the distribution of the systematic error or

suspects a certain pattern to exist, then the two-way mixed-effect model should be chosen and ICC(3,1)/ICC(3,k) are the appropriate reliability measures.

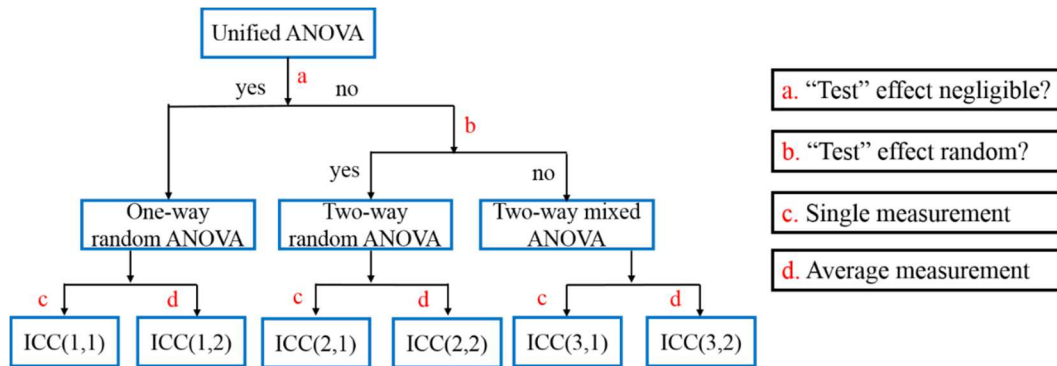


Figure 3-8 Flow chart of the procedure for ICC selection

Two things need to be kept in mind when applying the above procedure for ICC selection in practice: (1) If the "Test" effect is found to be negligible in Step 1, the three models will yield similar ICC values, so any of them can be used in reliability assessment of measurements as pointed out by Guideline ii. The one-way model is suggested in the procedure because it is appropriate in the sense of model building. (2) Due to the subjectivity involved in the choice between the two-way random-effect versus mixed-effect model, the decision might be debatable in some cases. In fact, such debates widely exist among researchers in many other fields [57], [58]. So finding an absolutely better model is not very meaningful here; the key is to make sure that the same model is grounded in comparing the reliability of neuroimaging modalities.

3.6.2 Pitfalls in Test-retest Reliability Assessment

There are some special issues that may arise in assessing test-retest reliability of measurements using ICCs. The first issue is negative reliability estimates. Since ICCs are defined to be the proportion of between-subjects variance, they should range from 0 to 1 theoretically. In practice, however, due to sampling uncertainty, the calculated values of ICCs may be out of the theoretical range such as being negative. To be meaningful,

negative ICC values can be replaced by 0 (e.g., [85]). The second issue is dependence of ICCs on between-subjects variance. According to the definitions of ICC in Eq. (3-10) and (3-11), the value of ICCs depends on the between-subjects variance. When the between-subjects variance is small, i.e., subjects differ little from each other, even if the measurement error variance is small, the ICC may still be small; on the other hand, large between-subjects variance may lead to large ICCs even if the measurement error variance is not small. For example, considering ICCs defined by Eq. (3-11), if between-subjects variance=0.2 and random error variance=0.3, $ICC=0.2/(0.2+0.3)=0.4$; if between-subjects variance=3 and random error variance=1, $ICC=3/(3+1)=0.75$. Taking into account the magnitude of the between-subjects variance and random error variance, the former ($ICC=0.4$) might be acceptable, while the latter ($ICC=0.75$) might not be satisfactory in some applications. So the meaning of ICCs is context specific [59], and it is not adequate to compare the reliability in different studies only based on ICCs. The final issue is significant between-tests variance. When ANOVA indicates that the between-tests variance is significant, the value of ICCs may still be large, indicating good reliability. However, the significant between-tests variance is not desirable and efforts need to be made to reduce the systematic error of the test. For example, protocols of the study may be modified to eliminate the learning effects of the test [86].

Moreover, in the broad range of fNIRS study, there is always facing the extra-cranial issue that may exert errors to fNIRS measurement [87]–[89]. Also, there may be more influential from physiological noise than the brain activation, or brain activation is unstable under certain stimulation [90]. However, as a test-retest reliability study, especially in the topic of intraclass correlation coefficient, some effects may not be so essential. We are considering the anatomy within subject is stable during the two-week test-retest period. In this case, the variation due to the scalp-cortex distance could be

ignored. Thus, the first concern, which count on the scalp-cortex variation, may not be the major error source in the test-retest reliability study. In addition, data processing methods could be introduced to further minimize the extra-cranial signal effect. A recent study introduces an easy-to-use filter method, which use all fNIRS channels to subtract the extra-cranial signal channel, and shows a substantial improvement on the forehead measurement [91]. Moreover, a double short separation measurement approach based on the short-distance regression could also be introduced to reduce the noise for both HbO and HbR signal [92].

3.7 Summary

Choosing appropriate forms of ICC is critical in assessing measurement reliability of neuroimaging modalities. Wrong choice of ICCs will lead to misleading conclusions. In this study, I have reviewed the statistical rationale of ICCs and provided guidelines on selecting appropriate ICCs from the six popular forms of ICC. Also, using a risk decision-making protocol, we have demonstrated how to select appropriate ICCs and assess the reliability of fDOT-based brain imaging measurements following the given guidelines. While this study provides a statistical approach to assess test-retest reliability of fDOT measurements, its understanding and guidelines of ICCs are applicable to other neuroimaging modalities. Better comprehension on ICCs will help neuroimaging researchers to choose appropriate ICC models, perform accurate reliability assessment of measurements, and make optimal experimental designs accordingly.

Chapter 4

Implement of General Linear Model in Atlas-DOT

4.1 Introduction

The conventional way of defining brain activation induced by stimulation tasks in DOT [14]–[16] involves the following steps: (1) defining the maximum activation period in a time series of HbO (and HbR) readings from the fNIRS measurements; (2) reconstructing temporally-averaged DOT images over the chosen activation period; (3) determining the region of brain activation by full width of half maximum (FWHM) in reconstructed images; and (4) comparing the HbO values within the defined activation region between the two states (i.e., “rest” versus “task”) with a paired t-test to determine if the changes between the two states are statistically significant. However, this method used for DOT has a significantly limitations: the maximum activation or post-activation period had to be subjectively defined without much statistical or mathematical basis.

To overcome this limitation, many research groups have followed an analysis method commonly utilized by fMRI researchers, namely, the general linear model- (GLM-) based analysis [27], [29], [30], [91], [101]. It examines whether or not the experimental fNIRS data and a designed linear model are matched over the entire experimental time course. This approach rests on a physiology-based principle or model that hemodynamic signals measured in response to brain stimulation result from a convoluted effect between the stimulation task and hemodynamic response function (HRF), where the latter two functions are already given. Thus, there is no need to subjectively select the activation and/or post-activation period in order to determine the activation regions in the brain. This is why GLM-based analysis has been developed and popularly utilized for topographic image analysis [37], [83], [94].

In this chapter, I combined atlas-DOT (Chapter 2) with GLM-based analysis (voxel-wise GLM analysis) to form volumetric brain activation images under a specific risk decision-making task, the Balloon Analogue Risk Task (BART). BART is intentionally chosen as a demonstrative example in this study since it is a valid experimental protocol and has been commonly used in the field of neuroscience as a behavioral measure to assess human risk-taking actions and tendencies while facing risks. Background development, administration, and psychometrics of BART are introduced and discussed in our previous study [16], without using any novel image process and analysis approaches developed in this study. The novelty of this paper rests on the combination of three image processes, namely, (1) brain atlas guided DOT, (2) application of DCA to DOT image reconstruction, and (3) voxel-wise GLM-based analysis. This combined approach enables us to optimally obtain reconstructed volumetric DOT images with much improved spatial resolutions and 3D visualization on a human brain template, which is particularly useful for studying cognitive responses to risk decision-making. To our knowledge, this is the first report on brain atlas guided, GLM-driven, volumetric DOT to image the human frontal cortex in response to cognition-related stimulations.

4.2 Implement of general linear model in atlas-guided diffuse optical tomography

4.2.1 *General linear model*

The general linear model (GLM) is a hypothesis-driven model to define the brain activation with rigorous statistical analysis, which is initially utilized in fMRI and then in fNIRS data analysis in recent years [17], [20], [37], [83], [93]. The GLM-based analysis examines whether or not the experimental data and a designed linear model are matched over the entire experimental time course. The basic principle of GLM is expressed as:

$$Y = \sum_{i=1}^n X_i \times \beta_i + \varepsilon \quad (4-1)$$

where Y is the data matrix containing the observed signals at various time points at single voxel. X_i is the i th designed or modeled hemodynamic response matrix (or the i th regressor) with components explaining the observed data/signal; β_i is the amplitude or parameter defining the contribution of X_i to the observed data; the subscript i denotes the number of regressors used in the model; ε is the error matrix containing the difference between the observed data Y and predicted data by the model of $\sum_{i=1}^n X_i \times \beta_i$. In any fNIRS study, the observed data/signals could be changes of hemodynamic parameters, including ΔHbO , ΔHbR , and ΔHbT . Only ΔHbO is utilized as the observed data for further data analysis in this study since the magnitudes of ΔHbR are much smaller than those of ΔHbO .

In general, design of regressors is based upon the experimental protocol, including the timing and duration of the stimulation given. In this study, the BART paradigm included a baseline, a ~5-sec performance or stimulation period, followed by a 15-sec recovery period. During the BART performance in active mode, two kinds of stimulations occurred: the first is the stimulation due to deciding and performing balloon inflations (decision-making/performance phase); the second is the stimulation due to reaction to "win" or "lose" outcome (reaction phase). To investigate the brain responses to these two different stimulations during BART, we selected a mixed block/event-related design to model the two stimulations associated with BART [95]. The first regressor is created using a blocked design, having a boxcar of 5 sec to cover the decision-making/performance phase (regressor 1; blue dashed line in Figure 4-1a). The second

regressor is formulated with an event-related design, with a short period of boxcar of 0.5 sec to reflect the reaction phase (regressor 2; red dashed line in Figure 4-1a). The latter one simulated particularly the evoked hemodynamic response when subjects observed the win/lose outcomes. Both regressors are calculated after convolving the stimulation function and HRF [96] to represent overall responses in the brain, as illustrated in Figure 4-1a.

After the regressor is constructed, the time course of ΔHbO at each voxel within the human head template, which is reconstructed using brain atlas guided DOT, is fitted to eq. (6) using ordinary least squares (OLS) estimation [97]. The optimal parameters, β_i 's, are calculated as:

$$\beta_i = (X_i^T X_i)^{-1} X_i^T Y \quad (4-2)$$

where $i=1, 2$ are in response to the decision-making/performance phase and to the reaction

phase, respectively (see Figure 4-1a; regressors 1 and 2). The t-statistics are then calculated by:

$$t = \frac{c^T \beta}{\sqrt{\text{Var}(\varepsilon) c'(X'X)^{-1} c}} \quad (4-3)$$

where c represents the contrast vector ($c = [1,0]$ for decision-making/performance phase and $c = [0,1]$ for reaction phase); the denominator in eq. (4-3) represents the standard error of $c^T \beta$ [98]. This process mentioned above is performed voxel by voxel in order to identify the specific cortical regions which are activated by two separate stimulations (decision-making/performance phase and reaction phase) due to BART. In general, an assumption within GLM is that any noise/error shown at one time point is not correlated from that at another time point. The degree of freedom to compute

the significance in the t-test can be calculated by the number of observations minus the number of regressors if this assumption is met. However, this assumption does not hold for most cases in fMRI time-series analysis as well as in our study [99]. This can lead to biased t-statistics and affect accuracy of the conclusions. To correct this issue, we have applied the autocorrelation calculation which is introduced by Worsley and Friston [99]. The effective degree of freedom v to compute the p-value in t-distribution is calculated as:

$$v = \frac{\text{trace}(RV)^2}{\text{trace}(RVRV)} \quad (4-4)$$

where V is the autocorrelation matrix, and R represents the residual matrix and is expressed as:

$$R = I - X(X^T X)^{-1} X^T \quad (4-5)$$

Then, the t-statistics are calculated by:

$$t = \frac{c^T \beta}{\sqrt{\sigma^2 c^T (X^T X)^{-1} X^T V X (X^T X)^{-1} c}} \quad (4-6)$$

where σ^2 is the variance of the estimate parameter for each voxel and is calculated by [99]:

$$\sigma^2 = \frac{(RY)^T (RY)}{\text{trace}(RV)} \quad (4-7)$$

Since this study involved multiple participants, inter-subject variation would exist. Thus, we further performed the random-effects analysis [98], [100].

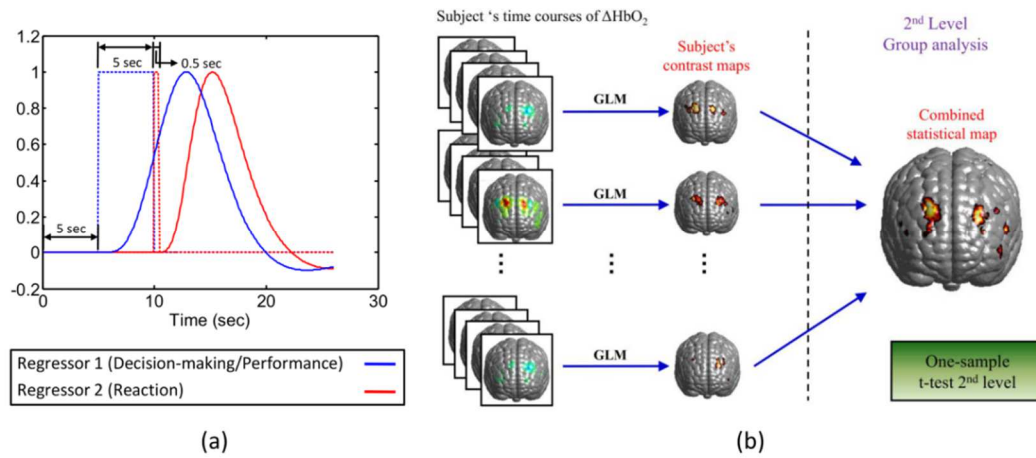


Figure 4-1 The schematic illustrations of an experimental design of BART and the random-effect analysis. (a) A schematic of protocol and regressor design of BART. (b) Schematic diagram of two-stage random-effects analysis.

In principle, random-effects analysis contains two stages of analysis operations: single-subject analysis and group-level analysis, respectively, as demonstrated in Figure 4-1(b). In this Chapter, for the first-level (i.e., single-subject) analysis, I generated a contrast map of β -values or t-statistics on the voxel-wise atlas template for each subject. For the second level (i.e., group-level) analysis, the one-sample, t-test on β -values was performed voxel by voxel within the reconstructed image volume over all the participants. The outcome of this group-level random-effects analysis gave rise to statistically meaningful brain activation maps for both phases in response to BART stimulation.

4.2.2 Strategies of GLM-based atlas-DOT algorithm

GLM approach were implemented into atlas-DOT to form up a solid fNIRS data analysis routine for high-order neurological test. As discussed in chapter 2, atlas-DOT technique can significantly improve the fNIRS image spatial resolution and depth information. In addition, mixed/event-related GLM approach was able to monitor complex neurological signals in complex protocol. Thus, combination of these two algorithm

provide us an optimal tool of investigation high-order cognitive functions along aging effect.

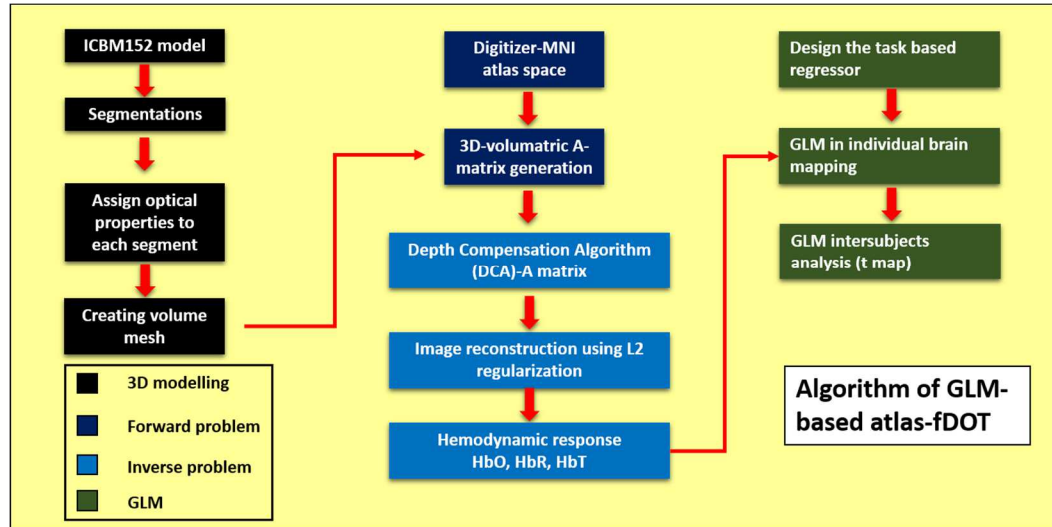


Figure 4-2 Procedures of GLM-based atlas-guided diffuse optical tomography

Implementations of GLM analysis into atlas-fDOT was to perform the general GLM routines after the inverse problem. As showed in Figure 4-2, the first three steps, which were 3D-modeling, forward problem and inverse problem, were represented the same procedures showed in Chapter 2 (Figure 2-3). Additional steps, which showed in dark green color in Figure 4-2, represented the GLM analysis. There were three main steps included in GLM analysis, names, design of regressor, linear model fitting and t statistics.

In the design of regressor, a mixed/event-related model was defined based on the BART protocol (as showed in Chapter 3.3). Figure 4-3 displays the experimental protocol and the regressor design. For each block, the first 5 to 8 seconds were considered the decision-making phase and was modeled by “Reg1” as showed in Figure 4-3(c). Reg2 (Figure 4-3d) was the outcome phase—a quick peek stimulation phase. In the decision-making phase, the participants were actively inflating the balloon (Figure4-

3(a), left side). Subject-specific regressor (Reg1) was used to model this phase since every participant had a decision-making period per balloon; time varied from 3 to 10 seconds. In the outcome phase, participants faced either a win or lose outcome. Notice that this phase began with the sudden appearance ($<1s$) of the phrases “You Win!!” or “You Lose!!” image in the center of the monitor (Figure 3(a), right side), a quick stimulus (Reg2) was applied to model this phase more accurately.

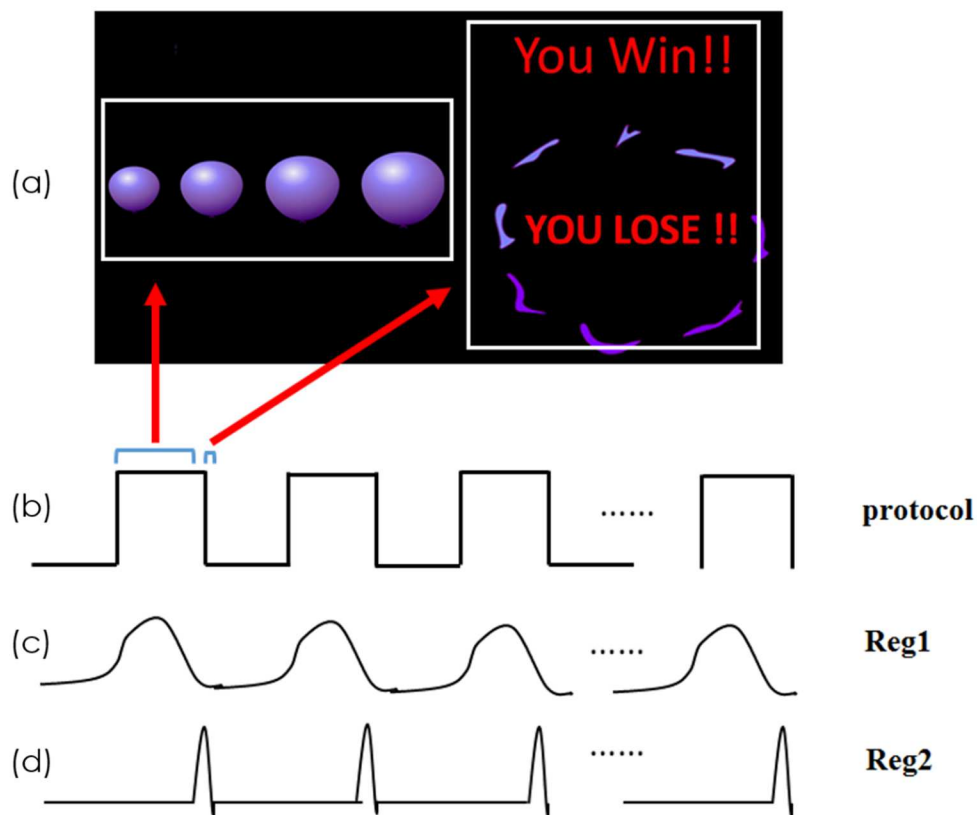


Figure 4-3 Experimental protocol and regressor design. (a) The BART protocol for decision-making phase (left) and reaction phase (right); (b) block design of the BART protocol; (c) illustration of regressor for the decision-making phase; (d) illustration of regressor for reaction phase.

After design of regressor, A 3D map corresponding to estimated regressor response amplitudes was generated by applying first-level temporal general linear model (GLM) fitting. The conventional ordinary least squares (OLS) estimation was applied to the voxel-wised ΔHbO data [97]. Specific cortical regions which were activated by two separate stimulations (decision-making/reaction phase) were then identified by the t -statistics. Prior to the use of GLM fitting, major issue that could lead to bias or over estimations of the functional data were recognized [99], [101], [102]. The first issue was the temporal correlated residuals of GLM due to some un-modeled physiology or structural noise. For the majority of functional brain imaging data, this could be the un-flitted intrinsic brain activities, heart beats or respirations [103], [104]. This effect could also vary the degrees of freedom that affect the accuracy of conclusions in t -tests [102], [105]. To deal with this, an autocorrelation matrix was applied to correct the OLS estimation [99]. Then, a false discovery rate (FDR) was applied to obtain the corrected degrees of freedom [106]. In this chapter, I chose $p < 0.05$ (FDR corrected) as a threshold to obtain the activation regions.

Group mean t -maps of both decision-making phase and outcome phase were obtained through random effect analysis for both gender and age group. Results were plotted and arranged by male/female in the gender-effect analysis, and with young/older pairing in the age-effect comparisons. Mean amplitude (μM) within the significant activated regions were quantified for further statistical analysis.

4.3 Participants and experimental setup

Forty young adults (17 female, 23 male, average age = 29) participated the BART measurement. Details of participant demographic information including gender, age, highest education level and blood pressure measures were presented in Table 4-1.

All subjects were recruited from the department of bioengineering and college of nursing at the University of Texas at Arlington.

Table 4-1 Participant Demographic Information

Demographics	Results
Age in Years Mean (SD; Range)	Total Sample: 28.8 (5.4; 25-44) yrs. Males: 29.2 (5.9; 25-44) yrs. Females: 28.5 (4.7; 25-42) yrs.
Gender Frequency (%)	Males: 23 (57.5%) Females: 17 (42.5%)
Highest Level of Education Achieved Frequency (%) Missing Data: n=8	High School/GED: 1 (3.1%) Some College: 1 (3.1%) Associate Degree: 1 (3.1%) Bachelors Degree: 12 (37.5%) Masters Degree: 13 (40.6%) Doctoral Degree: 4 (12.5%)
Major in School Frequency (%)	Engineering: 25 (62.5%) Science: 5 (12.5%) Business: 4 (10%) Nursing: 4 (10%) Other: 2 (5%)
Blood Pressure—Systolic and Diastolic Mean (SD; Range)	Total Sample: Systolic 118.8 (10.7; 81-137) Diastolic 65.7 (8.9; 43-87)) Males: Systolic 121.1 (9.9; 106-137) Diastolic 67 (9.6; 48-87) Females: Systolic 115.6 (11.3; 81-130) Diastolic 63.9 (7.6; 43-75)

The changes in blood hemoglobin concentration were measured using a multi-channel fNIRS brain imager (Cephalogics®), the most updated version of fNIRS systems which has an ability to afford high-density source-detector array and a broad dynamic range. Details of image device properties were discussed in chapter 3.4. During imaging,

the subject was required to sit in a comfortable chair in front of a laptop computer. A fiber-optic probe array with 28 soft fibers (12 for sources and 16 for detectors) was placed across each participant's forehead, as seen in Figure 3-1b and Figure 3-2a. The detected fNIRS signals were acquired in the frequency of 10.8 Hz over PFC areas continuously for each protocol (active and passive). Before taking the actual readings, all optodes were checked for adequate contact on each participant's scalp. All participants completed both active and passive runs; it took an average time of 16 minutes including the extra 5-minutes baseline. The order of the two protocols was randomized across participants.

4.4 Results

4.4.1 Active versus Passive Mode in BART Paradigm

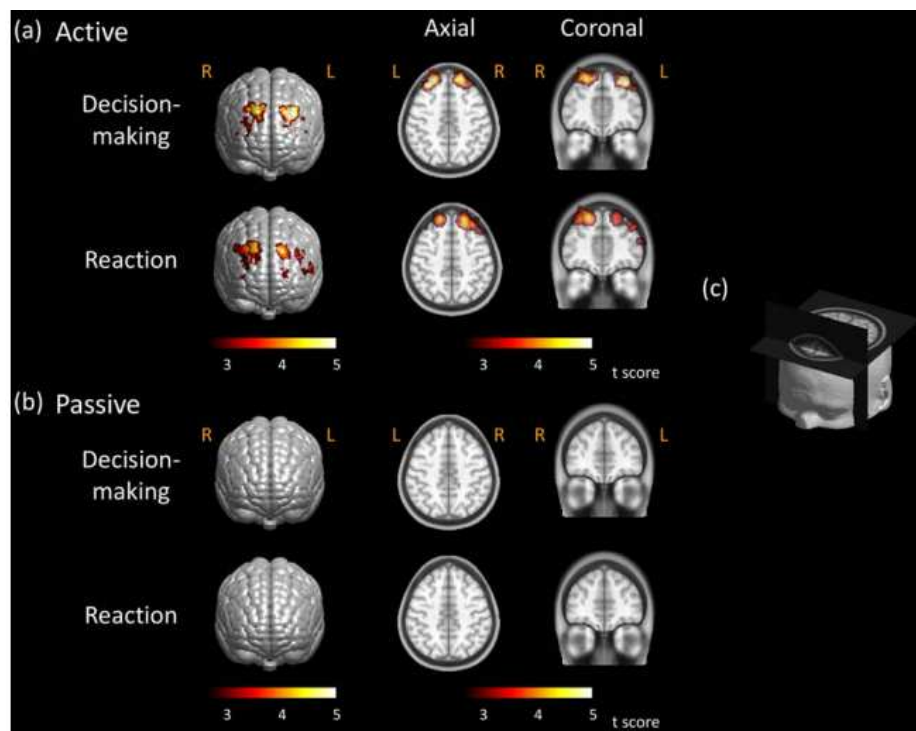


Figure 4-4 Activation images generated at the group-level when performing the (a) active and (b) passive BART modes. (c) Axial and coronal views of activation maps with sliced location

To obtain the brain activation images, changes of HbO concentrations in response to passive and active modes were reconstructed by human-atlas guided 3D-DOT. Group-level, brain activation images (t-maps) were generated by random-effects analysis; a threshold of false discovery rate (FDR) (Genovese, et al., 2002) corrected $p < 0.01$ was used to identify brain activation areas associated with BART. For subjects who performed the active mode of BART paradigm in the decision-making phase, both left and right hemispheres exhibited activations in DLPFC or Brodmann area (BA) 9 and 46 (see upper row of Figure 4.4a). Bilateral brain activations are also revealed on BA 9 and 46 when subjects observed the win/lose outcomes in the reaction phase (see bottom row of Figure 4.4a). The response intensities in the latter phase are a little weaker but more spread as compared to those in the former phase. In addition, the axial and coronal views exhibit that the activations occurred mostly within the cortical regions, exactly where the brain activation in response to BART should take place. On the other hand, no brain activations are shown when subjects performed the passive mode of BART, in both decision-making and reaction phase, as illustrated in Figure 4.4b. Specifically, no activations are present in either axial or coronal views.

4.4.2 Gender Difference in Active Mode

In order to further confirm our developed methodology, we also compared the differences of brain activation associated with BART between male and female participants in active mode. We targeted the comparisons only in active mode since no brain activation is observed in passive mode, as presented in Fig. 4-4b. Voxel-wise GLM is performed for each gender group (male: $N = 21$; female: $N = 16$) after time-dependent volumetric ΔHbO images are reconstructed. Regressors for GLM analysis are generated for decision-making and reaction phases. Random-effects analysis is then performed to

identify the brain activations for each gender at group level; the activation threshold is set to be FDR corrected $p < 0.01$.

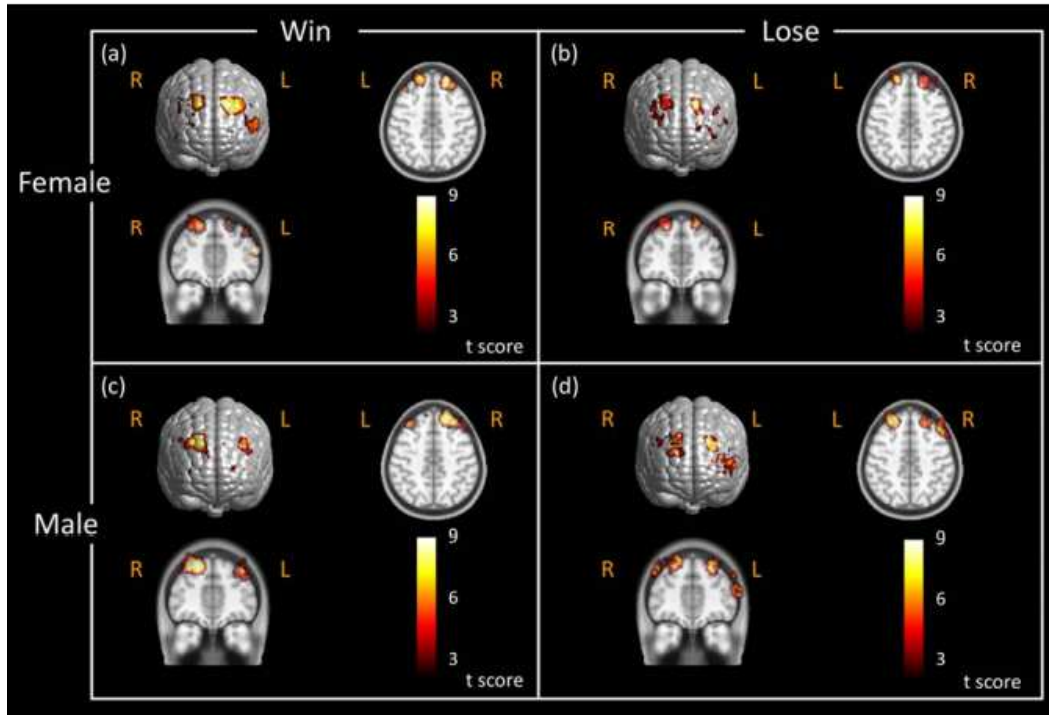


Figure 4-5 Brain activation maps from subjects performing BART decision-making/performance phase with different genders. (a) Female win case; (b) female lose case; (c) male win case; and (d) male lose case. Threshold is set as $p < 0.01$ (FDR corrected). Notice that “R” represents the right and “L” represents the left side of the brain.

During the decision-making/performance phase, we observed bilateral brain activations on DLPFC located on BAs 9 and 46 for both “win” and “lose” cases in female subjects (see Figure 4-5a and b). Bilateral brain activations are also seen on DLPFC in male subjects for “win” and “lose” cases (see Figure 4-5c and d). In “female win” and “male lose” cases, we also noticed similar brain activations in BA 10 on the left DLPFC, as shown in Figure 4-5 (a) and (d). These results implied that the brains behaved

similarly for both genders when they dealt with the BART paradigm in the decision-making/performance phase. This implication might be expected since the subjects did not know the outcomes yet during their performance of BART.

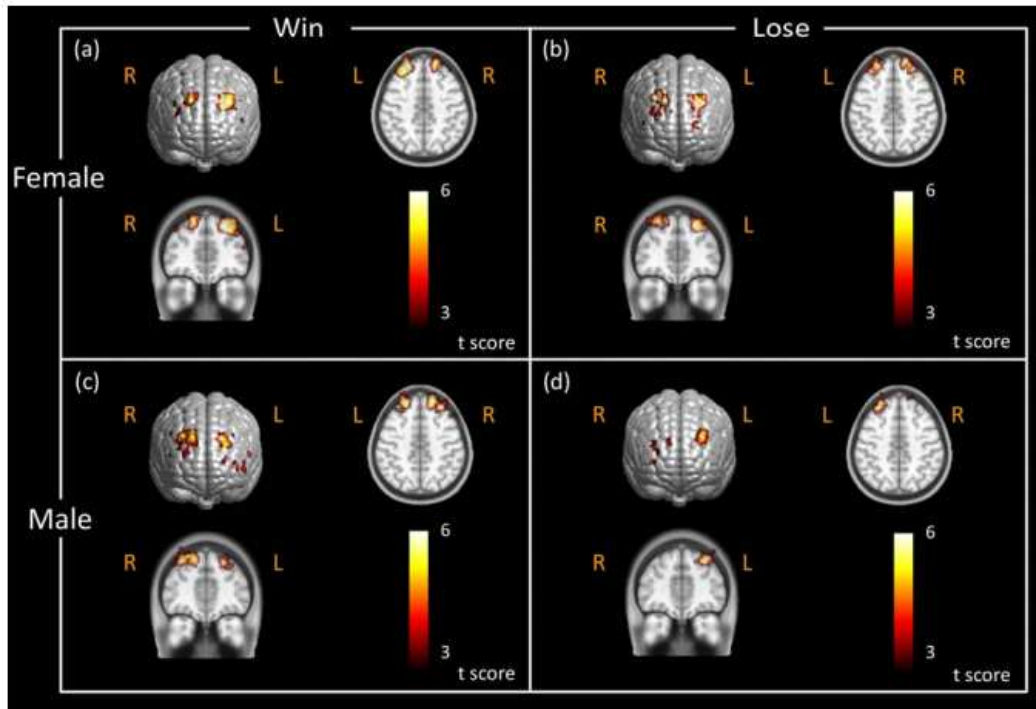


Figure 4-6 Activation images under BART stimulus during outcome phase. Brain activation maps in response to active BART mode when female subjects (N = 21) saw the outcome (a) in the “win” case, (b) in the “lose” case, and when male subjects (N = 16) saw the outcome (c) in the “win” case, and (d) in the “lose” case.

During the reaction phase, we observed strong bilateral cortical activations on or near DLPFC in both male and female subjects (Figure 4-6a and c) in the “win” case. However, in the “lose” case, female participants exhibited clear, bilateral brain activations on DLPFC (Figure 4-6b), while male subjects displayed strong, unilateral activation on the left DLPFC, with little activation on the right DLPFC (Figure 4-6d).

4.4.3 Improvement of Depth Sensitivity by DCA

Earlier in Chapter 2.3, we presented the improvement of depth reconstruction image in a stimulation (See Figure 2-6). Here, to demonstrate the improvement of depth localization when DCA is applied, we utilized a risk decision-making paradigm (BART), as an example, and accordingly investigated the spatial distribution of activation voxels which are derived from voxel-wise GLM analysis across all participants. We analyzed the brain responses to BART only in active mode since no brain activation is observed in passive mode, as previously reported in Active versus Passive Mode in BART Paradigm sub-section (see Figure 4-4). For each subject, the activated voxels induced by BART are identified and selected by GLM analysis, and then the corresponding atlas-guided 3D DOT image is binarized in the following format:

$$V_i = \begin{cases} 1 & \text{where voxel } i \text{ was activated} \\ 0 & \text{otherwise} \end{cases}$$

where V_i represents the i th voxel after GLM analysis in the atlas-guided, 3D image domain. In this way, we are able to generate a brain activation image in a binary form for each subject, followed by summation of such binary activation maps from all of the participants. The outcome of this process resulted in a group-summarized brain activation image by showing the overlapped activation voxels among all the participants, as illustrated in Figure 4-7. Note that the color scale in Figure 4-7 represents the number of overlapping times at each voxel from all the participants. Note that since the number of final participants is 37, the maximum overlapping number should be 37. Figure 4-7(a) and (c) clearly demonstrate that the brain activations in all subjects are mostly located in extra-cerebral regions (as seen from axial, sagittal and coronal views) when DCA is not utilized for 3D-DOT reconstruction. No obvious activations within cerebral regions are

observed for all participants. On the other hand, Figure 4-7 (b) and (d) clearly exhibit much improvement in depth localization, namely, most selected activations are presented within cortical regions for almost all participants when DCA is applied for 3D-DOT reconstruction.

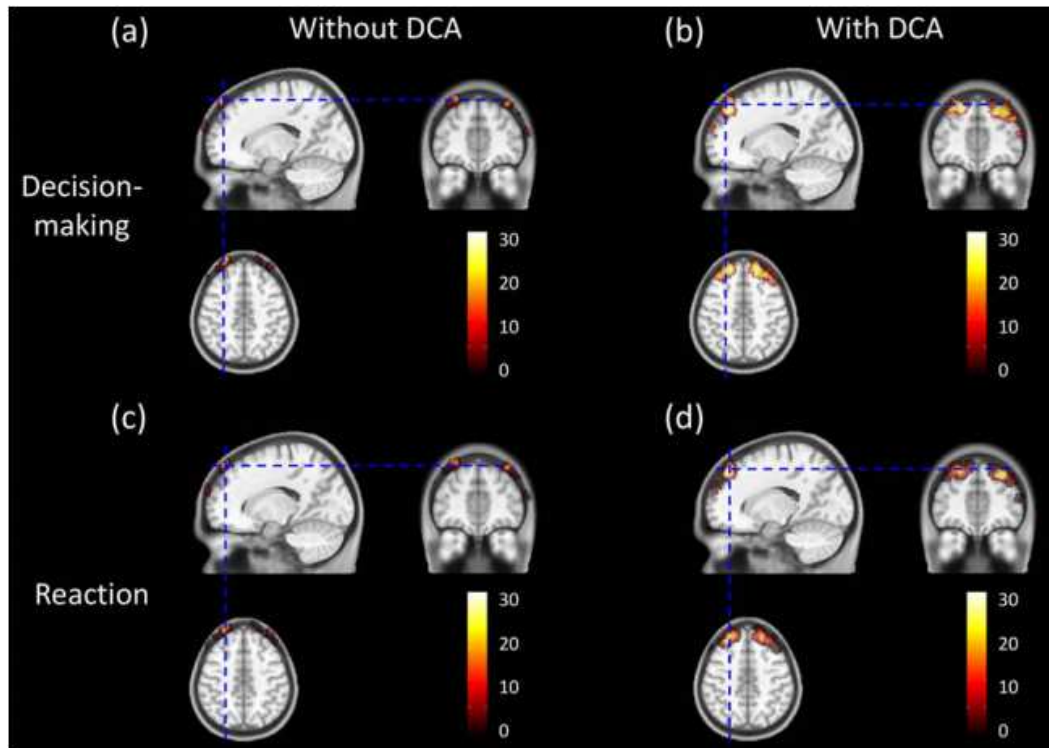


Figure 4-7 Group-level atlas-guided images of overlapped activation voxels across all participants. Shown are a axial, coronal, and sagittal views of brain activations across all participants during decision-making phase and reaction/outcome phase: (a), (c) Without DOCA and (b), (d) with DCA), respectively.

Table 4-2 Activation overlapping ratio between brain and non-brain region

Total		Cerebral region		Extra-cerebral	
<i>Reg1</i>	<i>Reg2</i>	<i>Reg1</i>	<i>Reg2</i>	<i>Reg1</i>	<i>Reg2</i>

Table 4-2—Continued

Without DCA	16043	14668	673 (4.2%)	495 (3.4%)	15370 (95.8%)	14173 (96.6%)
With DCA	24431	22697	22550 (92.3%)	20701 (91.2%)	1881 (7.7%)	1996 (8.8%)

*Reg1: Decision-making/Performance; Reg2: Outcome

Quantitatively, we also performed the voxel-wise based comparisons between GLM-derived activation images with and without DCA applied. The percentages of total voxels representing the brain activation volumes within the cortical/cerebral regions are calculated for both cases, as listed in Table 4-2. From the Table, we observed that approximately 3-4% of total activated voxels (4.2% in decision-making/performance phase and 3.4% in reaction phase) are located within the cerebral region, while approximately 96% of total activated voxels (95.8% in decision-making/performance phase and 96.6% in reaction phase) are located at the extra-cerebral region when the conventional 3D-DOT reconstruction (without DCA adoption) is performed. Dramatic improvement is found when reconstruction with DCA is utilized: 91-92% of total activated voxels resided within the cortical regions. It is noteworthy that approximate 8% (7.7% in decision-making/performance phase and 8.8% in reaction phase) of activated voxels are still outside the brain region even when DCA is applied in 3D-DOT reconstruction. One possible explanation could be related to the selection of adjusted power factor γ since it controls the compensation power and depth sensitivity. We expect the results to improve further if optimization of γ can be further developed. Another possible reason to have brain activation voxels extended beyond the cerebral regions is due to the nature of diffuse light in tissue. Light scattering in tissue consistently makes reconstructed DOT images with smooth or non-sharp edges, extending the image boundaries beyond the true or actual edges of the objects or activated brain areas.

4.5 Discussion

In this paper, we presented the ICBM152 template guided DOT combined with DCA to image hemodynamic changes induced by BART with improved 3D visualization and localization. Moreover, we combined human atlas guided 3D DOT with GLM-based analysis to generate volumetric brain activation images under BART paradigms in the assessment of risk-decision making in 40 young adults. Compared to conventional FWHM-based analysis in DOT, GLM-based analysis allows for simultaneous modeling of the mixed stimulations so as to distinguish brain signals/activations in response to different tasks. Atlas-guided 3D DOT techniques recently have been established by several research groups. For example, studies including computational simulations [41], [42] and in-vivo human data [40], [44] have demonstrated great improvements in resolution as well as quantification. In addition, quantitative spatial comparisons between DOT and fMRI showed good correlation and match between the two imaging modalities [48], indicating great capability of 3D-DOT to be used for studies on brain cortical activities.

The major drawback of 3D-DOT is its poor depth localization due to the exponential attenuation of measurement sensitivity with increase of penetration depth. While an increase in source-detector separation has been reported to enhance depth sensitivity [107], mathematical models to increase the sensitivity for deep layer/tissue have also been proposed to benefit the image quality of DOT. Boas et al proposed the cortical (or brain) constraint method where DOT voxels located outside the brain/cortical regions are forced to have a sensitivity of zero [45]. This method implied that changes in absorption occurred only within the brain/cortical regions. The spatially variant regularization (SVR) technique, which spatially regularized higher sensitivities near the superficial depth and provided more homogenous spatial and depth sensitivity, has been

utilized for human [40], [44], [108] and animal DOT studies [46]. Moreover, Zhan et al. recently demonstrated the improvement of DOT image quality based on computational simulations when a whole-brain spatial constraint and SVR are utilized simultaneously [41]. Our recently developed depth compensation algorithm (DCA) is another approach to improve the measurement sensitivity along the penetration depth by mathematically counter-balancing the fast decay of sensitivity in deeper layers. Each method may have a different outcome and its own advantage; the comparison of different methods to improve the depth localization is not the scope of this study.

I acknowledge that the sensitivity of DOT measurements is mainly limited by the hardware itself and the nature of light attenuation within tissue. Because of severe loss of detected optical signals from deep tissue, the reconstructed brain activities are often projected toward the superficial layer. We mathematically applied the depth compensation algorithm (DCA) for the Jacobian matrix to counter-balance the sensitivity in depth and also to suppress the hyper sensitivity near the surface. We have demonstrated that reconstruction with DCA did improve the depth localization based on computer simulations as well as the experimental data [47], [109], rather than constrain the reconstructed activities in particular depth. Furthermore, a recent study has demonstrated how DCA alters sensitivity at different depths [110]. A similar Figure is given in Supporting Figure S1, illustrating that higher sensitivities reside more toward extracerebral regions, i.e., skull and scalp, without DCA applied, while compensated sensitivities (with DCA) distribute more ideally for imaging the brain activations.

4.5.1 Comparison with Previous Studies

As we mentioned before, we have modified BART paradigm previously used in fMRI research by Rao et al., 2008 [82]. Our BART protocol closely followed Rao et al.'s design although there are slight differences in passive mode. In Rao et al's design,

participants merely pressed the button to keep inflating the balloon during the protocol while computer decided the end points and outcomes including win or lose. In our passive BART paradigm, participants only pressed the button once at the beginning of each block and then observed the computer performing BART. Each balloon is automatically inflated until the computer stopped the task in win case or balloon exploded in lose case. In terms of data analysis, we have used the atlas-guided, GLM-driven, 3D DOT in this study to determine brain activation regions, which is similar to Rao et al's study. However, Rao et al. utilized the BOLD signals as contrast while we targeted changes in hemoglobin concentrations, especially ΔHbO in this study. Moreover, due to the limited interrogation depth in fNIRS, our study is only focused on the hemodynamic changes on BA 9, 10 and 46 while fMRI investigated the whole brain. Although difference exists between these two studies, our results here in this paper, show strong bilateral activations on DLPFC in active mode regardless of participants' gender while no activation is observed on DLPFC in passive mode. These results are highly consistent with those concluded in Rao et al., 2008 [82].

Closer comparisons are made between this study and the one reported by Cazzell et al. in fNIRS research [16]. Cazzell et al. have recently compared gender differences in brain activation maps and hemodynamic responses in HbO when subjects responded to BART. It is noteworthy that Cazzell et al. focused on the brain responses only when subjects observed or reacted to the outcomes of BART (i.e., seeing either "you win" or "you lose") regardless of the responses when subjects performed the BART paradigm (balloon inflation). The comparisons herein are made only for the outcome stimuli. In their study, although brain activation maps are determined by FWHM of HbO spatial patterns, the study concluded strong bilateral brain activations on DLPFC in active mode which is consistent with our results shown in Figure 4-4. In passive mode, we

observed no activation on DLPFC in this study (see Figure 4-4), whereas slight brain activations are exhibited on DLPFC in Cazzell et al. although they are relatively weaker compared to those in active mode. For the comparison of reactions to two outcomes between genders, the study reported by Cazzell et al. concluded strong bilateral brain activations on DLPFC in both “win” and “lose” cases for female subjects and in win “case” for male. This conclusion is relatively consistent with our findings given here, as seen in Figure 4-6 (a) and (b). For male subjects, while the results by Cazzell et al. demonstrated strong bilateral changes on DLPFC in the “win” case, the changes exhibited a strong decrease (or deactivation) in ΔHbO on the right DLPFC (see Fig. 8 in [16]). However, the brain activation/deactivation maps obtained in the “lose” case for male subjects in this study displayed somewhat different patterns or distributions: the FWHM-derived results from Cazzell et al. revealed more diffuse deactivation patterns which are distributed closer to DLPFC (BA 46) bilaterally, while GLM-derived results given in this study exhibited more unilateral activation on the left frontal region, located near both BA 9 and 46 (see Figure 4-6d).

The agreement and disagreement between the brain activation maps derived by two types of data analysis methods need to be understood in order to select a more accurate approach for improved DOT in brain imaging. The disagreement could result from the following factors: (1) Image reconstruction process in this study is based on human brain atlas-guided 3D DOT after depth-compensation and voxel-wise GLM analysis are performed, while the earlier study by Cazzell et al. utilized non-atlas-guided, 2D-DOT with no depth compensation or statistical parametric analysis. In Cazzell et al's study, 2D-DOT images are thresholded by FWHM of reconstructed HbO amplitudes and approximately projected onto the anatomical human brain template according to the approach given by Homan et al [111]. Distinct differences in distribution of brain

activation patterns are highly likely to exist because of different reconstruction algorithms, co-registration methods, and the anatomical brain template used between the two methodologies. (2) Due to the difference in image processing algorithms, the two methods rest on two hidden hypotheses: the current method given in this paper utilizes the conventional GLM model commonly used in fMRI, assuming that voxel-wise HbO signals can be modeled well by convolving the stimulation function with the HRF. Also, in this study, we utilized a mixed block/event-related design to model the two stimulation phases that are directly associated with BART [95]. This mixed design in principle allowed us to separate the brain responses between the decision-making/performance phase and the reaction phase. On the other hand, the FWHM-based image processing method by Cazzell et al. to determine the activation maps relied on the level of reconstructed maximum activation, so the activation patterns are more affected by the level of maximum activation. Furthermore, the 5-sec post-stimulation window used for 2D-DOT reconstruction by Cazzell et al. indeed included the brain responses to the performance phase (see Figure4-1a) on top of the responses to the reaction phase. Thus, it is not surprising that the reconstructed brain activation maps derived by two types of data analysis methods are somewhat different. It is reasonable to state that the activation maps studied by Cazzell et al. reflected brain responses to convolved stimulation tasks, while the activation maps shown in this paper present brain responses to two separate or de-convoluted stimulation tasks (i.e., performance phase and reaction phase) .

4.5.2 Atlas-DOT in Brain Research

In this study, we utilized the head atlas to anatomically guide the 3D-DOT reconstruction. Anatomically-guided DOT reconstruction has been used in brain research within the fNIRS community to overcome the major drawback of DOT, namely, lack of

structural information. Two major approaches, atlas anatomical-guided [112] and subject-specific anatomical-guided 3D-DOT [43], [108], have been intensely presented in the field recently. While subject-specific anatomical-guided 3D-DOT demonstrated accurate localization of brain activation compared with fMRI [114], the expected localization errors when using atlas-DOT could result from: (1) differences between subject specific anatomy and atlas anatomy, and (2) registration errors between subject space and atlas space, including the variations due to measurement of optode locations in subject space by a 3D digitizer. Studies on the comparisons between these two approaches have been presented by Custo et al. [112] and Cooper et al. [114]. Custo et al. compared the reconstruction results from the two approaches using three subjects. The spatial and numerical (i.e., overlapping between two reconstructions up to 93%; Dice's coefficient up to 0.86 [112]) results concluded that accurate cortical activation locations determined by fNIRS can be obtained using an atlas-based head model. A further supporting report by Copper et al. also concluded that atlas-guided 3D-DOT could provide reasonably accurate localization of brain activation based on the computational simulation results. Based on these conclusions and our study shown in this paper, we highly recommend utilizing atlas-guided 3D-DOT as a useful neuroimaging tool when investigating brain functions and stimulated activities.

4.5.3 Limitations and future work

While we have demonstrated that atlas-guided voxel-wise GLM-based analysis allows us to simultaneously model the mixed task-evoked brain activations with a better statistical power, this proposed methodology is still limited by: (1) the nature of light scattering in tissues, which results in reduction of spatial resolution and depth accuracy, and (2) mixed signals between the brain activations and artifacts from the superficial layers, i.e., scalp and skull. While the latter aspects have been studied by using

superficial signal regression [113] and adaptive filtering [15] to isolate the brain signals, the GLM-based analysis has the capability to resolve this problem [110]. However, for all of the methods mentioned above, it still remains difficult if the fluctuations of brain activations and superficial artifacts follow the same or similar temporal patterns/frequency. Therefore, a combination of GLM-based analysis and adaptive filtering/linear regression with a high-density optode array is possibly an optimal approach in order to improve depth and localization accuracies of DOT for functional brain imaging.

It is also well known that utilization of more source-detector (S-D) pairs in a high-density optode array for 3D-DOT reconstruction will benefit the quality of reconstructed images. In this study, we selected only the first-nearest S-D pairs for image reconstruction because the noise levels from the second-nearest S-D pairs (separated by 4.8 cm) are too high. For future studies, we will modify the current probe geometry and form a high-density optode array so that the second and possibly third nearest S-D measurements can be performed for improved 3D-DOT reconstruction.

The purpose of using a band pass filter from 0.03 to 0.2 Hz on raw data is to remove (1) high-frequency physiological interference due to respiration (>0.2 Hz) and cardiac (>1 Hz) signals and (2) low-frequency (<0.03 Hz) system drift. Utilization of a band-pass filter has been a common image pre-processing procedure for reconstructing DOT by numerous research groups [39], [41], [92], [108], [110]. It might be true that when GLM is applied by deconvolving HbO (and HbR) with a given HRF, a band-pass filter may not be necessary since the temporal HbO/HbR profiles are fitted in a least squares sense with the model. However, uses of a band-pass filter will help reduce any possibly large noises, particularly for HbO or HbR signals at the individual subject level. To consider an optimal action, it may be beneficial to select a lower high-pass cutoff

frequency (such as 0.01 Hz) for future studies in order to avoid any possible distortion of time course induced by high-pass filtering.

It is expected that a fixed HRF may not be applicable to all functional changes occurring in the brain. However, in order to use variable HRFs for different functional changes in different regions of the brain, further research is needed to define specific HRFs for respective tasks or functions. Finding activation-dependent HRFs is beyond the scope of this study and is left for future studies.

4.6 Summary

The main focus of this Chapter is to demonstrate the feasibility of integrating three DOT data/image process techniques in order to better define and identify the brain activations for fNIRS-based functional brain imaging. The three techniques are (1) atlas-DOT, (2) depth compensated algorithm, and (3) voxel-wise GLM analysis, which together allowed us to image hemodynamic changes induced by a specific risk decision-taking task, BART, with improved 3D visualization and depth localization. The results shown in this study demonstrated that human brain atlas-DOT provided better visualization and helped greatly to localize brain activation regions. Voxel-wise GLM analysis is developed and utilized complementarily with 3D-DOT for functional brain imaging, leading to good agreement with an fMRI study. Such integration of GLM analysis with volumetric DOT also provided excellent statistical analysis reliability and improved spatial localization, as well as allowed us to separate two convolved brain activities in response to performance and reaction stimulations in the BART paradigm. In addition, the current study provides convincing evidence that atlas-guided volumetric DOT with voxel-wise GLM analysis has strong potential for use in studies of cognitive-related brain activity. Most importantly, this integration methodology can be extended to reconstruct and analyze fNIRS or DOT images induced by different brain stimulation protocols. It is evident that reconstructed 3D

DOT images seen on a brain atlas template can be easily compared and confirmed with published literatures in fMRI studies, if further validation is desired.

Chapter 5

Assessment of Age and Gender Effect on Brain Activation under Risk Decision-making

5.1 Introduction

5.1.1 Background and significance

Studies of age and gender effects on brain function are recent hot topics in the field of neuroscience. Earlier studies have indicated that development in functional brain regions varies by age and gender [16], [30], [114]–[120]. For example, studies have shown that the motor and sensory cortices are the earliest regions to mature than other higher-order brain areas, such as the prefrontal cortex [115], [116]. Meanwhile, the decline of functional brain regions is not linear through the life span. Brain recession appears first in the prefrontal region, then gray matter declines gradually, spreading to the whole brain [9]. In addition, development of brain regions has shown to differ between genders, where reductions in cerebral gray matters are more obvious in males in youth and adulthood [121], but opposite observations are found in females in the old ages [122].

Neuroimaging methods, such as functional magnetic resonance imaging (fMRI), have proven to be useful in assessment of age- and gender- dependent cognitive functions [3]–[5], [7], [8], [13], [123]–[128]. However, due to the limiting factors of fMRI for older adults, restrictive body confinement and contraindications based on certain health conditions, it is necessary to explore other neuroimaging modalities, such as functional near infrared spectroscopy (fNIRS). To address this issue, I have applied the GLM-based atlas-DOT method (details are shown in Chapter 2 and 4) to explore age- and gender-dependent prefrontal activations in this Chapter. A total of 100 participants among two age groups (25-44 years and 60-95 years) have completed the Balloon Analog Risk Task (BART), a risk decision-making paradigm [77].

5.1.2 Age- and gender-effect on neurocognitive functions

Age effects on neurocognitive performances are well documented. It is well known that declines in high-order brain functions, such as memory, learning, information processing, and decision making, are progressively related to age [9]. Recent studies indicate that the PFC is the most affected region by the age-related decline compared to other parts of the brain, such as the temporal lobe, hippocampus and striatum [1], [2]. Theories of neurocognitive aging suggests a compensation mechanism in older adults; the brain could recruit additional neural cells in the neighboring functional regions to maintain the same work load as that in young adults [3]–[8]. More specifically, a review study indicates that older adults engaged more expansive areas of the PFC than young adults across a variety of externally-driven cognitive tasks [4]. Researchers of fMRI studies under gambling simulations also indicate that older adults exhibit increased neural activations in either the superior PFC, left orbitofrontal cortex ([OFC]; [5]) and bilateral ventromedial prefrontal cortex ([vmPFC]; [6]). Similar studies also report that memory-related tasks are associated with increased brain activations in the inferior frontal gyrus ([IFG]; [7]) and the bilateral dorsolateral prefrontal cortex ([DLPFC]; [8]).

Functional brain imaging studies report significant gender differences under risk decision-making or reward-related decision-making processes [11]–[13], [123], [129]. It is also suggested that emotional regulation, highly related to OFC (or equally vmPFC) and DLPFC, dominated gender-dependent neurocognitive differences in risk decision making [11]–[13]. Specifically, fMRI reviews on the Iowa Gambling Task (IGT) indicate: (1) females highly activate their OFC regions in the face of lose outcomes, while males exhibit less OFC responses than females; and (2) males have increased DLPFC activations when choosing long-term large rewards and controlling both positive and negative emotions, but females have activated the DLPFC regions only when controlling

positive emotions [11], [130]. In addition, an fMRI study (n = 22, 10 females) on gender-related differences in neural activity during risk taking reports an increased neural activity in the OFC for females during risk taking [12]. Moreover, an fMRI study on cognitive reappraisal reports increased brain activations in females in the prefrontal regions and greater decreased activations in the amygdala, associated with cognitive regulation of emotion [13].

5.1.3 fNIRS and BART

Studies of neurocognitive functions using fNIRS have increased in recent years [16], [39], [131] Functional NIRS allows non-invasive imaging of human brain functions by injecting near infrared (NIR) light into the human head and taking optical measurements on the human scalp. Functional NIRS offers lower imaging costs, portability and easier access for larger subject populations than fMRI. In addition, fNIRS has consistently correlated its findings with fMRI in mapping the cortical activations [43]. In this Chapter, I have applied atlas-DOT, based on multi-channel fNIRS to map brain activations in response to BART [105]. The atlas-DOT provides three-dimensional (3D) tomographic imaging by using an atlas-based finite-element model (FEM). Moreover, with implementation of a depth compensation algorithm (DCA) and general linear model (GLM), the atlas-DOT has significantly improved lateral resolution and localization accuracy of reconstructed images[47], [105], [110].

The assessment protocol in this study is the Balloon Analog Risk task (BART), a risk decision-making task. BART has been widely used in psychological studies as a reliable measure to generate “real-world” risk-taking [77], [79]–[81]. During BART, increasing the size of the balloons through inflations is associated with higher monetary rewards stored in a “virtual” bank. Meanwhile, increased inflations can lead to increased money or a balloon explosion. When a balloon explodes, money accrued for that balloon

is lost. From the original BART, modified computational versions of BART protocol have been implemented into neuroimaging studies in recent years. Both fMRI and fNIRS studies, in applying the BART paradigm to young adult groups (25 to 45 years of age), demonstrate highly-evoked DLPFC activations [16], [82]. Here, a similar fNIRS BART paradigm, as presented in [16], is utilized as the stimulation protocol in young and older adults; age- and gender-dependent responses to risk decision making and their outcomes are investigated.

5.1.4, Study aims and purpose

The aim of this Chapter is to investigate age- and gender- dependent neural correlates under risk decision making using atlas-DOT. The purposes are to identify: (1) age differences in prefrontal activations between young and older adults, (2) gender differences in prefrontal activations within each age group, (3) correlations between behavior and prefrontal activations in each age group, and (4) atlas-DOT as an efficient tool in mapping neurocognitive activations in young and older adults.

5.2 Material and method

5.2.1 Study design

A mixed block/event-related general linear model (GLM) study design was used to investigate the activations of PFC regions during a two-phase BART stimulation. In the first decision-making phase, participants actively inflated balloons (Figure 5-1(a), left side). Every participant utilized a specific decision-making period per balloon; time varied from 3 to 10 seconds. In the second phase, participants faced either a win or lose outcome with the sudden appearance (<1s) of the phrases “You Win!!” or “You Lose!!” in the center of the monitor (Figure5-1(a), right side). After the BART tasks were completed, each participant received a \$10 gift card. For specific BART protocol, please see Cazzell et al., (2012).

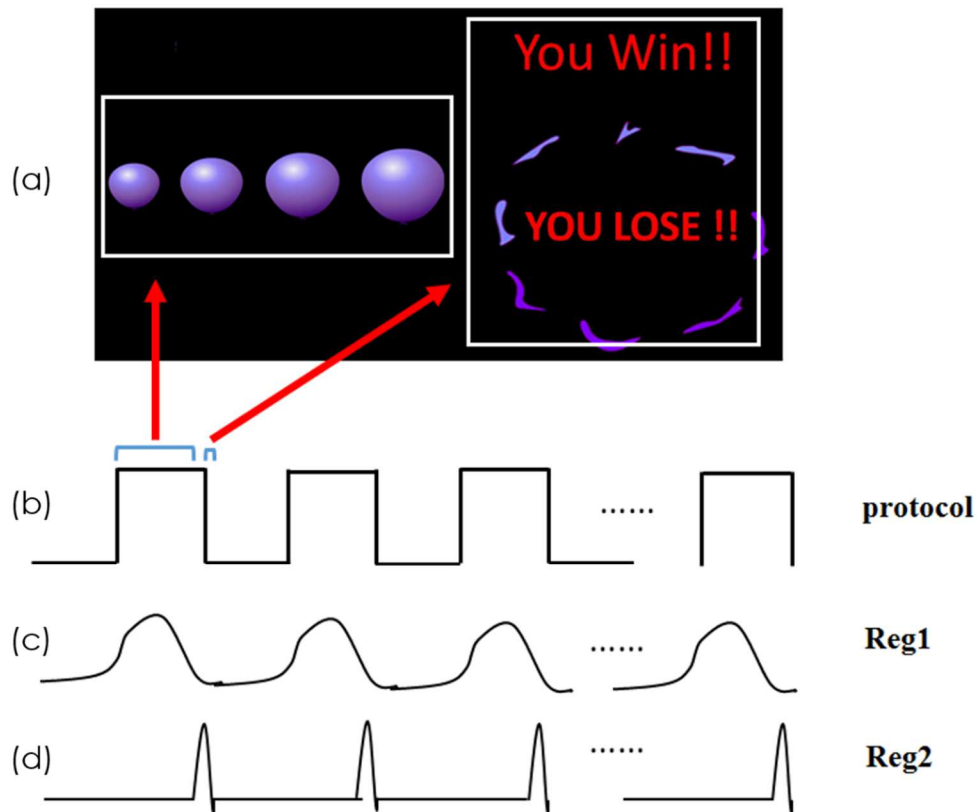


Figure 5-1 Experimental protocol and regressor design. (a) The BART protocol for decision-making phase (left) and outcome phase (right); (b) block design of the BART protocol; (c) illustration of regressor for the decision-making phase; (d) illustration of regressor for outcome phase.

5.2.2 Participants

To achieve adequate study power, a convenience sample ($N = 100$) was recruited in this Chapter; forty healthy young adults (23 males and 17 females) and sixty cognitively-healthy older adults (22 males and 38 females) participated. No participants reported any known musculoskeletal, neurological, visual, or cardio-respiratory dysfunctions. All participations were right-handed with normal or corrected-to-normal

vision. All participants completed a demographic survey on age, gender and highest level of education before conducting the BART measurement. Pre-test automatic blood pressures (BP) were also measured using a Dinamapp™ BP machine. Elevated blood pressure, affecting cerebral perfusion, could confound brain hemodynamic activity during the BART phases. The age ranges were mid-twenties to mid-forties for young adults, and >65 years of age for older adults. The age range for young adults were chosen to assure the approximated ages for PFC maturation [132] and the age range for older adults were chosen due to the documented rapid decline of gray matter density between 60 to 70 years [133]. The study was approved by the University of Texas at Arlington Institutional Review Board (IRB).

5.2.3 Experimental set up

Changes of brain hemodynamic responses were measured by a multi-channel functional near-infrared spectroscopy (Cephalogics®, Ishington Univ., USA). Source fiber included 750nm and 850nm laser emitting diodes (LEDs). The detectors were avalanche photodiodes (APDs). Subjects from two age groups were measured by using two different optical probe geometries. Older adults utilized 16 sources (red bobble) 16 detectors (blue bobble) probe [Figure 5-2(a)] with a total of 72 source-detector channels. Young adults used a 12 sources 16 detectors probe [Figure 5-2 (b)] with 40 pairs of source-detectors. More specifically, the source-detector separation for the probe used was 3 cm in older adult measurement and 3.25 cm in young adult measurement. These two probes covered similar prefrontal regions of the brain (Brodmann area 9, 10, 11), but to ensure that there were no significant variations in optical sensitivity, quantitative analyses were performed to test the similarity of those two sensitivity matrixes. The first parameter compared was the overlapped regions $R_{overlap}$ by [63]:

$$R_{overlap} = 2 \times C_{overlap} / (C_1 + C_2)$$

Where $C1$ was the number of pixels in the sensitivity matrix for young adults, and $C2$ was the number of pixels in the sensitivity matrix for older adults. Coverlap was the overlapped number of pixels between two sensitivity matrixes.

The second parameter was the mean sensitivity amplitudes over the whole sensitivity matrix, for young (S_{yi} , $i = 1, 2, \dots, 40$) and older adults (S_{oj} , $j = 1, 2, \dots, 60$). A paired t test with unequal variance was performed between S_{yi} and S_{oj} .

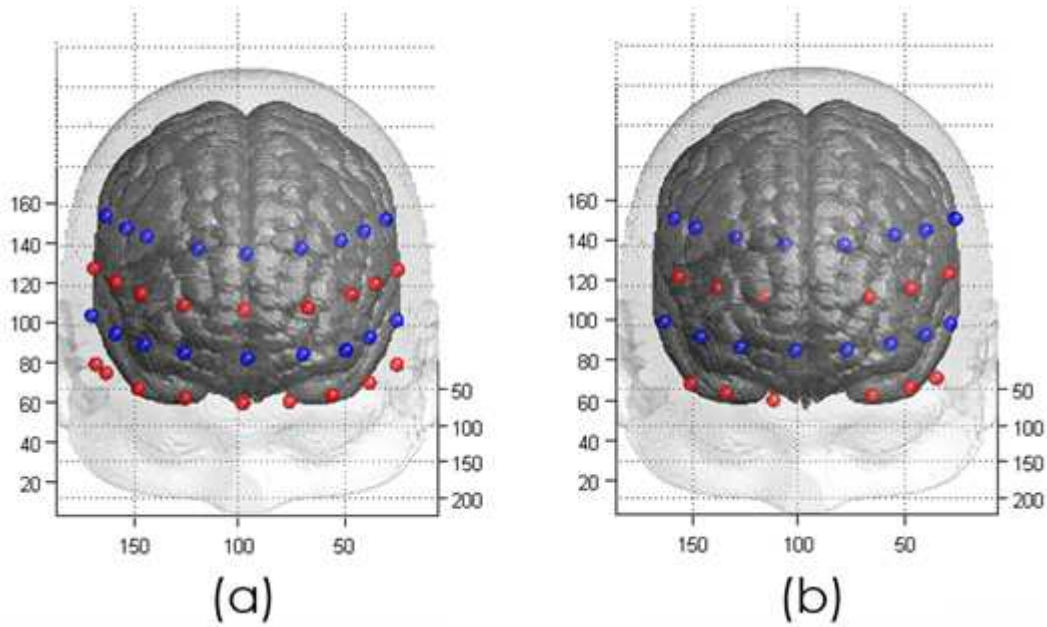


Figure 5-2 Optode probes for (a) older adults and (b) young adults. Images were plotted as the outcome of 3D co-registration.

The sensitivity matrices for two geometries were shown in Figure 5-3(a) and 3(b). The overlapped regions between two geometries were $R_{overlap} = 0.91$. The second comparison, which tested the averaged amplitude of sensitivity matrix between the young and older groups, showed no significant difference ($p = 0.21$). These results indicated that differences between the two sensitivity matrices were small and could be ignored.

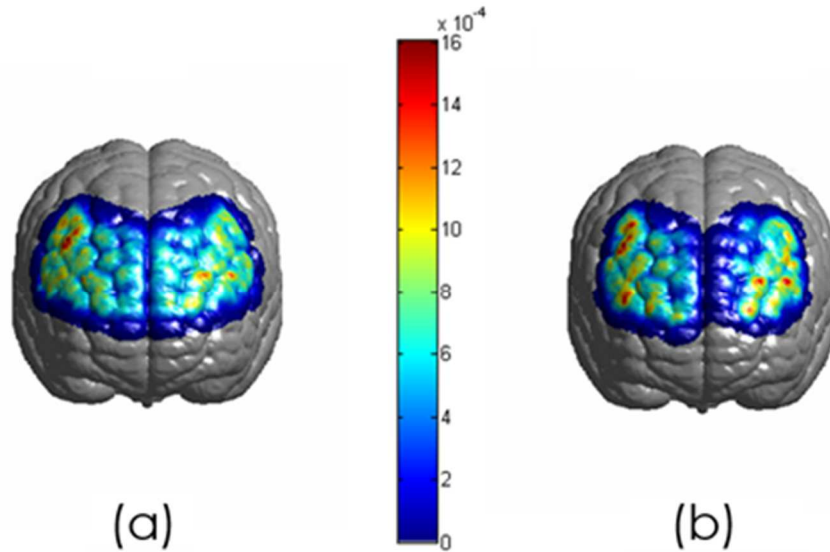


Figure 5-3 Optical sensitivity matrices for (a) older adults and (b) young adults.

5.2.4 Data processing

Three major steps, namely, data preprocessing, atlas-guided image reconstruction, and general linear model (GLM), were included in the data analyses. First, preprocessing of the fNIRS raw data for all participants was applied. Specifically, a band-pass filter from 0.03 Hz to 0.2 Hz was applied to all raw data in order to eliminate the high-frequency physiological interference from respiration ($>0.2\text{Hz}$) and cardiac pulsation ($>1\text{ Hz}$) as well as low-frequency ($<0.03\text{ Hz}$) system drift [42], [63], [134]. Second, the atlas-guided DOT image reconstruction was applied to obtain functional brain images. Specifically, a 171,262 pixel four-layered template was pre-generated and the forward calculation was performed. The sensitivity matrix J (also named Jacobian matrix) was computed on the atlas template under the two optode geometries using a MATLAB package NIRFAST [52]. Followed by image reconstruction, Tikhonov regularization was implemented using a depth compensation algorithm ([DCA]; [47], [54]). Relative changes in oxygenated hemoglobin (ΔHbO), deoxygenated hemoglobin (ΔHHb),

and total hemoglobin concentrations (ΔHbT) were determined by two wavelengths (750nm and 850nm) image reconstruction, based on spectral decomposition of extinction coefficients for both wavelengths [39]. More details of atlas-DOT method were presented in [105]. Third, GLM analysis was applied to the voxel-wised hemodynamic data obtained from the previous step. Only the ΔHbO sequence was used for GLM analysis since the ΔHHb levels were of very low magnitude to the BART stimulation across both age groups [16]. Two regressors were designed based on the experimental protocol. Figure 5-1 displays the experimental protocol and the regressor design. For each block, the first three to ten seconds are considered the decision-making phase and is labeled as “Reg1”, shown in Figure 5-1(c). Figure 5-1(d) describing the outcome phase is labeled “Reg2” — a rapid response phase.

A 3D map corresponding to estimated response amplitudes was generated by applying temporal general linear model (GLM) fitting [105]. The conventional ordinary least squares (OLS) estimation was applied to the voxel-wised ΔHbO data [97]. Specific cortical regions, activated by two separate stimulations (decision-making or outcome phase), were then identified by the t-maps.

One issue that could lead to bias or overestimation of functional data was the temporally correlated residuals of GLM due to un-modeled physiology or structural noise such as intrinsic brain activities, heart beats, or respirations [91], [99], [101], [103]. Temporal correlated residuals could also vary the degrees of freedom that affect the accuracy of conclusions in t-tests [102], [105]. To deal with this issue, an autocorrelation matrix was applied to correct the OLS estimation [99]. Then, a false discovery rate (FDR) was applied to obtain corrected degrees of freedom [106]. Moreover, $p < 0.05$ (FDR corrected) was chosen as a threshold to obtain the region of interest (ROI). Group-based t-maps in both decision-making and outcome phases were obtained through random

effect analysis for both gender and age groups. Results were plotted and arranged by male/female in the gender-effect analysis, and with young/older adult pairings in the age-effect comparisons. ROI volumes (in pixel number) and mean amplitudes (μM) within ROI were quantified for further statistical analysis.

5.2.5 Statistical analysis

Statistical analyses were performed for behavioral and hemodynamic responses in age and gender groups. The software used in the analysis was Statistical Analysis Software (SAS)®9.2 (SAS Institute Inc., Cary, NC). Thus, the gender effect in young and older adult groups were analyzed separately.

i: Statistical analysis for behavioral data

Described previously in [16], average adjusted pumps (AAP), measuring the adjusted average number of pumps on unexploded balloons, were quantified as the behavioral risk score. Age differences on behavioral data were quantified using one-way Analysis of Variance (ANOVA). Then, multiple comparisons were performed under confidence level of 95%. Gender differences on behavioral measures were analyzed within young and older adult groups separately following the same strategy.

ii: Statistical analysis for brain activity data

Brain activations based on changes in ROI-averaged ΔHbO amplitude (β) were calculated after GLM analysis β by averaging the amplitudes of significantly-activated pixels within each participant's activated cortical regions. Group-level analyses were performed in both decision-making and outcome phases. For the decision-making phase, one-way ANOVA was performed to examine significant differences in ΔHbO (or β) amplitude. The above analysis was repeated on the outcome phase data, with amplitudes, corresponding to “win” and “lose” outcomes, quantified separately.

iii: Statistical analysis for correlation

In order to investigate possible relationships between behavioral performances and brain activations during risk decision making, Pearson correlation coefficients (r) were computed for age and gender groups in the “win” and “lose” outcome phases. A positive correlation coefficient between brain activation and risk scores represents “risk-taking” performances, while a negative correlation represents “risk-averse” performances. The criterion for significance was set at $p < 0.05$.

5.3 Results

5.3.1 Participants

Forty young adults (17 males and 23 females), mean age of 28.8 ± 5.4 years participated in this study. Seventy percent of young adult had college degrees; systolic blood pressure averaged 118.8 ± 65.7 mmHg. Sixty older adults (22 males and 38 females), mean age of 76.2 ± 6.5 years completed this study. Forty-six percent of older adults were college educated; mean systolic blood pressure was 143.26 ± 71.76 mmHg. To ensure that all older adult participants were cognitively healthy, the Montreal Cognitive Assessment (MoCA) was administered by research personnel. All participants needed to score 26 points or higher to document cognitive health [135]; all sixty participants met this eligibility requirement with an average score of 27.9 ± 1.2 .

5.3.2 Brain maps for two phases

Statistical parametric maps (t-maps) are computed for all participants on both decision-making and outcome phases. Oxygenated hemodynamic changes (ΔHbO) are used to compute GLM fitting with the two regressors, shown in Figure 5-1(c) and 1(d). A critical value of $p < 0.05$ (FDR corrected) is used in the GLM process. As shown in Figure 5-4(a), BART paradigms on Phase 1 (decision making) robustly evoked brain hemodynamic changes in the frontal and prefrontal regions. Age-effect analysis revealed diffuse bilateral DLPFC and rostrolateral prefrontal cortex (RLPFC) activations in older

adults. More focused bilateral DLPFC activations are observed in young adults. From the three-plane views (coronal, sagittal and axial), a significant frontal lobe activation is clearly seen in both age groups. Brodmann area 9 (DLPFC and RLPFC) is the major activated region.

Brain images for outcome phase (Phase 2) are shown in Figure 5-4(b), where cortical, coronal, sagittal, and axial views are presented in four cases (young-win, older-win, young-lose, and older-lose) on the same color scale. For the older adult group, a minor cortical activation is observed in the win case, while robust bilateral activations are displayed in the prefrontal regions (DLPFC and RLPFC) in the lose case. For the young adult group, strong bilateral brain activations in the DLPFC region are observed in win and lose cases.

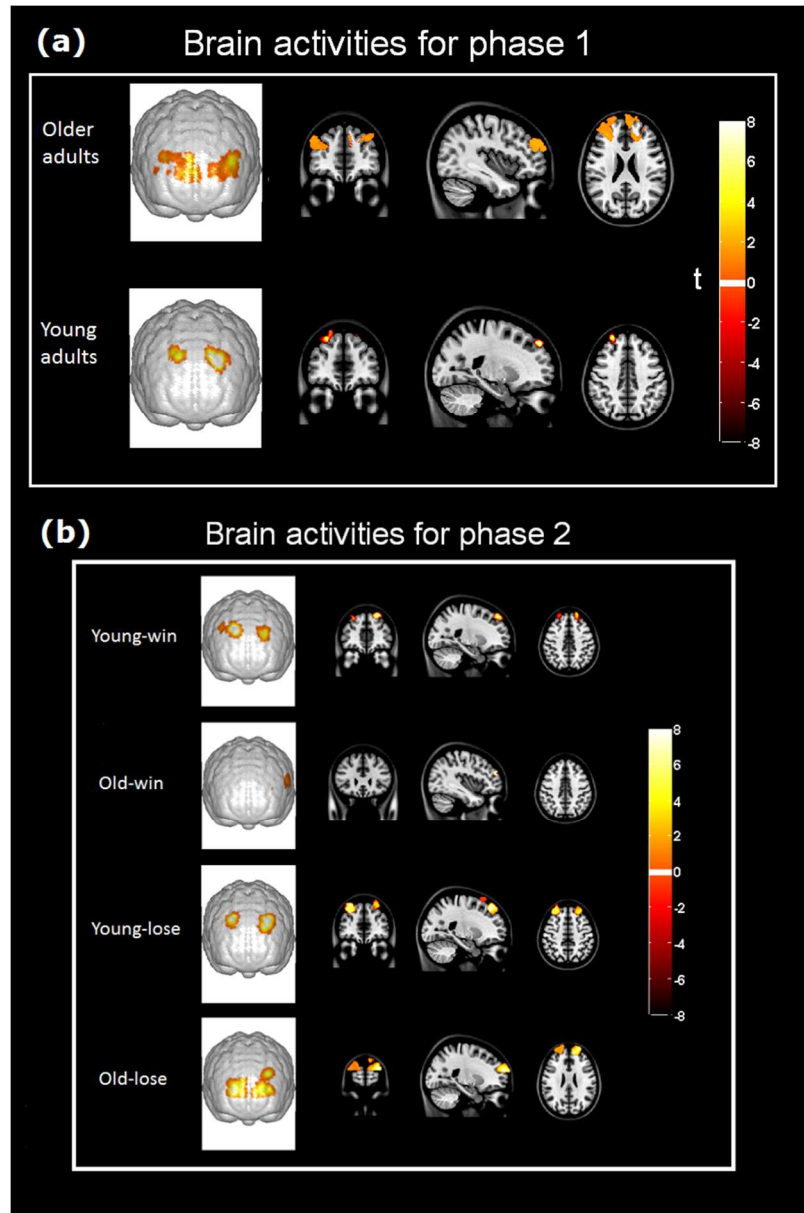


Figure 5-4 (a) Group-level brain activations (t -maps) for phase 1; images are displayed by groups of older adults and young adults. (b) Group-level brain activations for phase 2; from top to bottom showed young adult-win, older adult-win, young adult-lose, and older adult-lose, respectively. Images are obtained from the voxel-wise t -map threshold at $p < 0.05$ (FDR corrected).

Further analyses for assessing brain activation regions are performed in Phase 2 by considering both gender- and age-effects. ROI volumes are quantified by counting the number of pixels within ROIs for both males and females in young and older adult groups. Figure 5-5 revealed the ROI volumes for young-male, young-female, older-male, and older-female groups in both win and lose outcomes. In particular, young male adults (Figure 5-5(a), red) revealed a bilateral ROI in DLPFC win cases, and right side DLPFC ROI in lose cases. Young female adults (Figure 5- 5(a), yellow) revealed a right side DLPFC ROI in win cases and a bilateral DLPFC ROI in lose cases. In addition, both older male adults (Figure 5-5(b), red) and older female adults (Figure 5-5(b), yellow) had small left side ROIs in middle frontal gyrus (MFG) in win cases, but strong bilateral ROIs in both DLPFC and RLPFC in lose cases are observed. The quantitative values for the numbers of activated pixels are summarized in Table 5-1. Specifically, gender comparisons by two sample t-tests revealed that the ROI volumes in young male adults are significantly larger than young females in win cases ($p = 0.03$), and are significantly smaller in lose cases ($p < 0.01$). No gender differences of ROI volumes in older adults are noted under either win outcomes ($p = 0.19$) or lose outcomes ($p = 0.49$). In general, quantitative analysis revealed the existence of gender differences in brain activation patterns in both age groups.

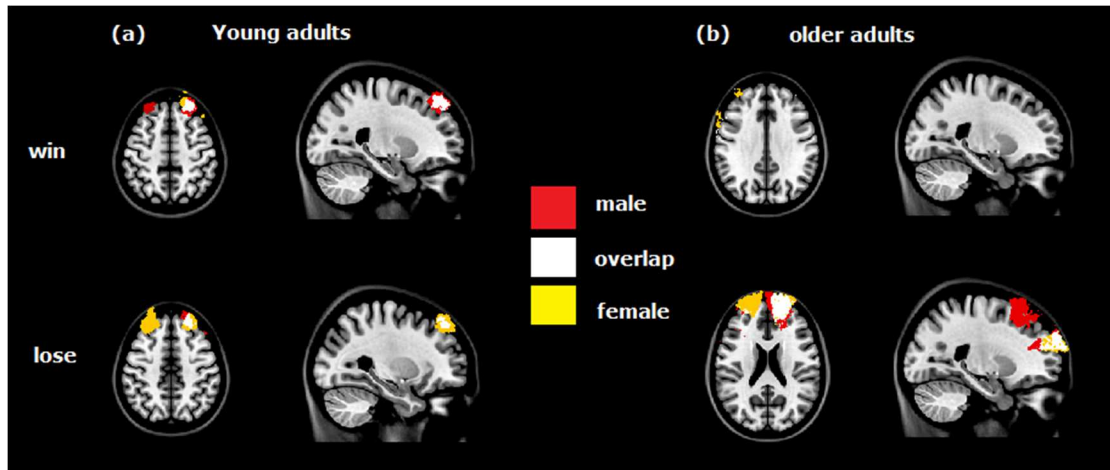


Figure 5-5 Brain activation regions for males and females in young adult (a) and older adult (b) groups. Brain activation regions for male, female, and overlaps are presented in red, yellow, and white color, respectively. Upper images showed the brain activation regions in win case for young adults (left) and older adults (right). Lower images showed the brain activation regions in lose case for young adults (left) and older adults (right).

Table 5-1 Brain activation regions (ROI volume) in phase 2

		Male			Female			
		Region	Side	Volume	Region	Side	Volume	<i>p</i>
Young	Win	DLPFC	BL	987.48	DLPFC	R	497.31	0.03
	Lose	DLPFC	R	206.17	DLPFC	BL	881.81	<0.01
Older	Win	MFG	L	120.76	MFG	L	121.03	0.49
	Lose	DLPFC+RLPFC	BL	3103.19	DLPFC+RLPFC	BL	2303.5	0.19

BL = bilateral; R = right side; L = left side

5.3.3 Statistical analysis for age effect

5.3.3.1 Behavioral measures

All behavioral data are normally distributed. One-way ANOVA analysis of average adjusted pumps revealed significant differences ($F = 9.49$; $p < 0.001$) between young-win, old-win, young-lose, old-lose groups. Results from pairwise comparisons

showed significant age differences in both the win case ($t = 4.41$; $p < 0.001$) and lose case ($t = 2.77$; $p = 0.012$) [Figure 5-6(a)]. Specifically, it is observed that the number of average adjusted pumps in young adults (6.0 ± 1.2) are significantly higher than those in older adults (5.0 ± 0.9) in the win case. The same pattern is observed among young adults (6.0 ± 1.5) and older adults (5.3 ± 0.9) in the lose case.

5.3.3.2 Brain hemodynamic responses

Quantified statistical analysis for brain activations is performed by investigating mean amplitudes within ROIs. Means and standard deviations of brain activations in Phase 1 are quantified for age effect (older adult = $0.64 \pm 0.24 \mu\text{M}$; young adult = $1.07 \pm 0.37 \mu\text{M}$). Pairwise analysis with unequal variance demonstrated a significant age difference in the amplitude comparison (young>older; $t = 6.92$; $df = 98$; $p < 0.001$; 95% CI = -0.55, -0.30). One-way ANOVA analyses on Phase 2 outcomes indicated significant differences in hemodynamic amplitudes between old-win, old-lose, young-win, and young-lose groups ($F = 23.94$; $p < 0.001$). Pairwise comparisons [Figure 5-6 (b)] showed significant larger ROI amplitudes in young adults than older adults in the win case ($t = 7.51$; $p < 0.001$; 95%CI = 0.37, 0.68). No significant age difference is found in the lose case ($t = 0.97$; $p = 0.56$; 95%CI = -0.22, 0.09).

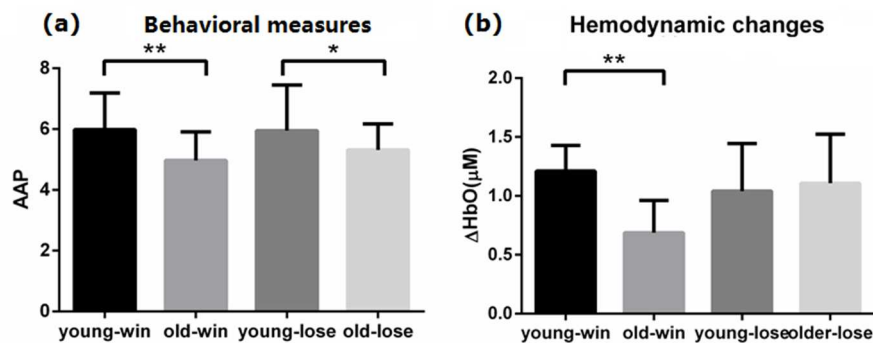


Figure 5-6 (a) Behavioral data for the age-effect analysis; (b) brain activity data for age-effect analysis. Columns showed the bar plot of mean and standard deviation (one-sided)

for young-win, old-win, young-lose, and older-lose groups, respectively. **: $p < 0.001$ * $p < 0.05$

Descriptive statistics of behavioral measures and brain activity data are displayed in Table 5-2. Mean, standard deviation and 95% confidence interval for young adults and older adults in Phase 2 are presented.

Table 5-2 Descriptive statistics of behavioral measures (AAP) and hemodynamic responses [ΔHbO (μM)] in young and older adults

		win		lose	
		Mean(SD)	95%CI	Mean(SD)	95%CI
AAP	Young	5.99(1.21)	5.60,6.37	5.95(1.50)	5.47,6.43
	Older	4.97(0.94)	4.72,5.22	5.31(0.86)	5.09,5.54
ΔHbO	Young	1.21(0.22)	1.14,1.28	1.04(0.40)	0.91,1.17
	Older	0.69(0.28)	0.62,1.17	1.11(0.42)	1.00,1.22

5.3.4 Statistical analysis for gender effect

5.3.4.1 Gender differences in young adults

For behavioral data, one-way ANOVA analysis revealed significant differences among young adults ($F = 3.19$; $p = 0.03$) between male-win, female-win, male-lose, female-lose groups. Results of pairwise comparisons showed significantly higher AAP in males in lose cases ($t = 2.90$; $p = 0.01$) but no significant gender differences in win cases ($t = 1.07$; $p = 0.49$) [Figure 5-7(a)].

Gender differences in brain activities are quantified following the same strategy as in age-effect analysis. One-way ANOVA analyses showed significant differences between male-win, female-win, male-lose, and female-lose groups ($F = 11.33$; $p < 0.001$). Pairwise comparison [Figure 5-7(b)] showed significant larger ROI amplitudes in males in

win case ($t = 4.16$; $p < 0.001$; $95\%CI = 0.30, 1.02$) but a significant smaller ROI amplitudes for males in lose cases ($t = 2.88$; $p = 0.01$; $95\%CI = -0.82, -0.09$).

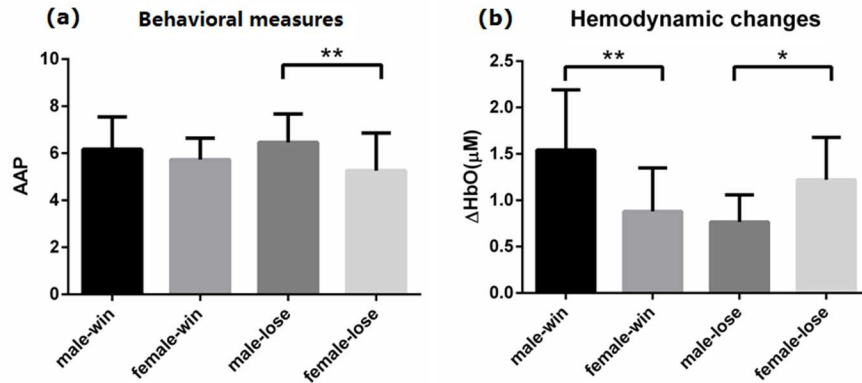


Figure 5-7 Gender comparisons in young adults. (a) Bar plot for means and standard deviations of behavioral data; (b) bar plot for means and standard deviations of hemodynamic data. Columns showed the mean and standard deviation (one-sided) for “young male win”, “young female win”, “young male lose,” and “young female lose” groups, respectively. **: $p < 0.001$ * $p < 0.05$

5.3.4.2 Gender differences in older adults

Behavioral data showed no significant gender differences in older adults in the win case ($t = 2.19$; $p = 0.06$) and in the lose case ($t = 0.09$; $p = 0.99$) [Figure 5-8(a)]. One-way ANOVA analyses showed significant differences between older adult male-win, female-win, male-lose and female-lose groups ($F = 21.89$; $p < 0.001$). But these differences only existed in the win/lose cross comparison (e.g., male-win vs. male-lose). There are no significant differences between older males and older females in the win case ($t = 1.24$; $p = 0.39$; $95\%CI = -0.09, 0.29$) and the lose case ($t = 0.06$; $p = 0.99$; $95\%CI = -0.18, 0.19$) [Figure 5-8(b)].

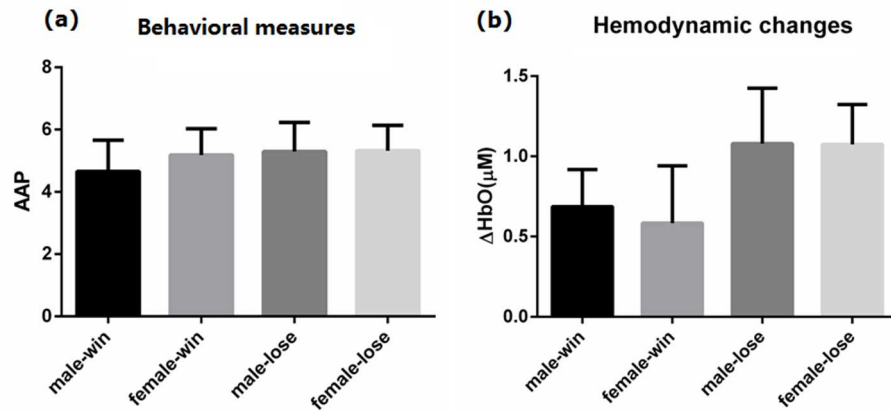


Figure 5-8 Gender comparisons in older adults. (a) Bar plot for means and standard deviations of behavioral data; (b) bar plot for means and standard deviations of hemodynamic data. Columns showed the bar plot of mean and standard deviation for “older male win”, “older female win”, “older male lose” and “older female lose” groups, respectively.

Descriptive statistics of behavioral and hemodynamic responses for gender differences in young adults and older adults are displayed in Table 5-3.

Table 5-3 Descriptive statistics of behavioral measures (AAP) and hemodynamic responses [ΔHbO (μM)] in males and females

		male				female			
		win		lose		win		lose	
		Mean(SD)	95%CI	Mean(SD)	95%CI	Mean(SD)	95%CI	Mean(SD)	95%CI
AAP	Young	6.2(1.4)	5.6, 6.8	6.5(1.2)	5.9, 7.0	5.7(0.9)	5.3, 6.2	5.3(1.6)	4.4, 6.1
	Older	4.7(1.0)	4.2, 5.1	5.3(0.9)	4.9, 5.7	5.2(0.8)	4.9, 5.5	5.3(0.8)	5.0, 5.6
ΔHbO	Young	1.5(0.7)	1.3, 1.8	0.8(0.3)	0.6, 0.9	0.9(0.5)	0.6, 1.1	1.2(0.5)	1.0, 1.5
	Older	0.7(0.2)	0.6, 0.8	1.1(0.4)	0.9, 1.2	0.6(0.4)	0.5, 0.7	1.1(0.3)	1.0, 1.6

5.3.5 Correlations between behavioral measures and hemodynamic responses

Pearson correlation coefficients (r) are computed to investigate potential correlations between behavioral (AAP) and hemodynamic responses (mean ΔHbO amplitude) during the participants' risk outcome phase. Results are presented in Figure 5-9, where the upper plots described the correlations in young adults [Figure 5-9(a) for win case and (b) for lose case], and the lower plots displayed the correlations in older adults [Figure 5-9(c) for win case and (d) for lose case]. With higher average adjusted pumps (6.2 ± 1.4), the young males had stronger mean ΔHbO amplitudes (1.5 ± 0.7) [Figure 5-9(a), blue, $r = 0.62$, $p < 0.01$] while young females ($n = 17$) revealed no correlations [Figure 5-9(a), red]. In the lose case, however, young females are shown to have lower average adjusted pumps (5.3 ± 1.6) accompanied by a stronger mean amplitude (1.3 ± 0.5) [Figure 5-9(b), red, $r = -0.71$, $p < 0.01$] and no correlations are observed in young males [Figure 5-9(b), blue]. Furthermore, both older male adults ($n = 22$) and older female adults ($n = 38$) revealed no significant correlations in win cases [Figure 5-9(c)]. However, with lower average adjusted pumps in both older male adults (5.3 ± 0.9) and older female adults (5.3 ± 0.8), there are corresponding higher mean ΔHbO amplitudes for older male adults (1.08 ± 0.35) and older female adults (1.1 ± 0.3) in lose cases [older males adults: Figure 5-9(d), blue, $r = -0.87$, $p < 0.01$; older females adults: Figure 5-9(d), red, $r = -0.58$, $p = 0.02$]. Correlation coefficients in all cases are summarized in Table 5-4.

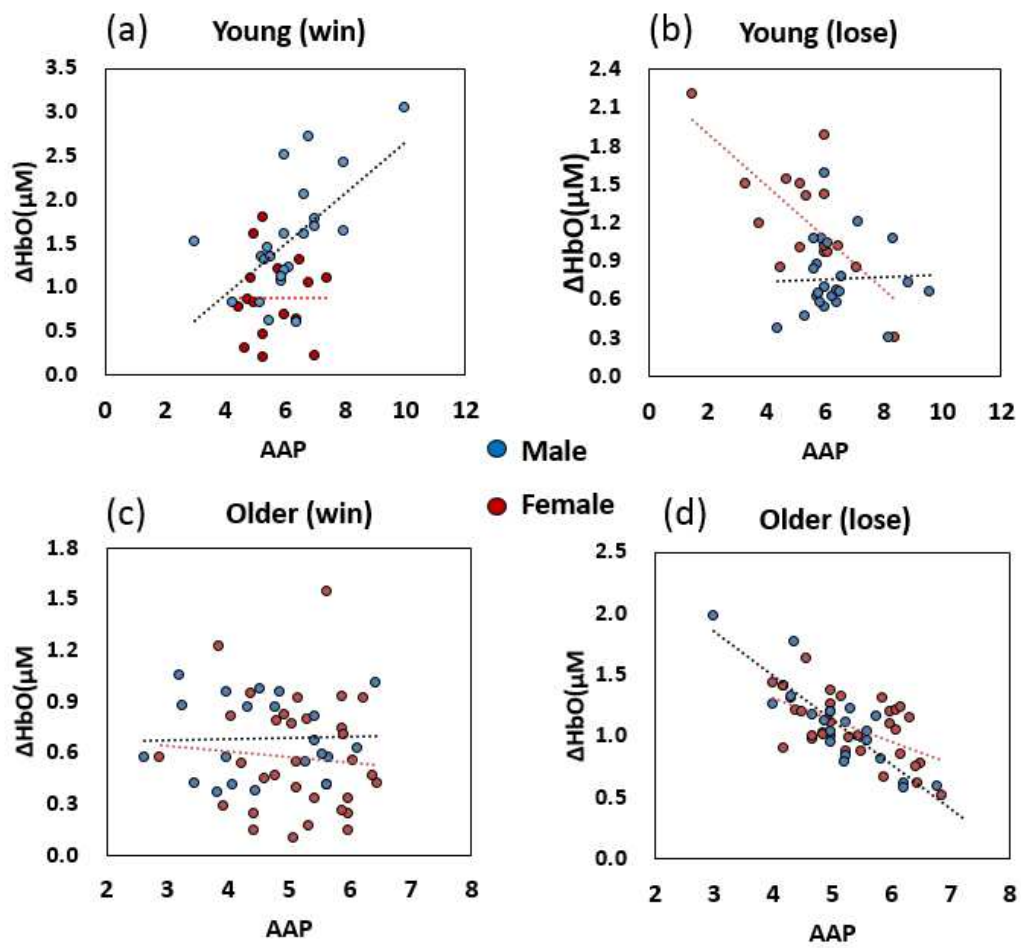


Figure 5-9 Correlation plots between the behavioral measure (AAP) and hemodynamic changes (ΔHbO) for male (blue) and females (red) in young adults (upper) and older adults (lower) groups.

Table 5-4 Correlation coefficients (r) of behavioral measures and hemodynamic amplitude changes in males and females within young and older adult groups

	male				female			
	win		lose		win		lose	
	r	p -value	r	p -value	r	p -value	r	p -value
Young adults	*0.62	<0.01	0.03	0.88	0.00	0.99	*-0.71	<0.01
Older adults	0.03	0.89	*-0.87	<0.01	-0.28	0.10	*-0.58	0.02

* Correlation is significant at $p < 0.05$ (two-tailed).

5.4. Discussion

The present fNIRS study comprehensively investigated age and gender effects on risk decision-making processes and outcomes using atlas-DOT. Depth-enhanced brain images are obtained by the 3D reconstruction algorithm. Two phases of the BART protocol (decision-making and outcome) are separately analyzed by applying GLM with two regressors; age- and gender- dependent statistical parametric maps are generated to quantify the brain hemodynamic responses. The results showed that age and gender have significant effects on prefrontal activations. First, different activations in prefrontal regions during risk decision-making stimulation are observed within young and older adults. Cortical activations for young adults occurred in the bilateral DLPFC with focused ROI patterns, while older adults demonstrated enlarged diffuse ROI patterns in bilateral RLPFC and the DLPFC regions. Reduction of ROI-averaged ΔHbO amplitudes are also observed in older adults. Second, gender differences for brain activations are observed in young adults but not in older adults during win/lose outcomes. Third, differences in behavioral-hemodynamic correlations are observed between males and females in young

adults but not in older adults. This is the first fNIRS study to report age- and gender-effects in neural correlates and hemodynamic activations.

5.4.1 Age effects

Cortical activation maps obtained using atlas-DOT and GLM analysis demonstrated age-related hemodynamic responses under the two-phase BART paradigm, modified for fNIRS. Both young and older adults showed strong dorsolateral prefrontal cortex (DLPFC) activations during decision making [Figure 5-4]. This finding supports the key roles of the DLPFC: working memory, learning and cognitive functions [136]–[141]. In addition, these results are strongly consistent with a previous fMRI study, which applied the BART paradigm to 14 healthy young adults and obtained bilateral DLPFC activations [82]. Brain hemodynamic changes in young adults are significantly higher than in older adults during win cases. Young adults also revealed more focused bilateral DLPFC activations compared with older adults. Dong et al. (2014) purport that young adults, more than older adults, are motivated by intent to win, thus evoking more DLPFC hemodynamic responses [124].

Older adults demonstrated increased ROI volumes in DLPFC regions during the decision-making phase (Figure 5-4). Increased ROI volumes (Figure 5-5(b)) are also observed in older adults when the outcomes are losses. Those findings could be explained by known age-related neural changes: decreased gray matter density causes the brain to compensate for increased work load by recruiting additional neural cells in neighboring functional regions [142]–[145]. Recent fMRI studies have also reported this compensation mechanism in older adult brains, involving larger areas of activations in the posterior and PFC regions with decreased amplitudes during risk/reward-related neurocognitive performances [3], [4].

Older adults demonstrated brain activations in the RLPFC in lose cases. Though the function of the RLPFC has not been fully explored, the RLPFC is regarded as functioning like ‘cognitive branching’ [146], with its core role as connector of neighboring regions, such as the ventromedial prefrontal cortex ([vmPFC]; [146], [147]). The vmPFC acts as the center of decision-making processes, especially under reward-related or “economic” options [148], [149]. Studies also suggest that vmPFC functions as regulator of emotion (Hänsel & von Känel, 2008). Older adults are known to be more emotionally driven [3], [5], and probably, more affected by negative-induced emotions in the face of losses. Other studies using the Iowa Gambling Task (IGT) also reported that older adults pay greater attention to emotional information requiring engagement of RLPFC and vmPFC to perform emotion-related brain reactions [147], [150].

5.4.2 Gender effects

5.4.2.1 Gender effect in young adults

Our results indicated the existence of gender effects on neurocognitive functions with risk-taking outcomes in young adults, but not in older adults. Strong brain activations in the DLPFC (right side biased) are observed in young males in win cases but reduced brain activations are observed in lose cases (Figure 5-5(a), red]. An fMRI study on IGT reported that males activated the right side of their DLPFC in the face of long-term winning decks [11]. Another fMRI study, with all male subjects (21-31 years) who completed a gambling risk task, reported more right-sided DLPFC activations with risk taking outcomes [151]. In the current study, DLPFC activations (right side biased), in young adult males, are significantly linked to risk-taking behaviors as evidenced by their willingness to inflate balloons larger in order to increase monetary rewards (but risk a balloon explosion and loss of accrued money). It is further suggested by several groups that the males (not females) exhibited suppressed brain activations in the OFC,

amygdala and ventral striatum, with occasional losses in order to achieve long-term winnings [11], [152], [153]. Thus, the decrease of DLPFC activation in lose cases in males could be associated with the suppression effect under negative outcomes.

In addition, young males also demonstrated strong ROI-averaged activation amplitudes which are significantly associated with high risk scores in win cases (Figure 5-9(a), blue]; no hemodynamic-behavioral correlations are observed for males in lose cases (Figure 5-9(b), blue]. As suggested by [16], a positive correlation between hemodynamic responses and risk behavior represented a risk-seeking performance, while a negative correlation revealed a risk-averse performance. This finding indicated that young adult males are more focused on wins instead of losses (more risk-seeking). Gardner and Steinberg (2005) supported these behavioral findings: young males ($n = 306$, age > 24) described stronger risk-seeking behaviors than females during risk questionnaire tasks [154].

Young adult females showed weak right-sided DLPFC activations in win cases (Figure 5-5(a), yellow], but increased bilateral DLPFC activations in lose cases (Figure 5-5(a), yellow]. Similar findings from an fMRI study using a risk-taking task ($n = 22$, 10 females) reported increased brain activations in the PFC regions of young female adults after punishment [12]. McRae et al. (2008) also reported that females required more neural processing than males under the same level of risk to evaluate uncertainty and negative outcomes related to risk decisions [13]. Moreover, fMRI studies suggested that the DLPFC is important in controlling negative emotions during IGT tasks [11], [130]. Specifically, an fMRI study with depression simulations in 24 young adults (12 females) indicated that females have stronger activations in left DLPFC than males [130], which is consistent with our current findings (female $>$ male in left DLPFC). Thus, the gender-dependent differences in brain activations under BART stimulation could possibly linked

to the differences in cognitive control between males and females in regulation of positive emotions (i.e., induced by win outcomes) and negative emotions (i.e., induced by lose outcomes). However, gender-dependent differences for neurocognitive performances are still not fully explored.

In addition, no correlations are observed in young females in win cases (Figure 5-9(a), red], but low risk-taking behaviors correlated with strong bilateral DLPFC amplitudes in lose cases (Figure 5-9(b), red]. These risk-averse performances are consistent with previous findings which reported less risk-seeking tendencies and greater perceptions of negative outcomes in young females than males [155], [156]. Fecteau et al. (2007) also suggested that higher levels of bilateral DLPFC activations are associated with less risk taking [157].

5.4.2.2 Gender effect in older adults

No gender differences are observed in older adults. Both older adult males and females produced reduced amplitudes in neural responses with win cases and large diffuse bilateral DLPFC and RLPFC activations in lose cases (Figure 5-5 (b) & Figure 5-8]. A paucity of research studies have investigated brain-behavior relations in older adults under risk taking. One possible reason for the reduction of brain activations in win cases could be the minimal amount of attention that older adults give to immediate rewards [158]. The fMRI-based study used a monetary decision-making task (n = 15, age from 65 to 80) and reported reduced sensitivity in older adults to immediate rewards as well as no correlation between BOLD signal and delay discounting, a parameter that measures the reduction of rewards as a function of the time [158].

No empirical evidence exists to support or explain the lack of gender-related differences in neural activations during older adult risk decision making. It is suggested that gender differences on lateralization in brain anatomy, such as in brainstem,

cerebellum and amygdala, are associated with gender differences on emotion-driven brain activities, but limited evidence supports this association on lateralization in the frontal cortex [159]. A brain structure study using MRI (n = 330, 120 males, age from 66 to 96 years) investigated the age (grouped by 65, 70, 75, 80, 85, 90, 95 years) and gender effects on changes in regional brain size and indicated: (1) significant decline of cerebral hemisphere volume in frontal region and temporoparietal region is associated with increase of age, and (2) even though the older adult male brain is more symmetrical towards right side in frontal cortex, no main effect on age or gender for the regional cerebral size is observed in the above regions [122]. So, lateralization in older adults may not affect neurocognitive performances under BART stimulations. Instead, similar brain volumes and sizes in frontal cortices in both older male and female adults may be associated with parallel brain activations during BART performances. In addition, both groups demonstrated consistent hemodynamic-behavioral correlations in win and lose cases (Figure 5-9 (c) & (d)). Strong ROI-based ΔHbO amplitudes with low risk scores are observed in lose cases in both older male and female adults (Figure 5-9(d)), revealing risk-averse performances. Deakin et al. (2004) reported increased risk-avoidance behavior in aging, where a Decision-Gamble task is performed to 177 healthy participants (age from 17 to 77 years) and revealed that the increase of age is associated with reduction of risk tolerance factor (risk behavior to judge personal risk) [160].

5.4.3 Study limitations and future work

Though the atlas-DOT with GLM method significantly improved the image quality and protocol modeling ability, several limitations need to be addressed in future studies: (1) the imaging depth for fNIRS is limited by the maximum penetration depth of near-infrared light in the human brain, 30 to 40 mm as the maximum [131], [161]. Thus, the activations in the deep brain are unable to be detected by fNIRS. A possible solution

could be combining fNIRS with other modalities, such as PET/SPECT and MEG, which are able to monitor the deep activities of the brain. (2) The optical probes used in the current study covered only prefrontal regions. Since the brain is an integrated and complex system, it is crucial to detect whole cortical regions in the assessment of cognitive functions. Future work is suggested to increase the number of optical fibers to be able to cover the whole cortical areas. In this way, both local features and global information could be obtained. (3) Aging effect is a continuous process. This study investigated two age groups with young adults, 25 to 43 years, and older adults, 65 to 92 years. However, researchers have indicated other critical age periods with rapid brain anatomical, chemical, and functional changes. For instance, age groups such as youth (7-15 years), adolescents (15-24 years), and mid-age (45-60 years) also have specific features of brain network development and physical structure organization. It is suggested to include other age groups in future neuro-behavioral research to determine age and gender effects.

5.5 Summary

This chapter reports the use of a newly-developed atlas-guided diffuse optical tomography to investigate age and gender effects during risk decision making. This depth-compensated image reconstruction algorithm is shown to efficiently monitor cortical activations. With the GLM approach, statistical parametric maps under two phases (pre- and post-risk decision making) of the BART protocol are obtained. Noticeable differences in age- and gender-dependent neurocognitive performances are observed. Age comparison reveals an increase of ROI regions combined with a decrease of ROI-averaged ΔHbO amplitudes in older adults, indicating compensatory efforts to allocate more neural resources to attentional and risk-taking processes in order to maintain neurocognitive performances at the level seen in young adults. Results also suggest that

emotional regulation could play a key role leading to gender differences in neurocognitive functions. Furthermore, brain-behavior correlations supported “risk-taking” patterns in young males. On the contrary, both young females and older adults (both males and females) are “risk-averse”. This study discovers significant age effects on prefrontal activations during risk decision-making processes and outcomes. Future life span research studies, which include more age groups, e.g., adolescence (18-25), and mid-age adults (45-65), are needed.

Chapter 6

Implement of Graph Theory Analysis to Atlas-DOT to Investigate Age-related Brain

Functional Connectivity

6.1. Introduction

6.1.1 Significance, backgrounds and goals

The human brain is naturally a complex network, which is constituted with local nodes (e.g., the significant anatomical regions) and edges (e.g., the internal connections between two or more brain regions with certain familiarity). Research reports have indicated that the aging process is not only associated with brain anatomy and cognitive changes, but also accompanied with reorganizations of brain networks [162]–[164]. Recent brain network studies suggest that the gray matter decline is the most significant leading factor that changes brain network properties in prefrontal regions in the aging process [164], [165].

Recent advances in techniques of forming brain networks involves graph theory analysis (GTA) [23], [24], [166]. This method has been increasingly applied in functional brain image modalities, such as fMRI [23], [24], [166]–[168] and PET [164]. Most recently, GTA has been applied to fNIRS, which has been proved to be efficient and reproducible in assessment of resting state functional connectivity (RSFC) [68], [109]. However, the current widely used fNIRS imaging method, namely fNIRS topography, lacks of spatial information and limits by its depth accuracy and spatial resolution [42]. In addition, little is known about feasibility of the fNIRS method in tracing the age-related changes of functional brain networks. The purpose of this chapter is to explore an new atlas-DOT algorithm with the spatial-temporal mapping ability to investigate age-dependent resting state brain networks.

6.1.2 Characteristics of brain networks along aging

The brain is naturally a complex system within which the nerve cells are linked by a dense web of intricate connectivity. The complex brain network is constituted in multiple scales, from single nerve cells to functional brain regions, linking the brain and body in a complete organism [169]. Studies on brain networks have rapidly increased in recent years, not only for a better understanding of the nature of the brain but also for potential protections of brain network decay along aging [162], [163], [170]–[173]. It is known that maturational formation of brain networks are the results of growing processes [168], [174], [175]. The combination of growing process operation, remodeling and organization of neuronal connections are continuous throughout the life span [162], [171], [172]. Development of neural cells and synaptic connections shape the topology of brain network. Thus, it is impossible to fully understand the aging effect on brain functions without considering the growth and development of brain networks.

Recent studies indicate that the age-related physical changes in the human brain are associated with changes of intrinsic brain networks. As people age, significant changes of white matter alter the large-scale white matter pathway [162]. In addition, about 5% of gray matter declines each year after the age of 65, and this decline process has been observed to first happen in the prefrontal cortex [9]. Decline of gray matter density has been associated with decreases in small-world properties, such as a decrease in global efficiency with an increase of path length [172]. Studies have also reported progressive decrease in default mode activity as people age [163]. Moreover, age effect is also reported to be associated with significant changes in the network modules and the interlinking hubs between different modules [170].

6.1.3 Atlas-guided diffuse optical tomography implemented with graph theory analysis

Over the last decade, researchers have developed a large amount of mathematical frameworks with sophisticated analytic strategies that can be utilized to analyze neuroimaging data, and to quantitatively model the brain as a complex network. Noninvasive brain imaging methods, such as fMRI and PET, can map the patterns of either structural or functional connectivity of the human brain. Graph theoretical modeling is one of the advanced methods, which can provide an uncomplicated but powerful mathematical means to characterize topological properties of the brain networks [23], [24], [166], [176]. Routinely used GTA in fMRI, PET and other volumetric brain imaging methods follows two major steps: (1) graph formation from the spatial-temporal functional brain images and (2) quantification of graph parameters as local and global brain network characteristics based on the graph theory metrics. However, few study has reported application of GTA to fNIRS data for complex brain network analysis. Very recent studies have demonstrated the feasibility and validity of combining GTA with channel-wise fNIRS, giving rise to the topological characterization or organization of human brain networks [68], [109], [177], [178]. However, the fNIRS topographical-based method utilizes channel-wise measured data in graph formation, not able to assess the volumetric cortical information and without depth resolution.

My study in this Chapter utilizes the newly developed atlas-DOT [105] to form 3D cortical images in time series and to obtain correlation-based brain networks across PFC. Based on this approach, I consequently investigate the age-related prefrontal network changes in the resting state. As compared to fNIRS topography, atlas-DOT (or fNIRS tomography) enables us to improve spatial resolution and depth accuracy of connectome maps [43], [105]. Furthermore, the standard spatial brain labelling technique is applied to the atlas-DOT approach to achieve comparable results. My study chooses a routinely

used automatic anatomical labeling (AAL) template for node extraction in graph formation [179]. The AAL node coordinate system, which contents 116 brain anatomical regions in Montreal Neurological Institute and Hospital (MNI) space, has been widely used in the fMRI and PET field as the standard brain atlas for graph formation.

6.1.4 Study aims and purpose

This chapter aims to combine the atlas-DOT with graph theory analysis to assess age-related changes in prefrontal cortex network properties at resting state. This chapter is organized as follows: First, I introduce the technique development about the graph formation using atlas-DOT with spatial-temporal nodal extraction. Second, quantifications of brain network parameters are given for the prefrontal regions from both young and older adults during resting state. Third, comparison of local and global brain network parameters is made between the two age groups. This chapter also aims to validate the feasibility of atlas-DOT technique being able to reveal the difference in brain network characteristics and connectomes in young and older adults under resting state.

6.2 Material and method

6.2.1 Participants and data acquisition

A total of 37 subjects participated in this study, including fifteen young adults (from 25 to 33 years, 27.86 ± 2.68) and twenty-two older adults (from 71 to 92 years, 77.23 ± 1.65). All subjects were right-handed with normal visual ability. No subjects reported any known diseases, such as musculoskeletal, neurological, visual, or cardio-respiratory dysfunctions. Two groups were selected properly. The age range for young adult group was chosen based on the approximated ages for PFC maturation [132], and older adult group was chosen due to the documented rapid decline of gray matter density after age of 65 [133]. Before the measurement, all participants were instructed to sit comfortably in a quiet room with eyes closed. A ten-minute, resting-state protocol was

then performed in the dark room by asking the participants to sit at a stable position with minimum body movements. One older adult subject was excluded due to failure of finishing the 10-minute measurement. Written consent forms were obtained for all participants before protocol started. This study was approved by the Institutional Review Board of the University of Texas at Arlington.

During the protocol, a continuous wave (CW) fNIRS brain imaging system (Cephalogics, Ishington Univ., USA) was applied to each subject's forehead to record the brain hemodynamic changes during resting state (see Figure 6-1(a)). The wavelengths used to calculate changes of oxygenated hemoglobin (ΔHbO) and deoxygenated hemoglobin (ΔHbR) were 750 nm and 850 nm. The sensor array consisted of 16 sources and 16 detectors with a nearest inter-optode distance of ~ 3.5 cm, forming 72 measurement channels and covering the forehead entirely. To find anatomical locations of the optodes, an international 10 to 20 system of electrodes placement was used to co-register the sources and detectors to a standardized brain atlas. Figure 6-1(b) shows the probe geometry overlaid on the frontal cortex of the ICBM152 brain template [51]. The region of detection (ROD) was about $10\text{ cm} \times 20\text{ cm} \times 3\text{ cm}$, which mainly covered the Bordman area 9, 10 and 11. The detected fNIRS signals were acquired at a sampling frequency of 10.8 Hz.

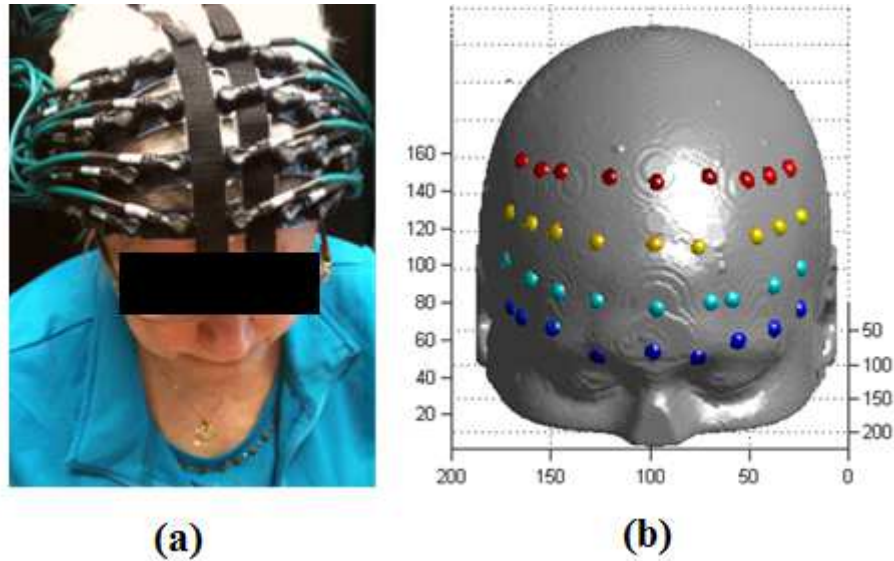


Figure 6-1 Experimental setup and detection regions. (a) Optical probe placement in the forehead of a participant. (b) Optodes co-registration in the ICBM 152 brain atlas. Region of detection (ROD) majorly located at frontal and prefrontal cortex, covered a $20 \times 10 \times 4$ cm regions with 32615 voxels.

6.2.2 Data processing

Time sequences of light density changes from 72 channels were recorded for all participants during the 10-minute resting-state period. A general atlas-DOT routine was applied to the raw recorded data to form spatial-temporal brain maps. Three major steps, namely, data preprocessing, forward modeling and image reconstruction were performed. Details on atlas-DOT algorithms are introduced in [105] and are briefly summarized as follows.

During data preprocessing, the band-pass filtering and global autocorrelation process were sequentially applied to the channel-wise raw data. Specifically, the band-pass filter chosen in this study was 0.02 to 0.3 Hz as suggested by a previous study to eliminate the physiological noise generated by heart beat and respirations [105]. A global

autocorrelation was applied to the channel-wise fNIRS signals to further eliminate the unmodeled global physiology or structure noise [102]. Specifically, for each participant, a global signal was generated by averaging over 72 channel time sequences. Then an autocorrelation approach was applied between the globally averaged signal and signals from each individual channel to perform global regression. An arbitrary threshold of $|R| > 0.2$ is chosen to eliminate the strong motion artifact channels [180].

After data preprocessing, a 3D forward modeling with depth compensation algorithm was performed. The pre-designed ICBM152 head template including 176192 voxels was served as the brain atlas for photon migration. The light sensitivity matrix (or Jacobin matrix) was obtained by performing finite element estimation of light propagation inside the ICBM152 brain atlas, using a FEM-based MATLAB package, NIRFAST [52]. A depth compensation algorithm (DCA) was further applied to the sensitivity matrix to enhance the deeper brain signals [47]. To recover spatial-temporal changes of light absorptions due to the brain hemodynamic responses, a 3D image reconstruction approach was then conducted. The inverse image reconstruction was performed using Moor-Penrose generalized approach with Tikhonov regularization [54]. The reconstructed images was a 4-D matrix with 176192 voxels and 6480 temporal points. Each data was also translated into the MNI space after image reconstruction. Consequently, determination of absorption changes at two wavelengths led to reconstructed images of relative changes in ΔHbO and ΔHbR concentrations, based on spectral decomposition of the extinction coefficients for both wavelengths [42]. In addition, brain maps with 32615 voxels from region of detection (ROD) areas by 6480 time points (10 minutes) were extracted as the spatial-temporal images for functional brain network formation.

6.2.3 Construction of functional brain networks

Two major steps, namely, graph formation and network parameter quantification, are suggested in the GTA. In general, graph formation utilizes averaged regional cortical responses as the sources and performs the cross-correlation between the sources to form a cross-correlation matrixes (or adjacency matrixes). The local and global graph parameters are then quantified from the cross-correlation matrixes as the brain network characteristics.

During the graph formation in my study, three sub-steps, namely, regional parcellation, node extraction and cross-correlation were performed. First, a regional parcellation was applied to the atlas-DOT images to generate anatomical region of interest. Specifically, the AAL 116 atlas was applied to separate the brain into 116 anatomical regions based on the landmarks of cortex and subcortical structures. Six brain networks, namely, default mode (yellow), sensorimotor region (navy blue), frontal-parietal lobe (light blue), occipital lobe (blue), limbic lobe (orange) and cerebellum (red) are identified from the previous studies and presented here using different colors (see Figure 6-2(a)) [181]. To illustrate details of the atlas plot, three planes from coronal, axial and sagittal views of the ICBM152 brain template with AAL116 regions are imaged by BrainNet Viewer software [182].

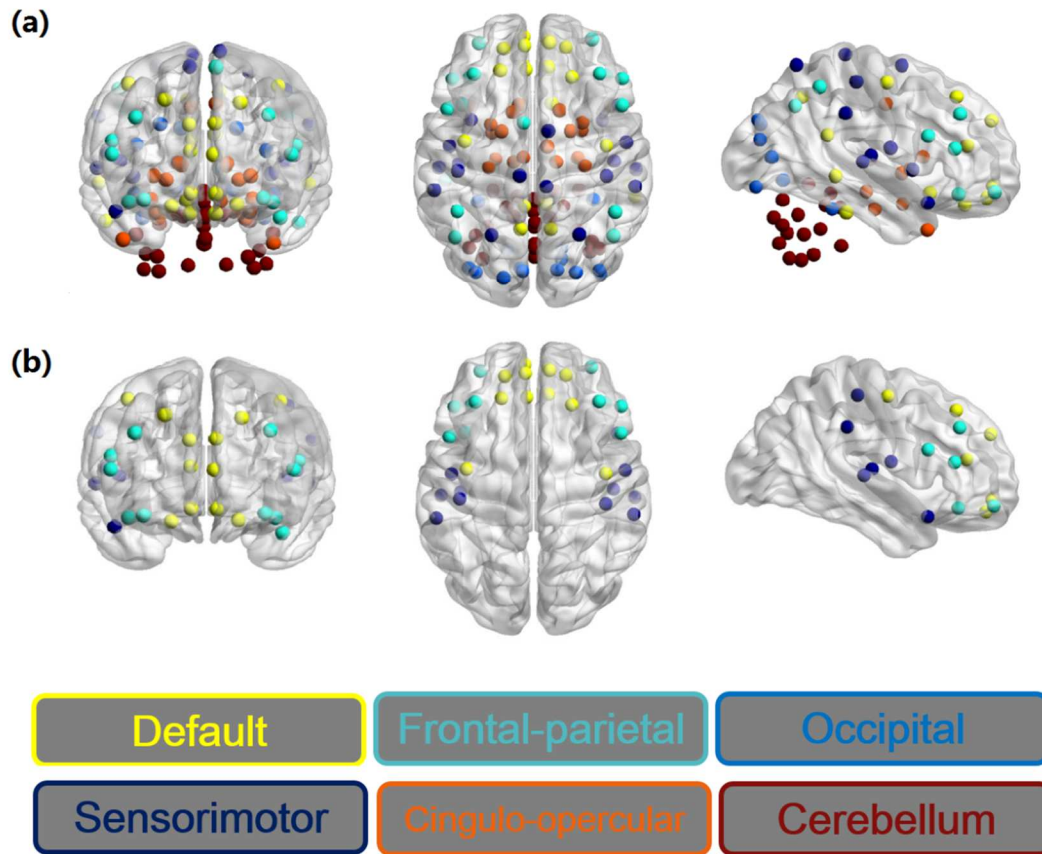


Figure 6-2 Region of interest (ROI) based on Automatic Anatomical Labelling (AAL). (a) Placement of 116 AAL regions with ICBM 152 brain template. (b) 34 node positions extracted based on the detected regions and AAL 116 templates.

Table 6-1 Node positions in this study

Region	Anatomical description	Label	x	y	z
Default mode	Left precentral gyrus	PreCG.L	-38.65	-5.68	50.94
Default mode	Right precentral gyrus	PreCG.R	41.37	-8.21	52.09
Default mode	Left superior frontal gyrus (dorsal)	SFGdor.L	-18.45	34.81	42.20
Default mode	Right superior frontal gyrus (dorsal)	SFGdor.R	21.9	31.12	43.82
Default mode	Left orbitofrontal cortex (superior)	ORBsup.L	-16.56	47.32	-13.31
Default mode	Right orbitofrontal cortex (superior)	ORBsup.R	18.49	48.1	-14.02
Frontal-parietal	Left middle frontal gyrus	MFG.L	-33.43	32.73	35.46

Table 6-1—Continued

Frontal-parietal	Right middle frontal gyrus	MFG.R	37.59	33.06	34.04
Frontal-parietal	Left orbitofrontal cortex (middle)	ORBmid.L	-30.65	50.43	-9.62
Frontal-parietal	Right orbitofrontal cortex (middle)	ORBmid.R	33.18	52.59	-10.73
Frontal-parietal	Left inferior frontal gyrus (opercular)	IFGoperc.L	-48.43	12.73	19.02
Frontal-parietal	Right inferior frontal gyrus (opercular)	IFGoperc.R	50.2	14.98	21.41
Frontal-parietal	Left inferior frontal gyrus (triangular)	IFGtriang.L	-45.58	29.91	13.99
Frontal-parietal	Right inferior frontal gyrus (triangular)	IFGtriang.R	50.33	30.16	14.17
Frontal-parietal	Left orbitofrontal cortex (inferior)	ORBinf.L	-35.98	30.71	-12.11
Frontal-parietal	Right orbitofrontal cortex (inferior)	ORBinf.R	41.22	32.23	-11.91
Sensorimotor-temporal	Left rolandic operculum	ROL.L	-47.16	-8.48	13.95
Sensorimotor-temporal	Right rolandic operculum	ROL.R	52.65	-6.25	14.63
Default mode	Left superior frontal gyrus (middle)	SFGmed.L	-4.80	49.17	30.89
Default mode	Right superior frontal gyrus (middle)	SFGmed.R	9.10	50.84	30.22
Default mode	Left orbitofrontal cortex (medial)	ORBsupmed.L	-5.17	54.06	-7.40
Default mode	Right orbitofrontal cortex (medial)	ORBsupmed.R	8.16	51.67	-7.13
Default mode	Left anterior cingulate gyrus	ACG.L	-4.04	35.4	13.95
Default mode	Right anterior cingulate gyrus	ACG.R	8.46	37.01	15.84
Sensorimotor-temporal	Left postcentral gyrus	PoCG.L	-42.46	-22.63	48.92
Sensorimotor-temporal	Right postcentral gyrus	PoCG.R	41.43	-25.49	52.55
Sensorimotor-temporal	Left supramarginal gyrus	SMG.L	-55.79	-33.64	30.45
Sensorimotor-temporal	Right supramarginal gyrus	SMG.R	57.61	-31.5	34.48
Sensorimotor-temporal	Left transverse temporal gyrus	HES.L	-41.99	-18.88	9.98
Sensorimotor-temporal	Right transverse temporal gyrus	HES.R	45.86	-17.15	10.41
Sensorimotor-temporal	Left superior temporal gyrus	STG.L	-53.16	-20.68	7.13
Sensorimotor-temporal	Right superior temporal gyrus	STG.R	58.15	-21.78	6.80
Frontal-parietal	Left superior temporal pole	TPOsup.L	-39.88	15.14	-20.18
Frontal-parietal	Right superior temporal pole	TPOsup.R	48.25	14.75	-16.86

Second, the node extraction was performed based on the AAL 116 atlas. As indicated in Figure 6-1(b), the ROD reached by our optical detection is mainly on the prefrontal cortex, including parts of default mode, frontal-parietal and sensorimotor region. Thus, the nodes in this study were defined within the AAL anatomic regions overlapped with ROD. As a result, a total 34 nodes (see Figure 6-2(b)) were identified as

nodes for my study. Table 6-1 lists the names, regions, labels and coordinates of 34 nodes. In addition, in order to quantify the hemodynamic changes in each node region, the 10-minute pixel-wise ΔHbO values within each node region were averaged to form a total 34 mean regional hemodynamic responses for cross-correlation calculations in the following step.

Former studies using fNIRS suggest that the brain functional connection could be represented by correlations among brain hemodynamic changes across different brain regions [68], [109], [177]. The same strategies were applied to nodal ΔHbO data across the 10-minute resting state period to establish the adjacency matrix for each participants. Figure 6-3(a) illustrates a temporal plot of nodal HbO values from one subject (subject 01). Specifically, x-axis represents time within 10 minutes of a resting-state period and y-axis represents the oxygenated hemoglobin changes with the node index from 1 to 34. The cross-correlation between each pair of nodes was then performed for the given time series and the Pearson correlation coefficients (R) were computed to form a 34×34 adjacency correlation matrix (see Figure 6-3(b)). Note that the color in Figure 6-3(b) denotes the values of correlation coefficient; blue color indicates low correlation coefficient and red represents high correlation coefficient.

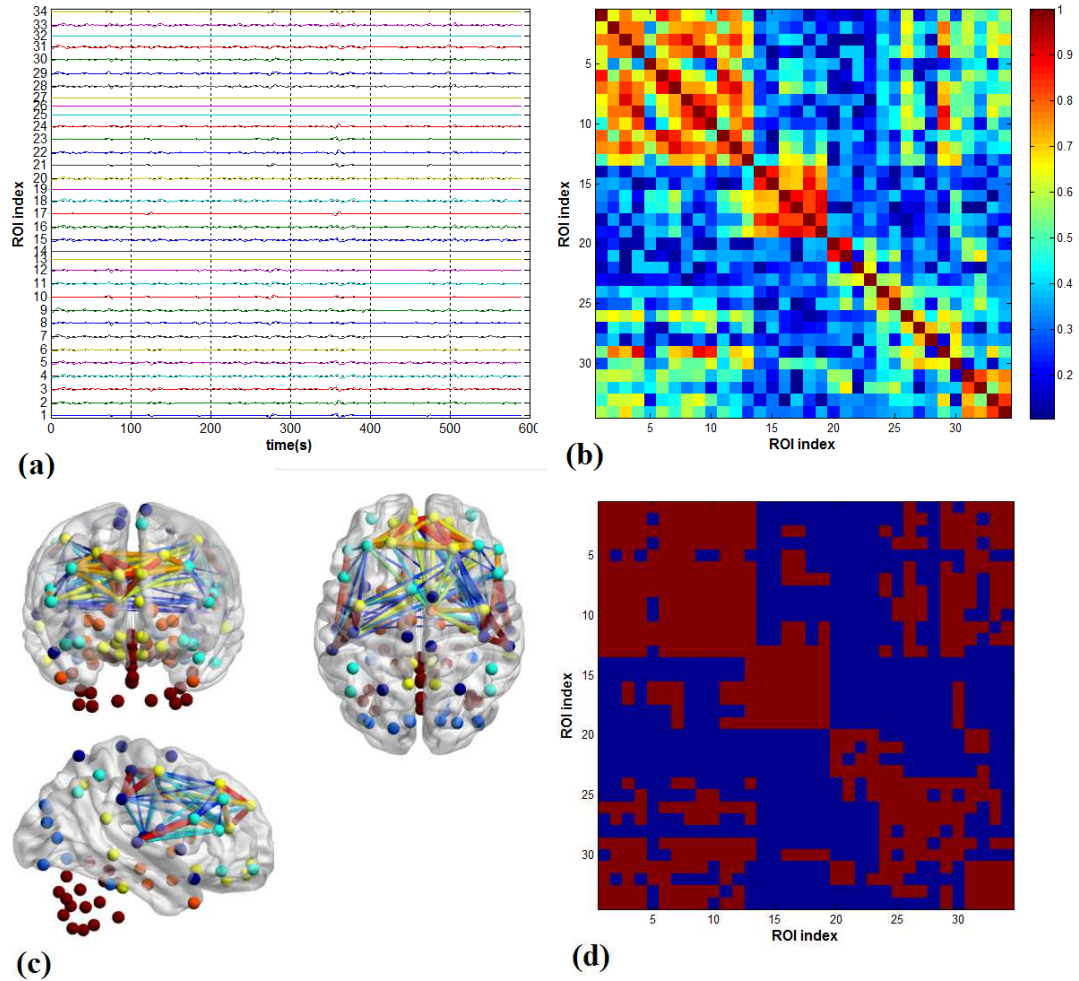


Figure 6-3 (a) Illustration of temporal plots of HbO values within 10 minutes of resting state at 34 nodes. (b) The adjacency matrix generated by cross-correlation of ΔHbO values at 34 nodes; x-axis and y-axis represent the node numbers; red color represents high correlations between the temporal profiles of two nodes, while blue color represents low correlations. (c) The spatial representation of nodes and edges based on DOT measurements. (d) The binary matrix threshold by sparsity of 0.26.

The adjacency matrix was further converted into a binarized matrix by setting a threshold. The correlation coefficient between node i and j ($i, j = 1, 2, \dots, 34$) was set to 1 if

the correlation value was larger than the given correlation threshold and 0 otherwise (see Figure 6-3(d)). The edge was defined as the functional connections (either = 1 to represent a significant correlation between two nodes or = 0 to represent no significant correlation). In this chapter, I applied different thresholds in the cross-correlation matrix to obtain a sequence of binary matrixes. Specifically, the sparsity-based approach was applied as suggested by [109]. The sparsity (S) is defined as the threshold by the number of actual edges in a network divided by the maximum possible number of edges in a network. In this chapter, the range from 0.05 to 0.5 (i.e., $0.05 < S < 0.5$, interval = 0.01) was chosen to be the standard threshold sequence as reported in a previous study [164]. Then the threshold sequence was applied to the adjacency matrix to generate a total of 34 binarized network matrix for each subject. Figure 6-3(c) illustrates a spatial representation of nodes and edges from one binary matrix with a given/fixed threshold. Colors of nodes represent different brain anatomical regions, while lines between two nodes represent respective connections. Differed from the channel-wise approach, the atlas-DOT combined with the depth compensation algorithm is able to reconstruct hemodynamic signals from a deeper brain region. Thus, temporal profiles from cortical nodes and their connections (see Figure 6-3(c)) could be computed using my atlas-DOT with DCA approach.

6.2.4 Graph theory analysis

Quantifications of mathematical parameters are the basis of graph theory approach. From a small to large scale, there are three types of graphical parameters. The first type of graphical parameters are nodes, $N_i, i = [1 n]$, and links, $L_{ij}, i, j \in N$, between pairs of nodes. They are the basic mathematical representations of a real-world complex system [176]. The nature of nodes and links in an individual brain network can be represented by functional brain mapping methods. Specifically, nodes in anatomical

mapping could be the representation of white matter tracts. Nodes in functional mapping should be functional pixels indicating measurable magnitudes or hemodynamic changes of a temporal profile. Links are a type of connectivity features of two nodes. In anatomical mapping, edges could be the identical thickness of two gray matter layers, while in functional mapping, edges could be the correlation between two separate nodes. Links are divided into binary links and weighted links. Binary links represent the presence or absence of connections, while weighted links contain information about connection strengths [176]. Another basic measure of brain networks is known as the degree. The degree is equal to the number of links that are connected to an individual node. The degree $K_i, i \in N$ of an individual node reflects its importance among all the nodes. The more connection it has by other nodes, the more pivotal of this individual node is within a network. In addition, the degree distribution is an important marker to illustrate the development and organization of the network [183].

Second type of brain network metrics is the functional local segregation. It represents the existence of interconnected groups of brain regions. The parameters within this type are the local features of a complex network. Clustering coefficient and network modularity are two parameters from this type. The clustering coefficient, $C_L(i), i \in N$, represents the occurrence of regional connectivity around individual nodes [183]. While network modularity Q is the measure of anatomic or functional structures of networks [184], it is designed to measure the strength of separation of a network into sub-units. Networks with high modularity have dense connections between the nodes within modules. The detection of modularity in a network is to find the partition, p , that maximizes the modularity Q . In practice, a Q value above 0.3 is a good value of significant modules in a network [185]. Other important local feature is hub. It is the identification of importance of a node within networks. A node with a larger number of

functional interactions in a network is regarded as hub. The major way of quantifying hubs is to compute the node degree, closeness and betweenness centrality $N_{bc}(i), i \in N$. Closeness centrality denotes the direct influence over the nodes while betweenness centrality represents the ability an individual node in the control of information flow within certain module. A large impacts of the node has high betweenness and important on controlling the information flow over the whole network [186].

The third type of brain network metrics is the global integration. Functional integration in the brain is associated with the ability to combine information from distributed brain regions [176]. The metrics within this type are based on shortest path length d_{ij} , nodal efficiency E_{nod} and global efficiency E_{glob} . Shortest path length denotes the shortest distance from one node traveling to other nodes. Network efficiency is a more biologically relevant metric to describe brain networks. Nodal efficiency $E_{nod}(i), i \in N$ is to measure the ability of a network to transmit information over a local subset of nodes[187], and the global efficiency E_{glob} is to measure the ability of a network to transmit information over the whole network [188].

As indicated above, different scales of brain network features are presented. From local to global, each type of network feature represents an aspect of constitution of complex brain network. The local information, such as hubs or modules, indicate the local organization of anatomical or functional regions. The globe information represents the overall efficiency of brain networks, which may show differences due to aging. To further understand age-related cognitive differences, it is important to compare local and global metrics between different age groups.

6.2.5 Statistical analysis

Statistical analysis was performed to quantify interregional correlations for bilateral node regions in both young and older adult groups. Totally 17 pairs of bilateral

regions were compared by the z-values that were transformed from Pearson correlation coefficients (R). In order to further test the hypothesis of between-group differences in the graph metrics, pair-wise t-tests were performed to compare the young and older adults in global efficiency (E_{glob}), shortest path length (L_p), clustering coefficient (C_p), normalized clustering coefficient, (γ), normalized characteristic path length (λ) and small-world coefficient (σ). A criterion of $p < 0.05$ was selected.

6.3 Results

6.3.1 Mapping of nodes and edges

The nodes and edges from one young subject are computed by the graph-based atlas-DOT method and are demonstrated in Figure 6-5. As indicated before, colors of nodes represent different brain anatomical regions, while colors of edges represent the strength of connections between two nodes. It is noticed that only the nodes in default mode networks (yellow), frontal-parietal networks (light blue) and part of sensorimotor networks (dark blue) are linked by edges. This is because the optical probe (Figure 6-1) used in my study covered only those brain regions. With the depth compensation algorithm, the image reconstruction depth can reach up to 3 to 4 cm. So the field of view of atlas-DOT image was selected from the surface of the scalp to 4 cm depth into the cortical regions. Then, temporal profiles of cortical nodes (such as superior frontal gyrus) were computed. It is observed that strong connections (light color edges, e.g., yellow and green) are presented in the default mode network (yellow). This finding is consistent with a previous study, which reports that the default mode network is highly involved during the resting-state [189].

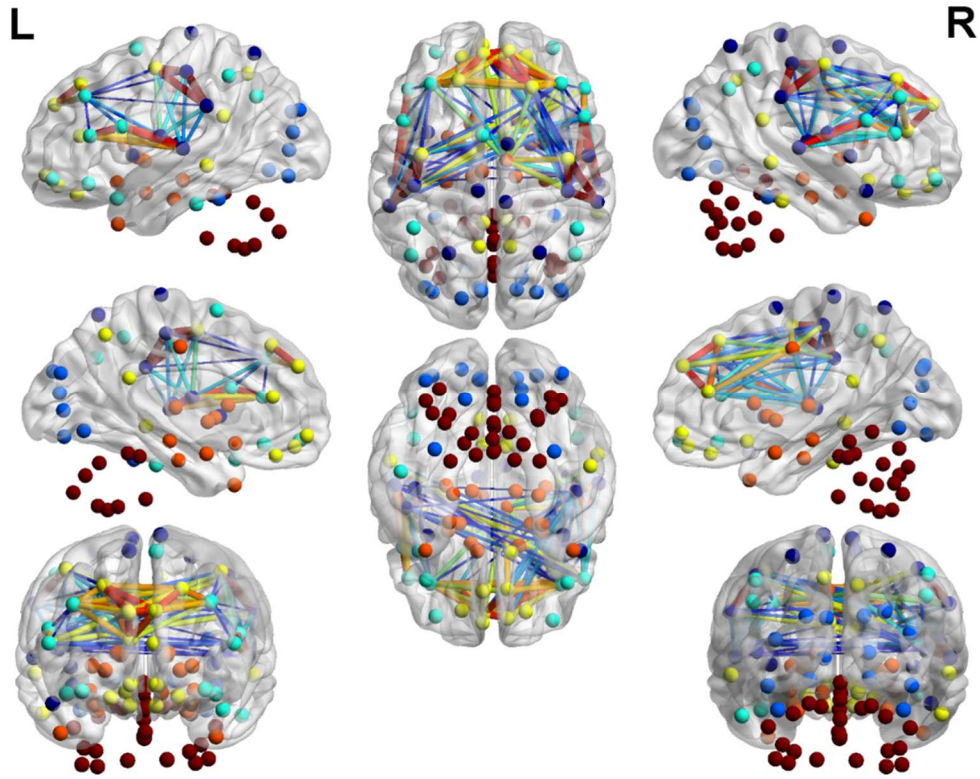


Figure 6-4 Eight views of nodes and edges from subject 1 (in young adult group). Colors of nodes represent the different brain anatomical regions, while colors of edges represent the strength of connections between two nodes.

6.3.2 Global and small-world metrics in brain network

6.3.2.1 Global network metrics

Global efficiency (E_{glob}), clustering coefficient (C_p) and shortest path length (L_p) for both young and older adult group are presented in Figure 6-5. As indicated in Figure 6-5 (a), global efficiencies for young adults are significantly larger than older adults under the sparsity range from 0.08 to 0.38. In contrast, older adults show a significantly larger clustering coefficient from the sparsity range between 0.03 to 0.5 (Figure 6-5(b)). Meanwhile, no significant difference is observed in shortest path length (Figure 6-5(c)). My findings are consistent with a previous study [164], which investigated resting-state

brain networks in 115 young adults (average age = 35) and 110 older adults (average age = 54) using PET. It suggests a decline of global efficiency with an increase of path length as people age [164].

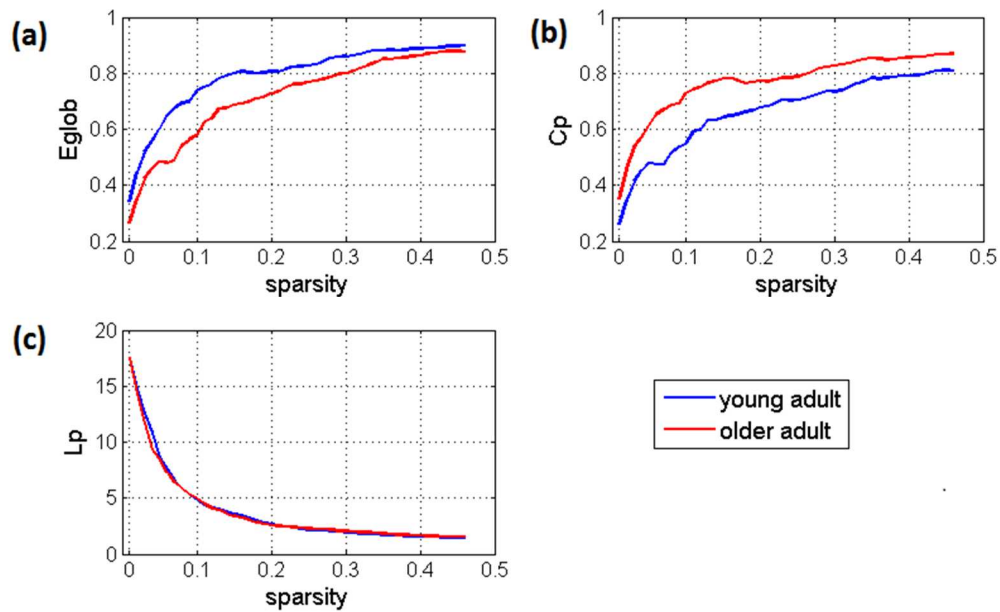


Figure 6-5 Comparison of young and older adult group in global network metrics. The plot for (a) global efficiency; (b) clustering coefficient and (c) shortest path length with respect to the sparsity from 0.05 to 0.5.

6.3.2.2 Small-world functional network

It is demonstrated that functional networks of the human brain have the small-world characteristics [166], [190]. Compared to random networks, the small-world characteristics in the human brain include large local connectivity and an approximately identical shortest path length between any of two nodes in the network. In my study, small-world parameters are quantified in both young adult and older adult groups in the sparsity range from 0.05 to 0.5. Figure 6-6 demonstrates the normalized clustering coefficient (γ), normalized characteristic path length (λ) and small-worldness (σ) of young

adult (blue) and older adult group (red). As observed in Figure 6-6 (b), the normalized characteristic path lengths (λ) in both groups approach to 1 ($0.1 < S < 0.5$), and so do normalized clustering coefficients (γ) ($0.1 < S < 0.5$). These findings on the small-world features in both groups are consistent with a previous report [164]. Specifically, my results show that the normalized characteristic path lengths (λ) are significantly larger in young adults than older adults over a wide range of sparsity ($0.15 < S < 0.5$). However, no significant difference is observed in normalized clustering coefficient (γ) and small-worldness (σ) between the two groups (Figure 6-6(a, c)).

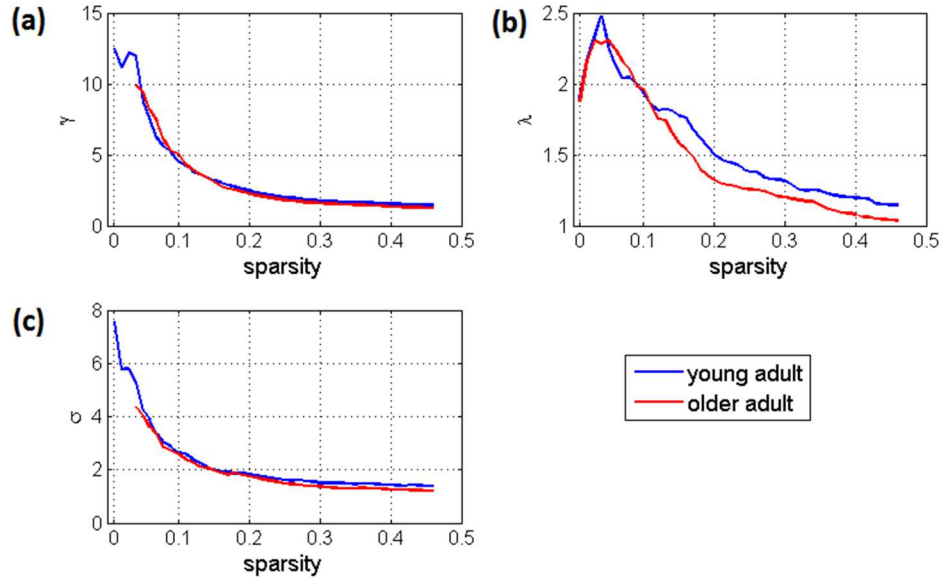


Figure 6-6 Small-world parameters, namely (a) normalized clustering coefficient (γ), (b) normalized characteristic path length (λ) and (c) small-worldness (σ) of young adult (blue) and older adult group (red).

6.3.3 Network hubs

Network hubs were quantified by three nodal parameters, namely, nodal degree (N_i), nodal efficiency (E_{nod}) and betweenness centrality (N_{bc}). First, nodal metrics were

constricted at a sparsity threshold of 0.4 to investigate local features of each node in the two age groups. The hubs were then selected for each of the three nodal parameters (i.e., N_i , E_{nod} and N_{bc}) with respective values larger than one standard deviation of the corresponding average values over all nodes, respectively. As shown in Figure 6-7, hubs are plotted in top view for both young and older adults under three nodal parameters of degree, efficiency and betweenness centrality. In the older adult group, 2, 1 and 3 hubs are found under nodal degree, nodal efficiency and betweenness centrality, respectively. In the young adult group, 5, 4 and 6 hubs are identified. The hub regions in both groups are listed in Table 6-2. The results reveal an overall decline of hub numbers in the aged group. Changes in regional nodal characteristics between two age groups are also denoted. Specifically, hubs in default mode networks are observed only on the right side of the middle frontal gyrus (MFG.R) and the left dorsolateral region of the medial superior frontal gyrus (SFGmed.L) in the older adult group, while both sides of middle frontal gyrus (MFG.L and MFG.R) and the right dorsolateral region (SFGmed.R) are observed in the young adult group. In addition, it is also observed bilateral hubs (MFG.L, MFG.R and SFGmed.L, SFGmed.R) in young adults but mainly unilateral hubs in older adults.

Table 6-2 Regions of hubs in two age groups

Regions	Abbreviations	betweenness	degree	efficiency
Older adult				
Superior frontal gyrus, dorsolateral	SFGdor.R			*
Middle frontal gyrus	MFG.R		*	*
Inferior frontal gyrus, opercular part	IFGtriang.L	*		
Inferior frontal gyrus, opercular part	IFGtriang.R	*		
Superior frontal gyrus, medial	SFGmed.L	*		
Young adult				
Middle frontal gyrus	MFG.L	*	*	*

Table 6-2—*Continued*

Middle frontal gyrus	MFG.R	*		*
Rolandic operculum	ROL.R	*	*	*
Superior frontal gyrus, medial	SFGmed.L	*	*	*
Superior frontal gyrus, medial	SFGmed.R	*	*	*
Anterior cingulate and paracingulate gyri	ACG.R	*		

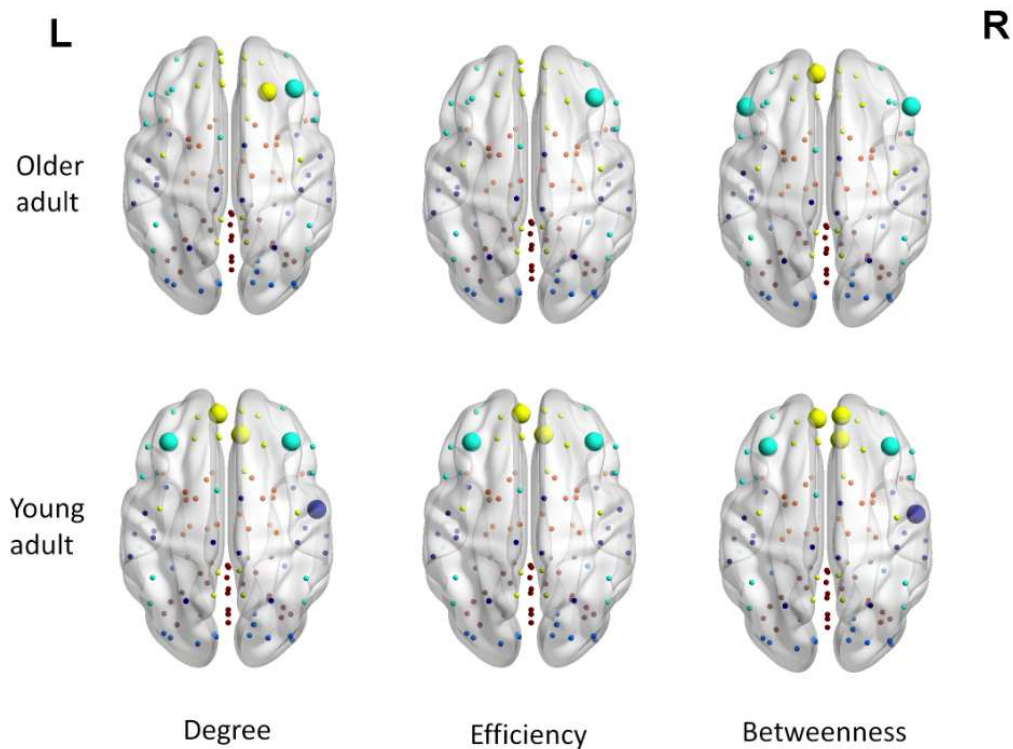


Figure 6-7 Hubs for older adults and young adults. The hubs are grouped as nodal degree, nodal efficiency and betweenness centrality. Yellow represents the default mode network, light blue represents the frontal-parietal network, and dark blue represents the sensorimotor network.

6.4 Discussion

This chapter firstly introduces graph theory analysis in atlas-DOT and investigates age-related changes in brain network parameters by comparing graph theory

metrics between 15 young adults and 21 older adults. The major findings in this chapter are as follows. First, the network metrics in global integration indicate an overall larger brain efficiency in young adults. Meanwhile, older adults reveal higher clustering network features than young adults. Second, both age groups show small-world features which reveal the nature of human brain organizations. However, no significant difference is found in small-worldness between young and older adult group. Third, nodal characteristics are observed difference between two age groups. Older adults showed a decreased hubs numbers than young adults. In addition, the hub regions are changed between two groups, especially in DMN. Overall, consistent findings are observed compared to previous studies reported by others.

6.4.1 Graph formation in atlas-DOT

This study combines the atlas-DOT approach with the network formation, which is an important step in GTA-based image analysis development since different image techniques utilize different approaches to define their network formations. Specifically, formations of networks by fMRI and PET are either by choosing pre-designed models (such as AAL) as node regions or defining all the brain voxels as nodes [164], [167]. In addition, no report on applying graph theory to fNIRS brain image data had been found until 2012. Recent fNIRS-based studies performed by Niu et al. utilized a total of 46 channels and investigated the large-scale, whole-brain network properties in twenty one health young adults [68], [109], [177]. Their results suggest that the fNIRS technique be reliable and feasible for resting-state brain network studies. Differently, my study applies a 3D-reconstruction technique for the network formation. The primary differences between my study and previous channel-wise studies are the application or implementation of three-dimensional reconstruction algorithm with the depth compensation approach, where DOT-based reconstruction is computed using a pre-

developed finite-element brain atlas [43], [105], [191]. This method reveals the feasibility of converting scalp-based optical measures to voxel-based cortical information. So far, few similar report has been found on combining DOT and GTA to study cortical brain networks. However, the optical probe used in my study covered only the frontal part of the brain. With the depth compensation algorithm, the trustable or reliable ROD is $12 \times 20 \times 4$ cm, where only approximate 1/5 (36525 over 179162) of total brain voxels are covered. Node extraction from this region shows that only 34 nodes (out of 116) are associated. Further study is suggested to increase the number of channels to cover the whole cortical regions, and thus this atlas-guided DOT approach could maximize its utilization.

6.4.2 Global integration and small-world features in two age groups

In this chapter, default mode networks and frontal-parietal networks of young adults (25-43 years of age) and older adults (65-92 years of age) have been studied. Our findings of high global efficiency in young adults and low in older adults are consistent with previous studies [162]–[164], [166]. The observation that young adults show a range of global efficiency larger than older adults in prefrontal regions could possibly due to anatomical changes along aging. It is reported that age-related decline of gray matter density happens firstly in the frontal cortex and then spreads through the entire brain [9]. Thus, the significant decrease of global efficiency in frontal regions in older adults could be associated with the rapid decline of gray matter density (GMD) after age of 65. My results also reveal that the clustering coefficient is larger in older adults than young adults. This finding is also consistent with previous reports [187], [164]. The observation of increased cluster (or module) numbers and decreased global and local efficiency in the prefrontal region of older adults reveals a possible reorganization of frontal network as people age. A similar study that investigated 11 older adults and 15 young adults using

fMRI indicates that the information processes are less economical in older adults, especially in frontal and temporal cortical and subcortical regions [187]. Several other reports also suggest an increase of shortest path length with an increase in age. This is due to the loss of long distant connection and interconnected hubs [168], [174]. However, there is no significant difference in those network metrics observed in my study. A possible reason could be a limited brain region (i.e., prefrontal) covered by the optical probe, thus leading to exclusion of long distant brain networks.

The data from both age groups have revealed a small-world characteristic in the frontal brain networks. As indicated by Sporn et al., small-world features of brain networks are due to an optimal balance between global integration and local specialization [192], [193]. A small-world network is formed by the process of brain network development and growth, which evolves for high complexity of dynamic behaviors. my findings are consistent with previous studies, which suggest that the human brain behaves like a complex organization that is neither entirely random nor entirely regular [24], [164], [190]. However, there is no significant difference in small-worldness observed between young and older adults in my study. Possible reasons could be again due to the partial coverage of the brain/cortical regions by the optical probe in my study.

6.4.3 Node betweenness centrality and age-related changes

The hubs or pivotal nodes are quantified by nodal degree, nodal efficiency and betweenness centrality in both age groups. Specifically, betweenness centrality is one of the crucial parameters that helps us identify important nodes within a network. The human brain has a small-world character, which an indicator of existence of local pivotal node regions that are efficiently connected to other parts of brain networks. My findings in both age groups show several identified hubs of the brain networks being located in the

frontal cortical regions. This finding is similar to the previous findings [192], [193].

Meanwhile, the alterations of hubs are observed between young and older adults. Figure 6-7 and Table 6-2 reveal a decrease of hub numbers from young adults to older adults. Especially, the nodal betweenness in DMN regions (such as MFG.L and SFGmed.L) are diminished in the older adults. It has been suggested that cortical regions instead of other parts of the brain (e.g., white matter) are tend to host hubs. The decrease of frontal region efficiency could possibly lead to the reduction of hubs in the frontal region of DMN. Another possible reason for the decline in betweenness of nodes in the frontal DMN in older adults could be due to possible amyloid deposition in the frontal cortex region. Researchers who have investigated DMN of patients with Alzheimer's disease (AD) suggest that the integrity of DMN may provide a biomarker of AD [194]. In addition, a clinical work on normal older adults indicates the correlation between amyloid deposition with the baseline activity in medial prefrontal cortices [195].

6.5 Summary

This chapter combines the graph theory analysis with atlas-guided DOT. The resting-state spatial-temporal brain images are obtained, and the prefrontal cortex graph theory metrics are compared in order to assess the prefrontal network differences between young and older adults. Innovations of my study in this chapter are: (a) volumetric DOT enables voxel-wise graph formations on the cerebral cortex instead of on the scalp; (b) age-dependent prefrontal network changes are analyzed, leading to a good agreement of my study with reports from previous PET studies. My results report the small-worldness features in both age groups, revealing the nature of brain organizations. It is also observed reduction of global efficiencies in older adults, which is consistent with previous studies. In addition, My findings indicate the reduction of network hubs in frontal regions for older adults, which is suggested to be mainly affected by gray matter decay

during aging process. To sum up, this chapter reveals the feasibility of atlas-guided DOT in assessment of age-related brain network changes at resting state. Further studies using the atlas-DOT technique is suggested to measure/record whole cortical regions, to be able to include and account for long-distance brain connections.

Chapter 7

Summary and Future Work

7.1 Summary

This dissertation focuses on the development of atlas-guided DOT to investigate age-related brain responses under a risk decision-making protocol, BART. The objectives of this dissertation are:

- i. to develop FEM-based atlas-guided DPT with a depth compensation algorithm;
- ii. to implement a general linear model with atlas-DOT to assess the neural correlate of age- and gender- effect on human risk decision-making process.
- iii. to implement a graph theory method with the atlas-DOT approach to assess resting-state brain network changes under age effect. My study utilized atlas-guided, volumetric DOT to analyze the fNIRS data and perform cortical network formations.

To accomplish these goals, the strategies of this dissertation are stated as follows:

(1) I have developed a ICBM152 4-layered human brain template using the finite element method. This template has been built into the forward model to generate a voxel-wise optical sensitivity volume matrix. This volume matrix is then implemented into an inverse problem combined with a depth compensation algorithm. This is the basis of atlas-DOT. A risk decision-making stimulation using BART indicates that atlas-DOT significantly improves reconstruction accuracy and depth information of DOT images.

(2) The GLM has been implemented into atlas-DOT in order to reduce possible subjective variation or to accurately identify brain activation regions with a statistical

power in DOT data/image processing. The GLM is a model driven approach that utilizes pre-designed regressors to fit for hemodynamic time sequence changes. Specifically, this method in my study is capable to separate out the decision-making phase and outcome phase and to lead to statistically significant results. Also, utilizing GLM analysis with atlas-DOT noticeably improves the image reconstruction depth in human-subject measurements. My results also reveal the capacity of this framework to distinguish brain activations from mixed designed sessions during multi-functional cognitive tasks.

(3) In order to better understand the age effect on risk decision-making process, GTA is implemented with atlas-DOT. The voxel-wise nodal extraction is applied in the network formation step. The connectome between anatomical regions of the brain is assessed. My preliminary results of graph theory analysis indicate small-world properties from both age groups and are consistent with previous studies reported by other groups. The nodal analysis also shows alterations of hubs due to aging. Those findings reveal the feasibility of using GTA along with atlas-DOT for assessment of age effect under risk decision making.

In general, the potential impact of this study includes: (1) the FEM-based atlas-DOT can be utilized to enhance reconstructed brain function images in following aspects: (a) it improves image resolution by providing pixel-wise data analysis; (b) it improves depth localization accuracy by integrating the depth compensation algorithm; (c) it improves reconstruction accuracy by specifically assigning layered tissue optical properties. (2) The investigation of brain responses to BART by GLM-based atlas-guided DOT could lead to a better understanding of age-related brain functional changes in the PFC region. (3) The implementation of graph theory method can be potentially useful for extending fNIRS-driven hemodynamic studies towards brain network research.

7.2 Limitations and future work

Compared with other noninvasive neuro-image modalities such as fMRI or MEG, fNIRS has the advantage of fast data acquisition with more flexibility for body movement-involved protocols. However, there are still several limitations with this method:

(1) The imaging depth for fNIRS is limited by the intrinsic optical property. It is shown that the maximum near-infrared light penetration depth in the human brain is 30 to 40 mm [131], [161]. Thus, the activations in the deep brain are unable to be detected by fNIRS tools. Thus, applications or studies using fNIRS should focus mainly on the cortex regions.

(2) The optical probe used in this study only covered prefrontal regions. Since the brain is a complex system with small-world properties, long-distance connections in the brain network are equally important. Future work is suggested to increase the optical fibers to cover the whole brain or cortical regions so that both local features and global information could be obtained.

(3) Aging effect is a continuous process. This study extensively investigated two aged groups (young adults, from 25-43 years of age; older adults, from 65-93 years of age). However, previous studies indicate other critical age periods with rapid brain anatomical and chemical changes; those age groups include youth (7-15 years of age), adolescents (15-24 years of age), and mid age (45-60 years of age). Each of the age groups has its significant development and reorganization in brain networks and physical structures. So it is suggested to include other age groups to completely and comprehensively investigate the age effect under risk decision making in the future work.

(4) There could be other issues that may confound the fNIRS results. Recent studies indicate that an extra-cranial signal could change the measurement of brain signals [88], [90], [91]. Individual variation in scalp-to-cortex distance may confound

results of fNIRS measurement. Moreover, the existence of neural response variability, for instance, the neurophysiological noise, could influence the brain activation measurement under an emotion stimulus [90]. Future work of fNIRS-based research should consider this issue. One quick approach to effectively reduce signal contamination from superficial layers is to add short-distance channels to regress out the extra-cranial noise from cortical regions of the brain [91].

Appendix A
Additional Figures for Chapter 2

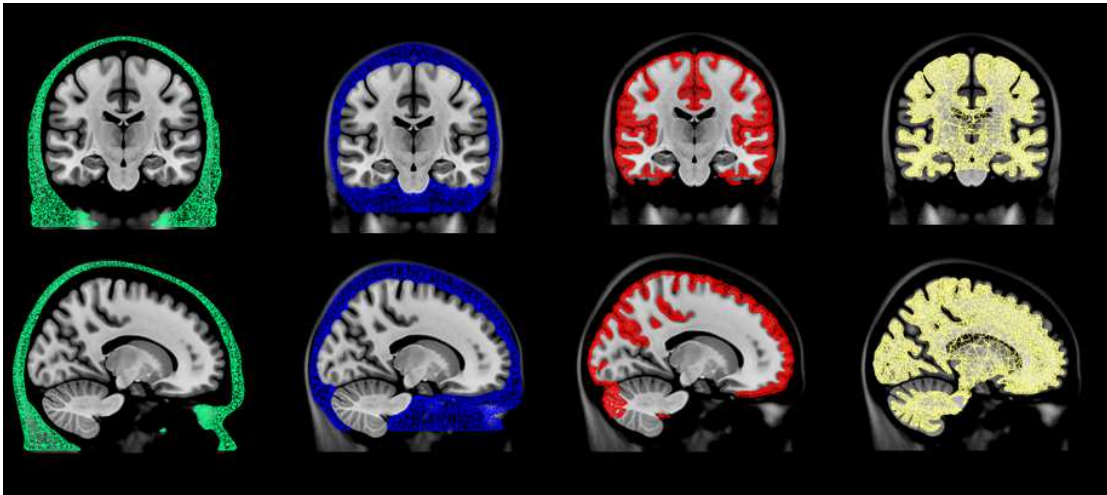


Figure 1. Coronal and Sagittal views of volume mesh generation for scalp(green), skull (blue), gray matter (red) and white matter (yellow).

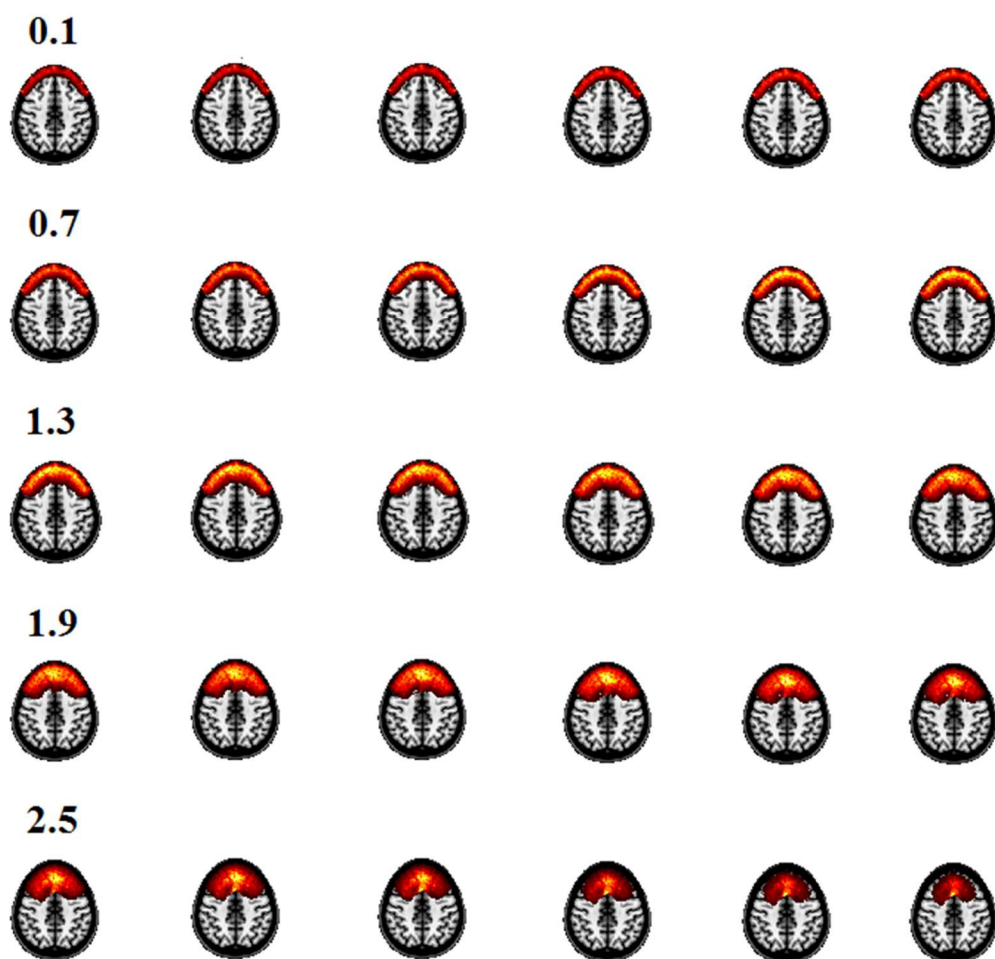


Figure 2. Axial view of the sensitivity matrix after depth compensation algorithm. The sensitivity matrices represent the forward calculation results by using the depth compensation factor $\gamma = 0.1$ to $\gamma = 3.0$.

Appendix B

Derivation of the Six Forms of ICC in Chapter 3

ICC(1,1) and ICC(1,k):

For the one-way random-effect model, according to the expressions of EMS

terms in Table 3-4, the variances can be estimated by

$$\begin{aligned}\sigma_e^2 &= MS_W \\ \sigma_s^2 &= \frac{MS_B - MS_W}{k}\end{aligned}\tag{a1}$$

Following the definition of reliability in Eq. (3-11), the ICC of a single measurement is

$$\begin{aligned}ICC(1,1) &= \frac{\sigma_s^2}{\sigma_s^2 + \sigma_e^2} \\ &= \frac{\frac{MS_B - MS_W}{k}}{\frac{MS_B - MS_W}{k} + MS_W} \\ &= \frac{MS_B - MS_W}{MS_B + (k-1)MS_W}\end{aligned}\tag{a2}$$

When the single measurement is replaced by the average measurement, the random error variance will be divided by k . Consequently, the ICC of the average measurement is

$$\begin{aligned}ICC(1,k) &= \frac{\sigma_s^2}{\sigma_s^2 + \sigma_e^2 / k} \\ &= \frac{\frac{MS_B - MS_W}{k}}{\frac{MS_B - MS_W}{k} + \frac{MS_W}{k}} \\ &= \frac{MS_B - MS_W}{MS_B}\end{aligned}\tag{a3}$$

ICC(2,1) and ICC(2,k):

In the two-way random-effect model, the total variance is decomposed into three components: between-subjects variance, between-tests variance and random error variance, which can be estimated by:

$$\begin{aligned}\sigma_e^2 &= MS_E \\ \sigma_S^2 &= \frac{MS_B - MS_E}{k} \\ \sigma_T^2 &= \frac{MS_T - MS_E}{n}\end{aligned}\tag{a4}$$

Following the definition in Eq. (3-10), the ICC of a single measurement is

$$\begin{aligned}ICC(2,1) &= \frac{\sigma_S^2}{\sigma_S^2 + \sigma_T^2 + \sigma_e^2} \\ &= \frac{\frac{MS_B - MS_E}{k}}{\frac{MS_B - MS_E}{k} + \frac{TMS - MS_E}{n} + MS_E} \\ &= \frac{MS_B - MS_E}{MS_B + (k-1)MS_E + k(TMS - MS_E)/n}\end{aligned}\tag{a5}$$

When the average measurement is used, the between-tests variance and random error variance will be divided by k , giving

$$\begin{aligned}ICC(2,k) &= \frac{\sigma_S^2}{\sigma_S^2 + (\sigma_T^2 + \sigma_e^2)/k} \\ &= \frac{\frac{MS_B - MS_E}{k}}{\frac{MS_B - MS_E}{k} + \frac{MS_T - MS_E}{nk} + \frac{MS_E}{k}} \\ &= \frac{MS_B - MS_E}{MS_B + (MS_T - MS_E)/n}\end{aligned}\tag{a6}$$

ICC(3,1) and ICC(3,k):

In the two-way mixed-effect model, the total variance is decomposed into three components like in the two-way random-effect model, and the variances of the random factors can be estimated by

$$\begin{aligned}\sigma_e^2 &= MS_E \\ \sigma_S^2 &= \frac{MS_B - MS_E}{k}\end{aligned}\tag{a7}$$

Since there is no variance of the factor “Test”, definition (7) will be followed, giving

$$\begin{aligned}ICC(3, 1) &= \frac{\sigma_S^2}{\sigma_S^2 + \sigma_e^2} \\ &= \frac{MS_B - MS_E}{MS_B + (k-1)MS_E}\end{aligned}\tag{a8}$$

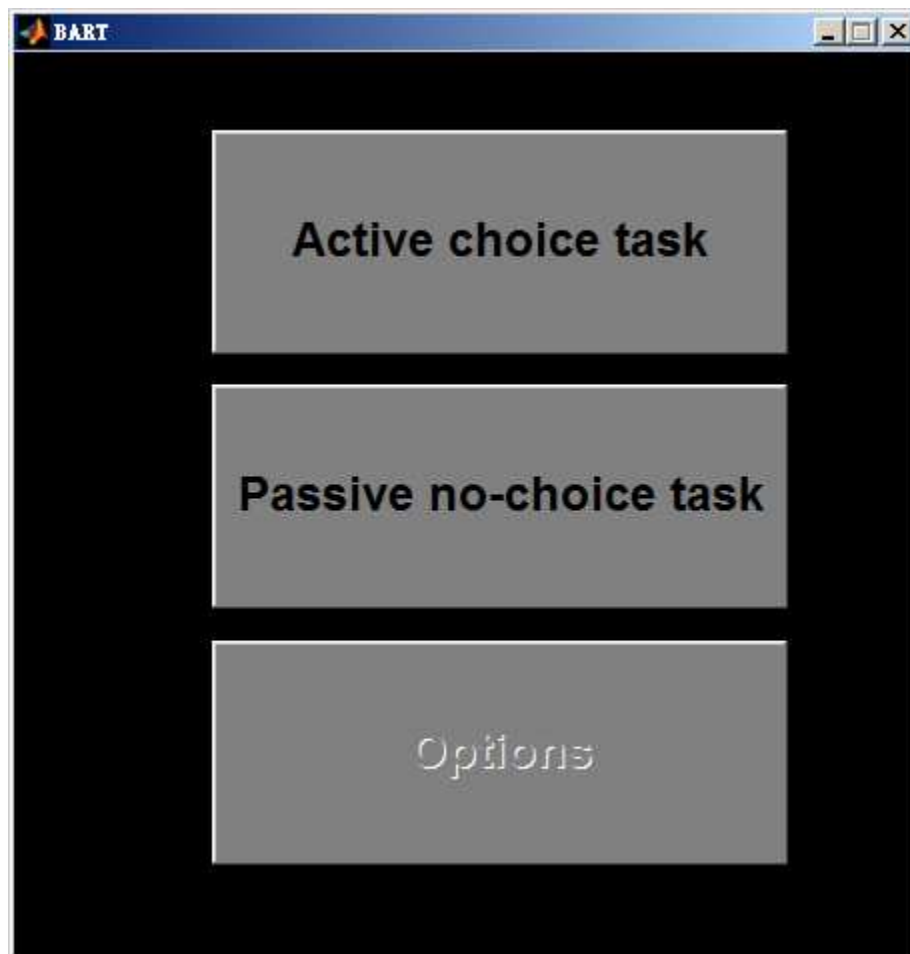
When the average measurement is used, the random error variance will be divided by k . So

$$\begin{aligned}ICC(3, k) &= \frac{\sigma_S^2}{\sigma_S^2 + \sigma_e^2 / k} \\ &= \frac{MS_B - MS_E}{MS_B + (k-1)MS_E / k}\end{aligned}\tag{a9}$$

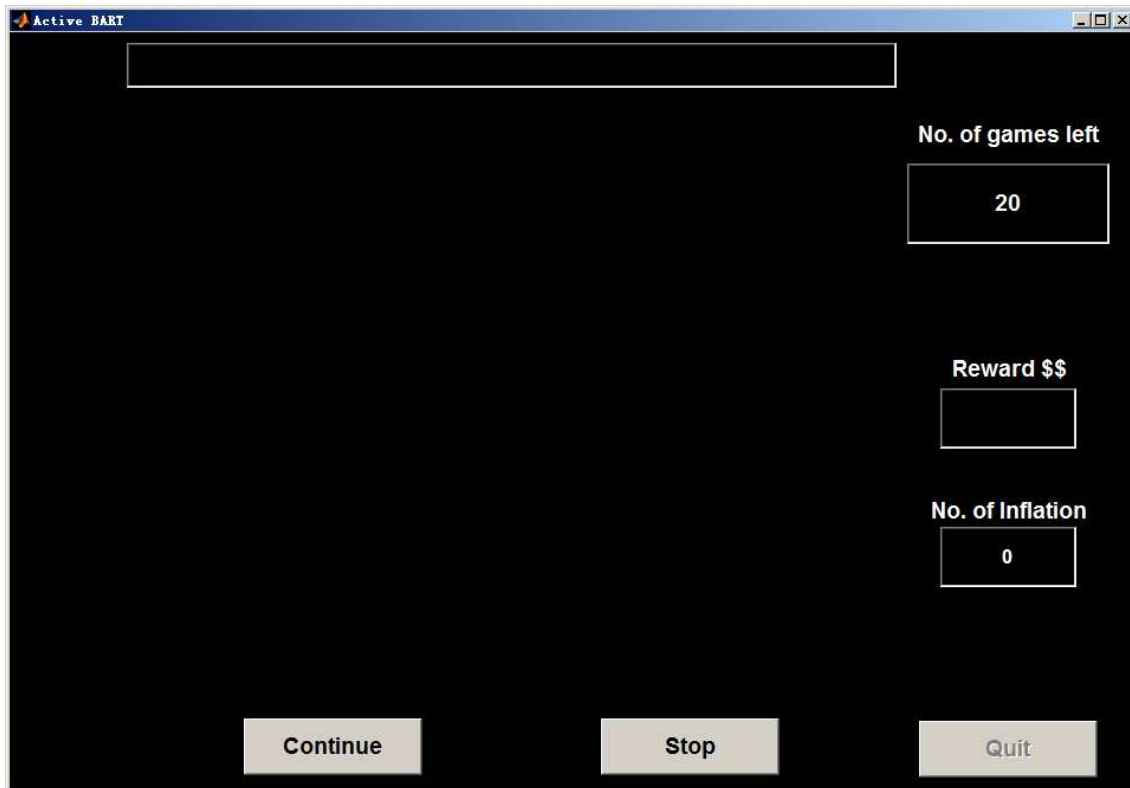
Appendix C

Matlab Program for BART Protocol

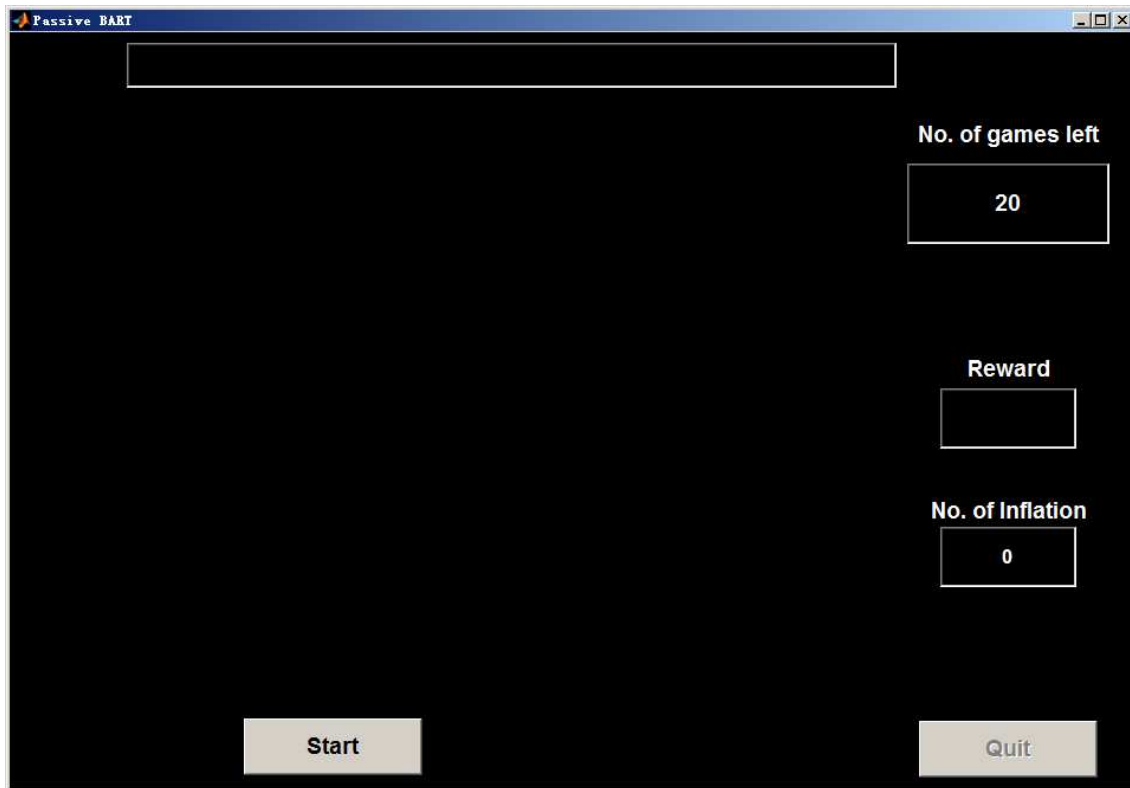
Images and Matlab Graphical User Interface of the BART protocol.



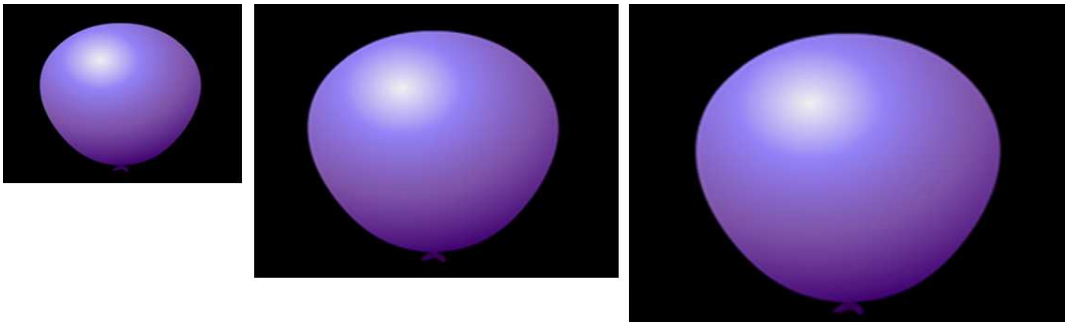
Graphical User Interface (GUI) of the BART protocol in the Main manual.



Graphical User Interface (GUI) of the BART protocol in the active task.



Graphical User Interface (GUI) of the BART protocol in the passive task.



Balloons and outcome pictures used in BART protocol.

Matlab code main.m:

```
function varargout = main(varargin)
% MAIN M-file for main.fig
%     MAIN, by itself, creates a new MAIN or raises the existing
%     singleton*.
%
%     H = MAIN returns the handle to a new MAIN or the handle to
%     the existing singleton*.
%
%     MAIN('CALLBACK',hObject,eventData,handles,...) calls the local
%     function named CALLBACK in MAIN.M with the given input arguments.
%
%     MAIN('Property','Value',...) creates a new MAIN or raises the
%     existing singleton*. Starting from the left, property value pairs are
%     applied to the GUI before main_OpeningFcn gets called. An
%     unrecognized property name or invalid value makes property application
%     stop. All inputs are passed to main_OpeningFcn via varargin.
%
%     *See GUI Options on GUIDE's Tools menu. Choose "GUI allows only one
%     instance to run (singleton)".
%
% See also: GUIDE, GUIDATA, GUIHANDLES

% Edit the above text to modify the response to help main

% Last Modified by GUIDE v2.5 21-Mar-2011 14:17:03

% Begin initialization code - DO NOT EDIT
gui_Singleton = 1;
gui_State = struct('gui_Name',       mfilename, ...
                  'gui_Singleton',   gui_Singleton, ...
                  'gui_OpeningFcn',  @main_OpeningFcn, ...
                  'gui_OutputFcn',   @main_OutputFcn, ...
                  'gui_LayoutFcn',   [] , ...
                  'gui_Callback',    []);
if nargin && ischar(varargin{1})
    gui_State.gui_Callback = str2func(varargin{1});
end

if nargout
    [varargout{1:nargout}] = gui_mainfcn(gui_State, varargin{:});
else
    gui_mainfcn(gui_State, varargin{:});
end
% End initialization code - DO NOT EDIT
% --- Executes just before main is made visible.
function main_OpeningFcn(hObject, eventdata, handles, varargin)
% This function has no output args, see OutputFcn.
% hObject    handle to figure
% eventdata  reserved - to be defined in a future version of MATLAB
% handles     structure with handles and user data (see GUIDATA)
```



```

% varargin    command line arguments to main (see VARARGIN)
% Choose default command line output for main
handles.output = hObject;
% Update handles structure
guidata(hObject, handles);
% UIWAIT makes main wait for user response (see UIRESUME)
% uiwait(handles.figure1);

% --- Outputs from this function are returned to the command line.
function varargout = main_OutputFcn(hObject, eventdata, handles)
% varargout    cell array for returning output args (see VARARGOUT);
% hObject      handle to figure
% eventdata    reserved - to be defined in a future version of MATLAB
% handles      structure with handles and user data (see GUIDATA)
% Get default command line output from handles structure
varargout{1} = handles.output;

% --- Executes on button press in BTN_active.
function BTN_active_Callback(hObject, eventdata, handles)
% hObject      handle to BTN_active (see GCBO)
% eventdata    reserved - to be defined in a future version of MATLAB
% handles      structure with handles and user data (see GUIDATA)
active;
guidata(hObject, handles);

% --- Executes on button press in BTN_passive.
function BTN_passive_Callback(hObject, eventdata, handles)
% hObject      handle to BTN_passive (see GCBO)
% eventdata    reserved - to be defined in a future version of MATLAB
% handles      structure with handles and user data (see GUIDATA)
passive;
guidata(hObject, handles);

% --- Executes on button press in BTN_option.
function BTN_option_Callback(hObject, eventdata, handles)
% hObject      handle to BTN_option (see GCBO)
% eventdata    reserved - to be defined in a future version of MATLAB
% handles      structure with handles and user data (see GUIDATA)

```

Matlab code active.m:

```
% BART protocol code
function varargout = active(varargin)
% ACTIVE M-file for active.fig
%     ACTIVE, by itself, creates a new ACTIVE or raises the existing
%     singleton*.
%
%     H = ACTIVE returns the handle to a new ACTIVE or the handle to
%     the existing singleton*.
%
%     ACTIVE('CALLBACK',hObject,eventData,handles,...) calls the local
%     function named CALLBACK in ACTIVE.M with the given input arguments.
%
%     ACTIVE('Property','Value',...) creates a new ACTIVE or raises the
%     existing singleton*. Starting from the left, property value pairs are
%     applied to the GUI before active_OpeningFcn gets called. An
%     unrecognized property name or invalid value makes property application
%     stop. All inputs are passed to active_OpeningFcn via varargin.
%
%     *See GUI Options on GUIDE's Tools menu. Choose "GUI allows only one
%     instance to run (singleton)".
%
% See also: GUIDE, GUIDATA, GUIHANDLES
% Edit the above text to modify the response to help active
% Last Modified by GUIDE v2.5 21-Mar-2011 16:04:17
% Begin initialization code - DO NOT EDIT
gui_Singleton = 1;
gui_State = struct('gui_Name',       mfilename, ...
                  'gui_Singleton',   gui_Singleton, ...
                  'gui_OpeningFcn', @active_OpeningFcn, ...
                  'gui_OutputFcn',  @active_OutputFcn, ...
                  'gui_LayoutFcn',   [] , ...
                  'gui_Callback',    []);
if nargin && ischar(varargin{1})
    gui_State.gui_Callback = str2func(varargin{1});
end

if nargout
    [varargout{1:nargout}] = gui_mainfcn(gui_State, varargin{:});
else
    gui_mainfcn(gui_State, varargin{:});
end
% End initialization code - DO NOT EDIT
% --- Executes just before active is made visible.
function active_OpeningFcn(hObject, eventdata, handles, varargin)
% This function has no output args, see OutputFcn.
% hObject    handle to figure
% eventdata  reserved - to be defined in a future version of MATLAB
% handles    structure with handles and user data (see GUIDATA)
% varargin   command line arguments to active (see VARARGIN)
```

```

% Choose default command line output for active
handles.output = hObject;
% %t = timer('TimerFcn', 'stat=false; disp("Timer!")',...
%           'StartDelay',10);
% start(t)
% stat=true;
% while(stat==true)
%     pause(1)
% end
filename = [cd 'bmp\bb01.jpg'];
handles.img = imread(filename);
[handles.r,handles.c] = size(handles.img);
handles.axes_p = get(handles.axes1,'Position');
handles.axes_cx = handles.axes_p(1) + handles.axes_p(3)/2;
handles.axes_cy = handles.axes_p(2) + handles.axes_p(4)/2;
handles.f_p = get(handles.figure1,'Position');
handles.c = handles.c / handles.f_p(3);
handles.r = handles.r / handles.f_p(4);
handles.c_x = handles.c / 2;
handles.c_y = handles.r / 2;
set(handles.axes1,'Position',[handles.axes_cx-handles.c_x handles.axes_cy-handles.c_y
handles.c handles.r]);
imshow(handles.img,'InitialMagnification',110);
handles.time = 1;
handles.reward = 0;
handles.mgv = 100;
handles.gameleft = 20;
set(handles.EDT_inflation,'String',num2str(0));
handles.r_e = [0 2.1 4.2 6.3 14.6 23.9 31.3 43.8 56.3 68.8 79.2 89.6];
handles.Wager = [0 0.05 0.15 0.25 0.55 0.95 1.45 2.05 2.75 3.45 4.25 5.15];
guidata(hObject, handles);

% UIWAIT makes active wait for user response (see UIRESUME)
% uiwait(handles.figure1);
% --- Outputs from this function are returned to the command line.
function varargout = active_OutputFcn(hObject, eventdata, handles)
% varargout    cell array for returning output args (see VARARGOUT);
% hObject      handle to figure
% eventdata    reserved - to be defined in a future version of MATLAB
% handles      structure with handles and user data (see GUIDATA)

% Get default command line output from handles structure
varargout{1} = handles.output;

function EDT_reward_Callback(hObject, eventdata, handles)
% hObject      handle to EDT_reward (see GCBO)
% eventdata    reserved - to be defined in a future version of MATLAB
% handles      structure with handles and user data (see GUIDATA)

% Hints: get(hObject,'String') returns contents of EDT_reward as text
%         str2double(get(hObject,'String')) returns contents of EDT_reward as a double

```

```

% --- Executes during object creation, after setting all properties.
function EDT_reward_CreateFcn(hObject, eventdata, handles)
% hObject    handle to EDT_reward (see GCBO)
% eventdata  reserved - to be defined in a future version of MATLAB
% handles    empty - handles not created until after all CreateFcns called
% Hint: edit controls usually have a white background on Windows.
%         See ISPC and COMPUTER.
if ispc && isequal(get(hObject,'BackgroundColor'), get(0,'defaultUicontrolBackgroundColor'))
    set(hObject,'BackgroundColor','white');
end

function EDT_inflation_Callback(hObject, eventdata, handles)
% hObject    handle to EDT_inflation (see GCBO)
% eventdata  reserved - to be defined in a future version of MATLAB
% handles    structure with handles and user data (see GUIDATA)
% Hints: get(hObject,'String') returns contents of EDT_inflation as text
%        str2double(get(hObject,'String')) returns contents of EDT_inflation as a double

% --- Executes during object creation, after setting all properties.
function EDT_inflation_CreateFcn(hObject, eventdata, handles)
% hObject    handle to EDT_inflation (see GCBO)
% eventdata  reserved - to be defined in a future version of MATLAB
% handles    empty - handles not created until after all CreateFcns called
% Hint: edit controls usually have a white background on Windows.
%         See ISPC and COMPUTER.
if ispc && isequal(get(hObject,'BackgroundColor'), get(0,'defaultUicontrolBackgroundColor'))
    set(hObject,'BackgroundColor','white');
end

% --- Executes on button press in BTN_cont.
function BTN_cont_Callback(hObject, eventdata, handles)
% hObject    handle to BTN_cont (see GCBO)
% eventdata  reserved - to be defined in a future version of MATLAB
% handles    structure with handles and user data (see GUIDATA)
% Use t1 and t2 to calculate the time played per balloon.
% at the beginning, t1 = clock, shows the beginning time while playing;
% when the balloon is finished, t2 = clock, shows the ending time played;
% then t2-t1 is the time played.
% c = clock returns a 6-element date vector containing the current date and time in decimal
form:
% [year month day hour minute seconds] for example [2012,5,28,18,17,19.978000000000000];
if handles.time - 1 == 0;
    handles.t1 = clock;
end
handles.reward_temp = 0;
if handles.time < 13
    idx = 100*rand(1);
    if idx <= handles.r_e(handles.time)
        handles.reward_temp = 0;
        [y, Fs] = wavread([cd '\bmp\explode.wav']);
        player = audioplayer(y, Fs);
        play(player);
    end
end

```

```

handles.t2 = clock;
handles.playtime(21 - handles.gameleft) = (handles.t2(4) - handles.t1(4))*60^2 +
(handles.t2(5) - handles.t1(5))*60 + handles.t2(6) - handles.t1(6);

set(handles.EDT_inflation,'String',num2str(handles.time));
set(handles.EDT_reward,'String',num2str(handles.reward));
set(handles.BTN_cont,'Enable','off');
set(handles.BTN_stop,'Enable','off');
handles.win(21 - handles.gameleft) = 0;
handles.money(21 - handles.gameleft) = 0;
handles.inflation(21 - handles.gameleft) = handles.time;
handles.gameleft = handles.gameleft - 1;
set(handles.axes1,'Position',handles.axes_p);
filename = [cd '\bmp\bb24_b.jpg'];
A = imread(filename);
imshow(A,'InitialMagnification',100);
pause(1);
filename = [cd '\bmp\lose.jpg'];
A = imread(filename);
imshow(A,'InitialMagnification',100);
if handles.gameleft == 0
    pause(15);
    close;
    main;
    return;
else
    set(handles.EDT_gameleft,'String',num2str(handles.gameleft));
end

for i = 1 : 15
    message = ['Next game will begin in ' num2str(16-i) 's'];
    set(handles.EDT_time,'String',message);
    pause(1);
end
    set(handles.EDT_time,'String',[]);
    set(handles.axes1,'Position',[handles.axes_cx - handles.c_x handles.axes_cy -
handles.c_y handles.c handles.r]);
    imshow(handles.img,'InitialMagnification',100);
    handles.time = 1;
    handles.mgv = 100;
    set(handles.EDT_inflation,'String',num2str(0));
    set(handles.EDT_reward,'String',[]);
    set(handles.BTN_cont,'Enable','on');
    set(handles.BTN_stop,'Enable','on');
else
    handles.mgv = handles.mgv + 10;
    nx = handles.c * (handles.mgv/100);
    ny = handles.r * (handles.mgv/100);
    c_x = nx / 2;
    c_y = ny / 2;
    set(handles.axes1,'Position',[handles.axes_cx-c_x handles.axes_cy-c_y nx ny]);

```

```

        imshow(handles.img,'InitialMagnification',handles.mgv);
        handles.reward_temp = handles.reward_temp + handles.Wager(handles.time);
    %         imshow(handles.img,'InitialMagnification',handles.mgv);
    %         handles.reward = handles.reward + handles.Wager(handles.time);
        set(handles.EDT_inflation,'String',num2str(handles.time));
        %set(handles.EDT_reward,'String',num2str(handles.reward));
        handles.time = handles.time + 1;
    end
else
    filename = [cd '\bmp\win.jpg'];
    A = imread(filename);
    set(handles.axes1,'Position',handles.axes_p);
    imshow(A,'InitialMagnification',100);
    handles.reward = handles.reward + handles.Wager(handles.time);
end
guidata(hObject, handles);
% --- Executes on button press in BTN_stop.
function BTN_stop_Callback(hObject, eventdata, handles)
% hObject    handle to BTN_stop (see GCBO)
% eventdata  reserved - to be defined in a future version of MATLAB
% handles    structure with handles and user data (see GUIDATA)
handles.t2 = clock;
handles.playtime(21 - handles.gameleft) = (handles.t2(4) - handles.t1(4))*60^2 + (handles.t2(5) - handles.t1(5))*60 + handles.t2(6) - handles.t1(6);
handles.win(21 - handles.gameleft) = 1;
handles.inflation(21 - handles.gameleft) = handles.time - 1;
set(handles.axes1,'Position',handles.axes_p);
filename = [cd '\bmp\win.jpg'];
A = imread(filename);
imshow(A,'InitialMagnification',100);
set(handles.BTN_cont,'Enable','off');
set(handles.BTN_stop,'Enable','off');
set(handles.EDT_inflation,'String',num2str(handles.time - 1));
handles.reward = handles.reward + handles.reward_temp;
handles.money(21 - handles.gameleft) = handles.reward;
% handles.reward = handles.reward + handles.Wager(handles.time);
set(handles.EDT_reward,'String',num2str(handles.reward));
handles.gameleft = handles.gameleft - 1;
if handles.gameleft == 0
    pause(15);
    close;
    main;
    return;
else
    set(handles.EDT_gameleft,'String',num2str(handles.gameleft));
end
%%%%%%%%%%%%%% cool-
down %%%%%%%%%%%%%%%
for i = 1 : 15
    message = ['Next game will begin in ' num2str(16-i) 's'];
    set(handles.EDT_time,'String',message);
    pause(1);
end

```

```

end
%%%%%%%%%%%%%%%%%%%%%%%%%%%%%%%%%%%%%%%%%%%%%%%%%%%%%%%%%%%%%%%%%%%%%%%%%%%%%%
%%%%%%%%%%%%%%%%%%%%%%%%%%%%%%%%%%%%%%%%%%%%%%%%%%%%%%%%%%%%%%%%%%%%%%%%%%%%%%
set(handles.EDT_time,'String',[]);
set(handles.EDT_reward,'String',[]);
set(handles.axes1,'Position',[handles.axes_cx - handles.c_x handles.axes_cy - handles.c_y
handles.c handles.r]);
imshow(handles.img,'InitialMagnification',100);
handles.time = 1;
handles.mgv = 100;
set(handles.EDT_inflation,'String',num2str(0));
set(handles.BTN_cont,'Enable','on');
set(handles.BTN_stop,'Enable','on');

guidata(hObject, handles);

% --- Executes on button press in BTN_quit.
function BTN_quit_Callback(hObject, eventdata, handles)
% hObject    handle to BTN_quit (see GCBO)
% eventdata  reserved - to be defined in a future version of MATLAB
% handles    structure with handles and user data (see GUIDATA)

% --- Executes on button press in BTN_again.
function BTN_again_Callback(hObject, eventdata, handles)
% hObject    handle to BTN_again (see GCBO)
% eventdata  reserved - to be defined in a future version of MATLAB
% handles    structure with handles and user data (see GUIDATA)

function EDT_time_Callback(hObject, eventdata, handles)
% hObject    handle to EDT_time (see GCBO)
% eventdata  reserved - to be defined in a future version of MATLAB
% handles    structure with handles and user data (see GUIDATA)

% Hints: get(hObject,'String') returns contents of EDT_time as text
%        str2double(get(hObject,'String')) returns contents of EDT_time as a double

% --- Executes during object creation, after setting all properties.
function EDT_time_CreateFcn(hObject, eventdata, handles)
% hObject    handle to EDT_time (see GCBO)
% eventdata  reserved - to be defined in a future version of MATLAB
% handles    empty - handles not created until after all CreateFcns called

% Hint: edit controls usually have a white background on Windows.
%        See ISPC and COMPUTER.
if ispc && isequal(get(hObject,'BackgroundColor'), get(0,'defaultUicontrolBackgroundColor'))
    set(hObject,'BackgroundColor','white');
end

function EDT_gameleft_Callback(hObject, eventdata, handles)
% hObject    handle to EDT_gameleft (see GCBO)

```

```

% eventdata reserved - to be defined in a future version of MATLAB
% handles structure with handles and user data (see GUIDATA)

% Hints: get(hObject,'String') returns contents of EDT_gameleft as text
% str2double(get(hObject,'String')) returns contents of EDT_gameleft as a double

% --- Executes during object creation, after setting all properties.
function EDT_gameleft_CreateFcn(hObject, eventdata, handles)
% hObject handle to EDT_gameleft (see GCBO)
% eventdata reserved - to be defined in a future version of MATLAB
% handles empty - handles not created until after all CreateFcns called

% Hint: edit controls usually have a white background on Windows.
% See ISPC and COMPUTER.
if ispc && isequal(get(hObject,'BackgroundColor'), get(0,'defaultUicontrolBackgroundColor'))
    set(hObject,'BackgroundColor','white');
end

```


Matlab code passive.m

```
function varargout = passive(varargin)
% PASSIVE M-file for passive.fig
%     PASSIVE, by itself, creates a new PASSIVE or raises the existing
%     singleton*.
%
%     H = PASSIVE returns the handle to a new PASSIVE or the handle to
%     the existing singleton*.
%
%     PASSIVE('CALLBACK',hObject,eventData,handles,...) calls the local
%     function named CALLBACK in PASSIVE.M with the given input arguments.
%
%     PASSIVE('Property','Value',...) creates a new PASSIVE or raises the
%     existing singleton*. Starting from the left, property value pairs are
%     applied to the GUI before passive_OpeningFcn gets called. An
%     unrecognized property name or invalid value makes property application
%     stop. All inputs are passed to passive_OpeningFcn via varargin.
%
%     *See GUI Options on GUIDE's Tools menu. Choose "GUI allows only one
%     instance to run (singleton)".
%
% See also: GUIDE, GUIDATA, GUIHANDLES
% Edit the above text to modify the response to help passive
% Last Modified by GUIDE v2.5 21-Mar-2011 17:29:27
% Begin initialization code - DO NOT EDIT
gui_Singleton = 1;
gui_State = struct('gui_Name',       mfilename, ...
    'gui_Singleton',  gui_Singleton, ...
    'gui_OpeningFcn', @passive_OpeningFcn, ...
    'gui_OutputFcn',  @passive_OutputFcn, ...
    'gui_LayoutFcn',  [] , ...
    'gui_Callback',   []);
if nargin && ischar(varargin{1})
    gui_State.gui_Callback = str2func(varargin{1});
end

if nargout
    [varargout{1:nargout}] = gui_mainfcn(gui_State, varargin{:});
else
    gui_mainfcn(gui_State, varargin{:});
end
% End initialization code - DO NOT EDIT

% --- Executes just before passive is made visible.
function passive_OpeningFcn(hObject, eventdata, handles, varargin)
% This function has no output args, see OutputFcn.
% hObject    handle to figure
% eventdata  reserved - to be defined in a future version of MATLAB
% handles    structure with handles and user data (see GUIDATA)
% varargin   command line arguments to passive (see VARARGIN)
```

```

% Choose default command line output for passive
handles.output = hObject;
% %t = timer('TimerFcn', 'stat=false; disp("Timer!")',...
%           'StartDelay',10);
% start(t)
% stat=true;
% while(stat==true)
%     pause(1)
% end
filename = [cd '\bmp\bb01.jpg'];
handles.img = imread(filename);
[handles.r,handles.c handles.d] = size(handles.img);
handles.axes_p = get(handles.axes1,'Position');
handles.axes_cx = handles.axes_p(1) + handles.axes_p(3)/2;
handles.axes_cy = handles.axes_p(2) + handles.axes_p(4)/2;
handles.f_p = get(handles.figure1,'Position');
handles.c = handles.c / handles.f_p(3);
handles.r = handles.r / handles.f_p(4);
handles.c_x = handles.c / 2;
handles.c_y = handles.r / 2;
set(handles.axes1,'Position',[handles.axes_cx-handles.c_x handles.axes_cy-handles.c_y
handles.c handles.r]);
imshow(handles.img,'InitialMagnification',110);
handles.time = 1;
handles.reward = 0;
handles.mgv = 100;
handles.gameleft = 20;
handles.ptime = 0;
set(handles.EDT_inflation,'String',num2str(0));
%set(handles.EDT_reward,'String',num2str(0));
handles.r_e = [0 2.1 4.2 6.3 14.6 23.9 31.3 43.8 56.3 68.8 79.2 89.6];
handles.Wager = [0 0.05 0.15 0.25 0.55 0.95 1.45 2.05 2.75 3.45 4.25 5.15];
% h1 = waitbar(0,'Please wait...');
% for i = 1 : 15
%     %message = ['Please wait for ' num2str(15-i) 's'];
%     waitbar(i / 15);
%     pause(1);
% end
% delete(h1);
% Update handles structure
guidata(hObject, handles);
% UIWAIT makes passive wait for user response (see UIRESUME)
% uiwait(handles.figure1);

% --- Outputs from this function are returned to the command line.
function varargout = passive_OutputFcn(hObject, eventdata, handles)
% varargout    cell array for returning output args (see VARARGOUT);
% hObject      handle to figure
% eventdata    reserved - to be defined in a future version of MATLAB
% handles      structure with handles and user data (see GUIDATA)

```

```

% Get default command line output from handles structure
varargout{1} = handles.output;

function EDT_reward_Callback(hObject, eventdata, handles)
% hObject    handle to EDT_reward (see GCBO)
% eventdata  reserved - to be defined in a future version of MATLAB
% handles     structure with handles and user data (see GUIDATA)
% Hints: get(hObject,'String') returns contents of EDT_reward as text
%          str2double(get(hObject,'String')) returns contents of EDT_reward as a double

% --- Executes during object creation, after setting all properties.
function EDT_reward_CreateFcn(hObject, eventdata, handles)
% hObject    handle to EDT_reward (see GCBO)
% eventdata  reserved - to be defined in a future version of MATLAB
% handles     empty - handles not created until after all CreateFcns called
% Hint: edit controls usually have a white background on Windows.
%          See ISPC and COMPUTER.
if ispc && isequal(get(hObject,'BackgroundColor'), get(0,'defaultUicontrolBackgroundColor'))
    set(hObject,'BackgroundColor','white');
end

function EDT_inflation_Callback(hObject, eventdata, handles)
% hObject    handle to EDT_inflation (see GCBO)
% eventdata  reserved - to be defined in a future version of MATLAB
% handles     structure with handles and user data (see GUIDATA)
% Hints: get(hObject,'String') returns contents of EDT_inflation as text
%          str2double(get(hObject,'String')) returns contents of EDT_inflation as a double

% --- Executes during object creation, after setting all properties.
function EDT_inflation_CreateFcn(hObject, eventdata, handles)
% hObject    handle to EDT_inflation (see GCBO)
% eventdata  reserved - to be defined in a future version of MATLAB
% handles     empty - handles not created until after all CreateFcns called
% Hint: edit controls usually have a white background on Windows.
%          See ISPC and COMPUTER.
if ispc && isequal(get(hObject,'BackgroundColor'), get(0,'defaultUicontrolBackgroundColor'))
    set(hObject,'BackgroundColor','white');
end

% --- Executes on button press in BTN_cont.
function BTN_cont_Callback(hObject, eventdata, handles)
% hObject    handle to BTN_cont (see GCBO)
% eventdata  reserved - to be defined in a future version of MATLAB
% handles     structure with handles and user data (see GUIDATA)
if handles.time - 1 == 0;
    handles.t1 = clock;
end
handles.reward_temp = 0;
flg = 1; % set flag
set(handles.EDT_time,'String',[]);
set(handles.BTN_cont,'Enable','off');

```

```

if handles.gameleft ~= 0
    set(handles.EDT_gameleft,'String',num2str(handles.gameleft));
    f_t = ceil(12*rand(1));
    %-----%
    if f_t == 13
        handles.t2 = clock;
        handles.playtime(21 - handles.gameleft) = (handles.t2(4) - handles.t1(4))*60^2 +
(handles.t2(5) - handles.t1(5))*60 + handles.t2(6) - handles.t1(6);
        handles.win(21 - handles.gameleft) = 1;
        filename = [cd '\bmp\win.jpg'];
        A = imread(filename);
        set(handles.axes1,'Position',handles.axes_p);
        handles.reward = handles.reward + sum(handles.Wager);
        handles.money(21 - handles.gameleft) = handles.reward;
        set(handles.EDT_inflation,'String',num2str(13));
        set(handles.EDT_reward,'String',num2str(sum(handles.Wager)));
        imshow(A,'InitialMagnification',100);
        handles.gameleft = handles.gameleft - 1;
        if handles.gameleft == 0
            pause(15);
            close;
            main;
            return;
        else
            set(handles.EDT_gameleft,'String',num2str(handles.gameleft));
        end
        %%%%%%%%%%%%%%% cool-
down %%%%%%%%%%%%%%%
        for i = 1 : 15
            message = ['Next game will begin in ' num2str(16-i) 's'];
            set(handles.EDT_time,'String',message);
            pause(1);
        end
        %%%%%%%%%%%%%%%
        %%%%%%%%%%%%%%%
        set(handles.BTN_cont,'Enable','on');
        set(handles.EDT_time,'String',[]);
        set(handles.EDT_reward,'String',[]);
        set(handles.axes1,'Position',[handles.axes_cx-handles.c_x handles.axes_cy-
handles.c_y handles.c handles.r]);
        imshow(handles.img,'InitialMagnification',100);
        handles.time = 1;
        handles.mgv = 100;
        set(handles.EDT_inflation,'String',num2str(0));
        set(handles.BTN_cont,'Enable','on');
        set(handles.BTN_stop,'Enable','on');
        flg = 0;
    end
    %-----%
    if f_t < 13
        while (f_t ~= 0)
            idx = 100*rand(1);

```

```

%-----%
if idx <= handles.r_e(handles.time)
    handles.reward_temp = 0;
    [y, Fs] = wavread([cd '\bmp\explode.wav']);
    player = audioplayer(y, Fs);
    play(player);
    handles.t2 = clock;
    handles.playtime(21 - handles.gameleft) = (handles.t2(4) -
handles.t1(4))*60^2 + (handles.t2(5) - handles.t1(5))*60 + handles.t2(6) - handles.t1(6);
    set(handles.axes1,'Position',handles.axes_p);
    filename = [cd '\bmp\bb24_b.jpg'];
    A = imread(filename);
    imshow(A,'InitialMagnification',100);
    pause(2);
    filename = [cd '\bmp\lose.jpg'];
    A = imread(filename);
    imshow(A,'InitialMagnification',100);
    set(handles.EDT_inflation,'String',num2str(handles.time));
    set(handles.EDT_reward,'String',num2str(handles.reward));
    set(handles.BTN_cont,'Enable','off');
    set(handles.BTN_stop,'Enable','off');
    handles.win(21 - handles.gameleft) = 0;
    handles.money(21 - handles.gameleft) = 0;
    handles.gameleft = handles.gameleft - 1;
    handles.inflation(21 - handles.gameleft) = handles.time - 1;
    if handles.gameleft == 0
        pause(15);
        close;
        main;

        return;
    else
        set(handles.EDT_gameleft,'String',num2str(handles.gameleft));
    end
    %%%%%%%%%%%%%%% cool-
down %%%%%%%%%%%%%%%
    for i = 1 : 15
        message = ['Next game will begin in ' num2str(16-i) 's'];
        set(handles.EDT_time,'String',message);
        pause(1);
    end
    %%%%%%%%%%%%%%%
%%%%%%%%%%%%%%
    set(handles.BTN_cont,'Enable','on');
    set(handles.EDT_time,'String',[]);
    set(handles.axes1,'Position',[handles.axes_cx-handles.c_x handles.axes_cy-
handles.c_y handles.c handles.r]);
    set(handles.EDT_reward,'String',[]);
    imshow(handles.img,'InitialMagnification',100);
    handles.time = 1;
    handles.mgv = 100;
    set(handles.EDT_inflation,'String',num2str(0));

```

```

        set(handles.BTN_cont,'Enable','on');
        set(handles.BTN_stop,'Enable','on');
        flg = 0;
        break;
    end
    %------%
    handles.mgv = handles.mgv + 10;
    nx = handles.c * (handles.mgv/100);
    ny = handles.r * (handles.mgv/100);
    c_x = nx / 2;
    c_y = ny / 2;
    set(handles.axes1,'Position',[handles.axes_cx-c_x handles.axes_cy-c_y nx ny]);
    imshow(handles.img,'InitialMagnification',handles.mgv);
    handles.reward_temp = handles.reward_temp + handles.Wager(handles.time);
    set(handles.EDT_inflation,'String',num2str(handles.time));
    %           set(handles.EDT_reward,'String',num2str(handles.reward));
    handles.time = handles.time + 1;
    f_t = f_t - 1;
    pause(1);
end
end
%------%
if flg ~= 0
    handles.t2 = clock;
    handles.playtime(21 - handles.gameleft) = (handles.t2(4) - handles.t1(4))*60^2 +
(handles.t2(5) - handles.t1(5))*60 + handles.t2(6) - handles.t1(6);
    handles.win(21 - handles.gameleft) = 1;
    filename = [cd '\bmp\win.jpg'];
    A = imread(filename);
    set(handles.axes1,'Position',handles.axes_p);
    imshow(A,'InitialMagnification',100);
    handles.gameleft = handles.gameleft - 1;
    handles.reward = handles.reward + handles.reward_temp;
    handles.money(21 - handles.gameleft) = handles.reward;
    handles.inflation(21 - handles.gameleft) = handles.time - 1 ;
    set(handles.EDT_gameleft,'String',num2str(handles.gameleft));
    set(handles.EDT_reward,'String',num2str(handles.reward));
    if handles.gameleft == 0
        pause(15);
        close;
        main;

        return;
    else
        set(handles.EDT_gameleft,'String',num2str(handles.gameleft));
    end
    %%%%%%%%%%%%% cool-
down %%%%%%%%%%%%%
    for i = 1 : 15
        message = ['Next game will begin in ' num2str(16-i) 's'];
        set(handles.EDT_time,'String',message);
        pause(1);
    end
end

```

```

end
%%%%%%%%%%%%%%%%%%%%%%%%%%%%%%%%%%%%%%%%%%%%%%%%%%%%%%%%%%%%%%%%%%%%%%%%%%%%%%
%%%%%%%%%%%%%%%%%%%%%%%%%%%%%%%%%%%%%%%%%%%%%%%%%%%%%%%%%%%%%%%%%%%%%%%%%%%%%%
set(handles.BTN_cont,'Enable','on');
set(handles.EDT_time,'String',[]);
set(handles.axes1,'Position',[handles.axes_cx-handles.c_x handles.axes_cy-
handles.c_y handles.c handles.r]);
imshow(handles.img,'InitialMagnification',100);
set(handles.EDT_reward,'String',[]);
handles.time = 1;
handles.mgv = 100;
set(handles.EDT_inflation,'String',num2str(0));
set(handles.BTN_cont,'Enable','on');
set(handles.BTN_stop,'Enable','on');
end
end
clear f_t_idx;
% set(handles.EDT_gameleft,'String',num2str(handles.gameleft));
guidata(hObject, handles);

% --- Executes on button press in BTN_quit.
function BTN_quit_Callback(hObject, eventdata, handles)
% hObject    handle to BTN_quit (see GCBO)
% eventdata  reserved - to be defined in a future version of MATLAB
% handles    structure with handles and user data (see GUIDATA)

% --- Executes on button press in BTN_again.
function BTN_again_Callback(hObject, eventdata, handles)
% hObject    handle to BTN_again (see GCBO)
% eventdata  reserved - to be defined in a future version of MATLAB
% handles    structure with handles and user data (see GUIDATA)

function EDT_time_Callback(hObject, eventdata, handles)
% hObject    handle to EDT_time (see GCBO)
% eventdata  reserved - to be defined in a future version of MATLAB
% handles    structure with handles and user data (see GUIDATA)
% Hints: get(hObject,'String') returns contents of EDT_time as text
%        str2double(get(hObject,'String')) returns contents of EDT_time as a double

% --- Executes during object creation, after setting all properties.
function EDT_time_CreateFcn(hObject, eventdata, handles)
% hObject    handle to EDT_time (see GCBO)
% eventdata  reserved - to be defined in a future version of MATLAB
% handles    empty - handles not created until after all CreateFcns called

% Hint: edit controls usually have a white background on Windows.
%        See ISPC and COMPUTER.
if ispc && isequal(get(hObject,'BackgroundColor'), get(0,'defaultUicontrolBackgroundColor'))
    set(hObject,'BackgroundColor','white');
end

```

```

function EDT_gameleft_Callback(hObject, eventdata, handles)
% hObject    handle to EDT_gameleft (see GCBO)
% eventdata  reserved - to be defined in a future version of MATLAB
% handles     structure with handles and user data (see GUIDATA)
% Hints: get(hObject,'String') returns contents of EDT_gameleft as text
%         str2double(get(hObject,'String')) returns contents of EDT_gameleft as a double

% --- Executes during object creation, after setting all properties.
function EDT_gameleft_CreateFcn(hObject, eventdata, handles)
% hObject    handle to EDT_gameleft (see GCBO)
% eventdata  reserved - to be defined in a future version of MATLAB
% handles     empty - handles not created until after all CreateFcns called

% Hint: edit controls usually have a white background on Windows.
%         See ISPC and COMPUTER.
if ispc && isequal(get(hObject,'BackgroundColor'), get(0,'defaultUicontrolBackgroundColor'))
    set(hObject,'BackgroundColor','white');
end

```


Appendix D

Matlab Program for 3D Imaging

Matlab code for 3D imaging

```
% Mapping the results
clear all; close all; clc;
%% load the data %%
load('dat01.mat');
aHbO = mean(bart.HbO(:,50:100),2);
aHbO(find(isnan(aHbO)==1)) = 0;
%% plot %%
load('mesh.mat'); % brain node coordinates
x = mesh.nodes(:,1);
y = mesh.nodes(:,2);
z = mesh.nodes(:,3);
xmax = 193;
ymax = 229;
zmax = 144;
xmin = 1;
ymin = 1;
zmin = 1;
xv = linspace(xmin, xmax, 193);
yv = linspace(ymin, ymax, 229);
zv = linspace(zmin, zmax, 144);
[Xinterp,Yinterp,Zinterp] = meshgrid(xv,yv,zv);
HbO = griddata(x,y,z,aHbO,Xinterp,Yinterp,Zinterp);
load('head_icbm_152.mat');
T1 = zeros(size(gm));
T1(:,50:end)= HbO;

figure(h);
E1 = gm;
p = patch(isosurface(x,y,z,E1,0.1));
isonormals(x,y,z,E1,p);
isocolors(x,y,z,T1,p);
set(p,'FaceColor','interp','EdgeColor','none')
view(150,30); daspect([1 1 1]);axis tight
camlight; lighting phong;
colorbar;
axis off;
```

References

- [1] C. A. Barnes, "Long-term potentiation and the ageing brain.," *Philos. Trans. R. Soc. Lond. B. Biol. Sci.*, vol. 358, pp. 765–772, 2003.
- [2] B. H. Anderton, "Ageing of the brain," *Mechanisms of Ageing and Development*, vol. 123, pp. 811–817, 2002.
- [3] L. T. Eyler, A. Sherzai, A. R. Kaup, and D. V. Jeste, "A review of functional brain imaging correlates of successful cognitive aging," *Biol. Psychiatry*, vol. 70, no. 2, pp. 115–122, 2011.
- [4] R. N. Spreng, M. Wojtowicz, and C. L. Grady, "Reliable differences in brain activity between young and old adults: A quantitative meta-analysis across multiple cognitive domains," *Neurosci. Biobehav. Rev.*, vol. 34, no. 8, pp. 1178–1194, 2010.
- [5] A. C. McCarrey, J. D. Henry, W. von Hippel, G. Weidemann, P. S. Sachdev, M. J. a Wohl, and M. Williams, "Age Differences in Neural Activity during Slot Machine Gambling: An fMRI Study," *PLoS One*, vol. 7, no. 11, 2012.
- [6] C. Rogalsky, C. Vidal, X. Li, and H. Damasio, "Risky decision-making in older adults without cognitive deficits: an fMRI study of VMPFC using the Iowa Gambling Task.," *Soc. Neurosci.*, vol. 7, no. 2, pp. 178–90, Jan. 2012.
- [7] P. Liu, A. C. Hebrank, K. M. Rodrigue, K. M. Kennedy, J. Section, D. C. Park, and H. Lu, "Age-related differences in memory-encoding fMRI responses after accounting for decline in vascular reactivity," *Neuroimage*, vol. 78, pp. 415–425, 2013.
- [8] G. R. Turner and R. N. Spreng, "Executive functions and neurocognitive aging: Dissociable patterns of brain activity," *Neurobiol. Aging*, vol. 33, no. 4, pp. 826.e1–826.e13, 2012.
- [9] R. Peters, "Ageing and the brain.," *Postgrad. Med. J.*, vol. 82, no. 964, pp. 84–8, Feb. 2006.
- [10] S. B. R. E. Brown and K. R. Ridderinkhof, "Aging and the neuroeconomics of decision making: A review.," *Cogn. Affect. Behav. Neurosci.*, vol. 9, no. 4, pp. 365–79, Dec. 2009.
- [11] R. van den Bos, J. Homberg, and L. de Visser, "A critical review of sex differences in decision-making tasks: focus on the Iowa Gambling Task.," *Behav. Brain Res.*, vol. 238, pp. 95–108, Feb. 2013.

- [12] T. M. C. Lee, C. C. H. Chan, A. W. S. Leung, P. T. Fox, and J. H. Gao, "Sex-related differences in neural activity during risk taking: An fMRI study," *Cereb. Cortex*, vol. 19, no. June, pp. 1303–1312, 2009.
- [13] K. McRae, K. N. Ochsner, I. B. Mauss, J. J. D. Gabrieli, and J. J. Gross, "Gender Differences in Emotion Regulation: An fMRI Study of Cognitive Reappraisal," *Gr. Process. Integr. Relations*, vol. 11, no. 2, pp. 143–162, 2008.
- [14] F. Tian, M. R. Delgado, S. C. Dhamne, B. Khan, G. Alexandrakis, M. I. Romero, L. Smith, D. Reid, N. J. Clegg, and H. Liu, "Quantification of functional near infrared spectroscopy to assess cortical reorganization in children with cerebral palsy.," *Opt. Express*, vol. 18, pp. 25973–25986, 2010.
- [15] F. Tian, H. Niu, B. Khan, G. Alexandrakis, K. Behbehani, and H. Liu, "Enhanced functional brain imaging by using adaptive filtering and a depth compensation algorithm in diffuse optical tomography.," *IEEE Trans. Med. Imaging*, vol. 30, pp. 1239–1251, 2011.
- [16] M. Cazzell, L. Li, Z.-J. Lin, S. J. Patel, and H. Liu, "Comparison of neural correlates of risk decision making between genders: an exploratory fNIRS study of the Balloon Analogue Risk Task (BART).," *Neuroimage*, vol. 62, no. 3, pp. 1896–911, Sep. 2012.
- [17] T. Tsujii and S. Watanabe, "Neural correlates of dual-task effect on belief-bias syllogistic reasoning: a near-infrared spectroscopy study.," *Brain Res.*, vol. 1287, pp. 118–125, 2009.
- [18] M. M. Plichta, M. J. Herrmann, C. G. Baehne, A.-C. Ehlis, M. M. Richter, P. Pauli, and A. J. Fallgatter, "Event-related functional near-infrared spectroscopy (fNIRS) based on craniocerebral correlations: reproducibility of activation?," *Hum. Brain Mapp.*, vol. 28, pp. 733–741, 2007.
- [19] M. Schecklmann, A.-C. Ehlis, M. M. Plichta, and A. J. Fallgatter, "Functional near-infrared spectroscopy: a long-term reliable tool for measuring brain activity during verbal fluency.," *Neuroimage*, vol. 43, pp. 147–155, 2008.
- [20] D. R. Leff, F. Orihuela-Espina, C. E. Elwell, T. Athanasiou, D. T. Delpy, A. W. Darzi, and G.-Z. Yang, "Assessment of the cerebral cortex during motor task behaviours in adults: a systematic review of functional near infrared spectroscopy (fNIRS) studies.," *Neuroimage*, vol. 54, pp. 2922–2936, 2011.
- [21] J. C. Ye, S. Tak, K. E. Jang, J. Jung, and J. Jang, "NIRS-SPM: statistical parametric mapping for near-infrared spectroscopy.," *Neuroimage*, vol. 44, no. 2, pp. 428–47, Jan. 2009.

- [22] X. Cui, S. Bray, D. M. Bryant, G. H. Glover, and A. L. Reiss, "A quantitative comparison of NIRS and fMRI across multiple cognitive tasks.," *Neuroimage*, vol. 54, pp. 2808–2821, 2011.
- [23] E. Bullmore and O. Sporns, "Complex brain networks: graph theoretical analysis of structural and functional systems.," *Nat. Rev. Neurosci.*, vol. 10, no. 3, pp. 186–98, Mar. 2009.
- [24] C. J. Stam and J. C. Reijneveld, "Graph theoretical analysis of complex networks in the brain.," *Nonlinear Biomed. Phys.*, vol. 1, no. 1, p. 3, Jan. 2007.
- [25] H. Niu and Y. He, "Resting-State Functional Brain Connectivity: Lessons from Functional Near-Infrared Spectroscopy.," *Neuroscientist*, Sep. 2013.
- [26] S.-J. Blakemore and T. W. Robbins, "Decision-making in the adolescent brain.," *Nat. Neurosci.*, vol. 15, no. 9, pp. 1184–91, Sep. 2012.
- [27] Y. Stern, C. Habeck, J. Moeller, N. Scarmeas, K. E. Anderson, H. J. Hilton, J. Flynn, H. Sackeim, and R. van Heertum, "Brain networks associated with cognitive reserve in healthy young and old adults.," *Cereb. Cortex*, vol. 15, no. 4, pp. 394–402, Apr. 2005.
- [28] X. Liang, Q. Zou, Y. He, and Y. Yang, "Coupling of functional connectivity and regional cerebral blood flow reveals a physiological basis for network hubs of the human brain.," *Proc. Natl. Acad. Sci. U. S. A.*, vol. 110, no. 5, pp. 1929–34, Jan. 2013.
- [29] J. Steffener, C. G. Habeck, and Y. Stern, "Age-related changes in task related functional network connectivity.," *PLoS One*, vol. 7, no. 9, p. e44421, Jan. 2012.
- [30] P. a Reuter-Lorenz, J. Jonides, E. E. Smith, A. Hartley, A. Miller, C. Marshuetz, and R. a Koeppe, "Age differences in the frontal lateralization of verbal and spatial working memory revealed by PET.," *J. Cogn. Neurosci.*, vol. 12, no. 1, pp. 174–87, Jan. 2000.
- [31] I. E. Dror, M. Katona, and K. Mungur, "Age differences in decision making: to take a risk or not?," *Gerontology*, vol. 44, no. 2, pp. 67–71, Jan. 1998.
- [32] E. R. Sowell, P. M. Thompson, C. J. Holmes, R. Batth, T. L. Jernigan, and a W. Toga, "Localizing age-related changes in brain structure between childhood and adolescence using statistical parametric mapping.," *Neuroimage*, vol. 9, no. 6 Pt 1, pp. 587–97, Jun. 1999.
- [33] J. V Haxby and J. M. Maisog, "Age-related Processing Changes in Cortical Blood Flow Activation of Faces and Location during Visual," vol. 14, no. March, 1994.

- [34] R. Mata, A. K. Josef, G. R. Samanez-Larkin, and R. Hertwig, "Age differences in risky choice: a meta-analysis," *Ann. N. Y. Acad. Sci.*, vol. 1235, pp. 18–29, Oct. 2011.
- [35] L. V. Wang and Hsin-I Wu, *Biomedical Optics: Principles and Imaging*. 2012.
- [36] F. Irani, S. M. Platek, S. Bunce, A. C. Ruocco, and D. Chute, "Functional near infrared spectroscopy (fNIRS): an emerging neuroimaging technology with important applications for the study of brain disorders," *Clin. Neuropsychol.*, vol. 21, no. 1, pp. 9–37, Jan. 2007.
- [37] X. Cui, S. Bray, D. M. Bryant, G. H. Glover, and A. L. Reiss, "A quantitative comparison of NIRS and fMRI across multiple cognitive tasks," *Neuroimage*, vol. 54, pp. 2808–2821, 2011.
- [38] M. Takeuchi, E. Hori, K. Takamoto, A. H. Tran, K. Satoru, A. Ishikawa, T. Ono, S. Endo, and H. Nishijo, "Brain cortical mapping by simultaneous recording of functional near infrared spectroscopy and electroencephalograms from the whole brain during right median nerve stimulation," *Brain Topogr.*, vol. 22, pp. 197–214, 2009.
- [39] M. A. Franceschini and D. a Boas, "Noninvasive measurement of neuronal activity with near-infrared optical imaging," *Neuroimage*, vol. 21, no. 1, pp. 372–386, Jan. 2004.
- [40] B. R. White and J. P. Culver, "Phase-encoded retinotopy as an evaluation of diffuse optical neuroimaging.," *Neuroimage*, vol. 49, pp. 568–577, 2010.
- [41] Y. Zhan, A. T. Eggebrecht, J. P. Culver, and H. Dehghani, "Image quality analysis of high-density diffuse optical tomography incorporating a subject-specific head model.," *Front. Neuroenergetics*, vol. 4, no. May, p. 6, Jan. 2012.
- [42] D. A. Boas and A. M. Dale, "Simulation study of magnetic resonance imaging-guided cortically constrained diffuse optical tomography of human brain function," *Appl. Opt.*, vol. 44, pp. 1957–1968, 2005.
- [43] R. J. Cooper, M. Caffini, J. Dubb, Q. Fang, A. Custo, D. Tsuzuki, B. Fischl, W. Wells, I. Dan, and D. a Boas, "Validating atlas-guided DOT: a comparison of diffuse optical tomography informed by atlas and subject-specific anatomies.," *Neuroimage*, vol. 62, no. 3, pp. 1999–2006, Sep. 2012.
- [44] A. T. Eggebrecht, B. R. White, S. L. Ferradal, C. Chen, Y. Zhan, A. Z. Snyder, H. Dehghani, and J. P. Culver, "A quantitative spatial comparison of high-density diffuse optical tomography and fMRI cortical mapping," *Neuroimage*, vol. 61, pp. 1120–1128, 2012.

- [45] B. W. Pogue, T. O. McBride, J. Prewitt, U. L. Osterberg, and K. D. Paulsen, "Spatially variant regularization improves diffuse optical tomography.," *Appl. Opt.*, vol. 38, pp. 2950–2961, 1999.
- [46] J. P. Culver, A. M. Siegel, J. J. Stott, and D. A. Boas, "Volumetric diffuse optical tomography of brain activity.," *Opt. Lett.*, vol. 28, pp. 2061–2063, 2003.
- [47] H. Niu, F. Tian, Z.-J. Lin, and H. Liu, "Development of a compensation algorithm for accurate depth localization in diffuse optical tomography.," *Opt. Lett.*, vol. 35, no. 3, pp. 429–31, Feb. 2010.
- [48] S. L. Ferradal, A. T. Eggebrecht, M. Hassanpour, A. Z. Snyder, and J. P. Culver, "Atlas-based head modeling and spatial normalization for high-density diffuse optical tomography: In vivo validation against fMRI," *Neuroimage*, vol. 85, pp. 117–126, 2014.
- [49] M. Jermyn, H. Ghadyani, M. a Mastanduno, W. Turner, S. C. Davis, H. Dehghani, and B. W. Pogue, "Fast segmentation and high-quality three-dimensional volume mesh creation from medical images for diffuse optical tomography.," *J. Biomed. Opt.*, vol. 18, no. 8, p. 86007, Aug. 2013.
- [50] A. K. Singh, M. Okamoto, H. Dan, V. Jurcak, and I. Dan, "Spatial registration of multichannel multi-subject fNIRS data to MNI space without MRI.," *Neuroimage*, vol. 27, no. 4, pp. 842–51, Oct. 2005.
- [51] S. Cutini, P. Scatturin, and M. Zorzi, "A new method based on ICBM152 head surface for probe placement in multichannel fNIRS.," *Neuroimage*, vol. 54, no. 2, pp. 919–27, Jan. 2011.
- [52] H. Dehghani, M. E. Eames, P. K. Yalavarthy, S. C. Davis, S. Srinivasan, C. M. Carpenter, B. W. Pogue, and K. D. Paulsen, "Near infrared optical tomography using NIRFAST : Algorithm for numerical model and image reconstruction," no. August 2008, pp. 711–732, 2009.
- [53] S. R. Arridge, "Optical tomography in medical imaging," *Inverse Problems*, vol. 15, pp. R41–R93, 1999.
- [54] J. A. Fill and D. E. Fishkind, "The Moore--Penrose Generalized Inverse for Sums of Matrices," *SIAM J. Matrix Anal. Appl.*, vol. 21, no. 2, pp. 629–635, Jan. 2000.
- [55] X. Song, B. W. Pogue, S. Jiang, M. M. Doyley, H. Dehghani, T. D. Tosteson, and K. D. Paulsen, "Automated region detection based on the contrast-to-noise ratio in near-infrared tomography.," *Appl. Opt.*, vol. 43, no. 5, pp. 1053–62, Feb. 2004.
- [56] I. Paper, "METHODS FOR THE EVALUATION OF IMAGE QUALITY : A REVIEW," vol. 90, pp. 89–99, 2000.

- [57] P. E. Shrout and J. L. Fleiss, "Intraclass correlations: uses in assessing rater reliability.," *Psychol. Bull.*, vol. 86, no. 2, pp. 420–8, Mar. 1979.
- [58] K. O. McGraw and S. P. Wong, "Forming inferences about some intraclass correlation coefficients.," *Psychological Methods*, vol. 1. pp. 30–46, 1996.
- [59] J. P. Weir, "Quantifying test-retest reliability using the intraclass correlation coefficient and the SEM.," *J. Strength Cond. Res.*, vol. 19, pp. 231–240, 2005.
- [60] M. M. Plichta, M. J. Herrmann, C. G. Baehne, a-C. Ehli, M. M. Richter, P. Pauli, and a J. Fallgatter, "Event-related functional near-infrared spectroscopy (fNIRS): are the measurements reliable?," *Neuroimage*, vol. 31, no. 1, pp. 116–24, May 2006.
- [61] Y. Bhambhani, R. Maikala, M. Farag, and G. Rowland, "Reliability of near-infrared spectroscopy measures of cerebral oxygenation and blood volume during handgrip exercise in nondisabled and traumatic brain-injured subjects," *J. Rehabil. Res. Dev.*, vol. 43, no. 7, p. 845, 2006.
- [62] U. Braun, M. M. Plichta, C. Esslinger, C. Sauer, L. Haddad, O. Grimm, D. Mier, S. Mohnke, A. Heinz, S. Erk, H. Walter, N. Seiferth, P. Kirsch, and A. Meyer-Lindenberg, "Test-retest reliability of resting-state connectivity network characteristics using fMRI and graph theoretical measures.," *Neuroimage*, vol. 59, no. 2, pp. 1404–12, Jan. 2012.
- [63] H. Zhang, L. Duan, Y.-J. Zhang, C.-M. Lu, H. Liu, and C.-Z. Zhu, "Test-retest assessment of independent component analysis-derived resting-state functional connectivity based on functional near-infrared spectroscopy.," *Neuroimage*, vol. 55, no. 2, pp. 607–15, Mar. 2011.
- [64] J.-H. Wang, X.-N. Zuo, S. Gohel, M. P. Milham, B. B. Biswal, and Y. He, "Graph theoretical analysis of functional brain networks: test-retest evaluation on short- and long-term resting-state functional MRI data.," *PLoS One*, vol. 6, no. 7, p. e21976, Jan. 2011.
- [65] M. M. Plichta, A. J. Schwarz, O. Grimm, K. Morgen, D. Mier, L. Haddad, A. B. M. Gerdes, C. Sauer, H. Tost, C. Esslinger, P. Colman, F. Wilson, P. Kirsch, and A. Meyer-Lindenberg, "Test-retest reliability of evoked BOLD signals from a cognitive-emotive fMRI test battery.," *Neuroimage*, vol. 60, no. 3, pp. 1746–58, Apr. 2012.
- [66] F. Tian, F. A. Kozel, A. Yennu, P. E. Croarkin, S. M. McClintock, K. S. Mapes, M. M. Husain, and H. Liu, "Test-retest assessment of cortical activation induced by repetitive transcranial magnetic stimulation with brain atlas-guided optical topography.," *J. Biomed. Opt.*, vol. 17, no. 11, p. 116020, Nov. 2012.

- [67] C. C. Guo, F. Kurth, J. Zhou, E. a Mayer, S. B. Eickhoff, J. H. Kramer, and W. W. Seeley, "One-year test-retest reliability of intrinsic connectivity network fMRI in older adults.," *Neuroimage*, vol. 61, no. 4, pp. 1471–83, Jul. 2012.
- [68] H. Niu, Z. Li, X. Liao, J. Wang, T. Zhao, N. Shu, X. Zhao, and Y. He, "Test-Retest Reliability of Graph Metrics in Functional Brain Networks: A Resting-State fNIRS Study.," *PLoS One*, vol. 8, no. 9, p. e72425, Jan. 2013.
- [69] M. Fiecas, H. Ombao, D. van Lunen, R. Baumgartner, A. Coimbra, and D. Feng, "Quantifying temporal correlations: a test-retest evaluation of functional connectivity in resting-state fMRI.," *Neuroimage*, vol. 65, pp. 231–41, Jan. 2013.
- [70] H. Cao, M. M. Plichta, A. Schäfer, L. Haddad, O. Grimm, M. Schneider, C. Esslinger, P. Kirsch, A. Meyer-Lindenberg, and H. Tost, "Test-retest reliability of fMRI-based graph theoretical properties during working memory, emotion processing, and resting state.," *Neuroimage*, vol. 84C, pp. 888–900, Sep. 2013.
- [71] J. L. Fleiss, *The Design and Analysis of Clinical Experiments*. Hoboken, NJ, USA: John Wiley & Sons, Inc., 1999.
- [72] D. V. Cicchetti, "Guidelines, criteria, and rules of thumb for evaluating normed and standardized assessment instruments in psychology.," *Psychological Assessment*, vol. 6, pp. 284–290, 1994.
- [73] D. J. Brandt, J. Sommer, S. Krach, J. Bedenbender, T. Kircher, F. M. Paulus, and A. Jansen, "Test-Retest Reliability of fMRI Brain Activity during Memory Encoding.," *Front. psychiatry*, vol. 4, p. 163, 2013.
- [74] X.-H. Liao, M.-R. Xia, T. Xu, Z.-J. Dai, X.-Y. Cao, H.-J. Niu, X.-N. Zuo, Y.-F. Zang, and Y. He, "Functional brain hubs and their test-retest reliability: a multiband resting-state functional MRI study.," *Neuroimage*, vol. 83, pp. 969–82, Dec. 2013.
- [75] D. S. Manoach, E. F. Halpern, T. S. Kramer, Y. Chang, D. C. Goff, S. L. Rauch, D. N. Kennedy, and R. L. Gollub, "Test-retest reliability of a functional MRI working memory paradigm in normal and schizophrenic subjects.," *Am. J. Psychiatry*, vol. 158, pp. 955–958, 2001.
- [76] T. J. Kimberley, G. Khandekar, and M. Borich, "fMRI reliability in subjects with stroke.," *Exp. Brain Res.*, vol. 186, pp. 183–190, 2008.
- [77] C. W. Lejuez, J. P. Read, C. W. Kahler, J. B. Richards, S. E. Ramsey, G. L. Stuart, D. R. Strong, and R. A. Brown, "Evaluation of a behavioral measure of risk taking: The Balloon Analogue Risk Task (BART).," *J. Exp. Psychol. Appl.*, vol. 8, no. 2, pp. 75–84, 2002.

- [78] T. J. Pleskac, T. S. Wallsten, P. Wang, and C. W. Lejuez, "Development of an automatic response mode to improve the clinical utility of sequential risk-taking tasks.," *Exp. Clin. Psychopharmacol.*, vol. 16, no. 6, pp. 555–64, Dec. 2008.
- [79] C. W. Lejuez, W. Aklin, M. Bornovalova, and E. T. Moolchan, "Differences in risk-taking propensity across inner-city adolescent ever- and never-smokers.," *Nicotine Tob. Res.*, vol. 7, pp. 71–79, 2005.
- [80] T. J. Crowley, K. M. Raymond, S. K. Mikulich-Gilbertson, L. L. Thompson, and C. W. Lejuez, "A risk-taking 'set' in a novel task among adolescents with serious conduct and substance problems.," *J. Am. Acad. Child Adolesc. Psychiatry*, vol. 45, pp. 175–183, 2006.
- [81] W. M. Aklin, C. W. Lejuez, M. J. Zvolensky, C. W. Kahler, and M. Gwadz, "Evaluation of behavioral measures of risk taking propensity with inner city adolescents," *Behav. Res. Ther.*, vol. 43, pp. 215–228, 2005.
- [82] H. Rao, M. Korczykowski, J. Pluta, A. Hoang, and J. A. Detre, "Neural correlates of voluntary and involuntary risk taking in the human brain: an fMRI Study of the Balloon Analog Risk Task (BART).," *Neuroimage*, vol. 42, no. 2, pp. 902–10, Aug. 2008.
- [83] J. C. Ye, S. Tak, K. E. Jang, J. Jung, and J. Jang, "NIRS-SPM: Statistical parametric mapping for near-infrared spectroscopy," *Neuroimage*, vol. 44, pp. 428–447, 2009.
- [84] A. Miyake, N. P. Friedman, D. a. Rettinger, P. Shah, and M. Hegarty, "How Are Visuospatial Working Memory, Executive Functioning, and Spatial Abilities Related? A Latent-Variable Analysis*1," *J. Exp. Psychol. Gen.*, vol. 130, p. 19, 2001.
- [85] T. A. Salthouse, "Aging associations: influence of speed on adult age differences in associative learning.," *J. Exp. Psychol. Learn. Mem. Cogn.*, vol. 20, pp. 1486–1503, 1994.
- [86] G. Atkinson and A. M. Nevill, "Statistical methods for assessing measurement error (reliability) in variables relevant to sports medicine.," *Sports Med.*, vol. 26, pp. 217–238, 1998.
- [87] F. B. Haeussinger, S. Heinzl, T. Hahn, M. Schecklmann, A.-C. Ehlis, and A. J. Fallgatter, "Simulation of near-infrared light absorption considering individual head and prefrontal cortex anatomy: implications for optical neuroimaging.," *PLoS One*, vol. 6, no. 10, p. e26377, Jan. 2011.
- [88] L. Minati, I. U. Kress, E. Visani, N. Medford, and H. D. Critchley, "Intra- and extra-cranial effects of transient blood pressure changes on brain near-infrared

- spectroscopy (NIRS) measurements.,” *J. Neurosci. Methods*, vol. 197, no. 2, pp. 283–8, Apr. 2011.
- [89] S. Heinzel, F. B. Haeussinger, T. Hahn, A.-C. Ehlis, M. M. Plichta, and A. J. Fallgatter, “Variability of (functional) hemodynamics as measured with simultaneous fNIRS and fMRI during intertemporal choice.,” *Neuroimage*, vol. 71, pp. 125–34, May 2013.
 - [90] I. Lipp, K. Murphy, R. G. Wise, and X. Caseras, “Understanding the contribution of neural and physiological signal variation to the low repeatability of emotion-induced BOLD responses.,” *Neuroimage*, vol. 86, pp. 335–42, Mar. 2014.
 - [91] F. B. Haeussinger, T. Dresler, S. Heinzel, M. Schecklmann, a J. Fallgatter, and a-C. Ehlis, “Reconstructing functional near-infrared spectroscopy (fNIRS) signals impaired by extra-cranial confounds: An easy-to-use filter method.,” *Neuroimage*, vol. 95, pp. 69–79, Jul. 2014.
 - [92] L. Gagnon, M. a Yücel, D. a Boas, and R. J. Cooper, “Further improvement in reducing superficial contamination in NIRS using double short separation measurements.,” *Neuroimage*, vol. 85 Pt 1, pp. 127–35, Jan. 2014.
 - [93] M. M. Plichta, S. Heinzel, a-C. Ehlis, P. Pauli, and a J. Fallgatter, “Model-based analysis of rapid event-related functional near-infrared spectroscopy (NIRS) data: a parametric validation study.,” *Neuroimage*, vol. 35, no. 2, pp. 625–34, Apr. 2007.
 - [94] S. Tak, J. Jang, K. Lee, and J. C. Ye, “Quantification of CMRO(2) without hypercapnia using simultaneous near-infrared spectroscopy and fMRI measurements.,” *Phys. Med. Biol.*, vol. 55, pp. 3249–3269, 2010.
 - [95] S. E. Petersen and J. W. Dubis, “The mixed block/event-related design.,” *Neuroimage*, vol. 62, no. 2, pp. 1177–84, Aug. 2012.
 - [96] J. C. Rajapakse, F. Kruggel, J. M. Maisog, and D. Y. von Cramon, “Modeling hemodynamic response for analysis of functional MRI time-series.,” *Hum. Brain Mapp.*, vol. 6, pp. 283–300, 1998.
 - [97] M. M. Monti, “Statistical Analysis of fMRI Time-Series: A Critical Review of the GLM Approach.,” *Front. Hum. Neurosci.*, vol. 5, no. March, p. 28, Jan. 2011.
 - [98] W. Penny and A. Holmes, “Random-Effects Analysis,” in *Human Brain Function: Second Edition*, 2003, pp. 843–850.
 - [99] K. J. Worsley and K. J. Friston, “Analysis of FMRI time series revisited - again,” *Neuroimage*, vol. 2, pp. 173–181, 1995.
 - [100] S. A. Huettel, A. W. Song, and G. McCarthy, *Functional magnetic resonance imaging*. 2004.

- [101] K. J. Friston, A. P. Holmes, J. B. Poline, P. J. Grasby, S. C. Williams, R. S. Frackowiak, and R. Turner, "Analysis of fMRI time-series revisited.," *Neuroimage*, vol. 2, pp. 45–53, 1995.
- [102] M. S. Hassanpour, B. R. White, A. T. Eggebrecht, S. L. Ferradal, A. Z. Snyder, and J. P. Culver, "Statistical analysis of high density diffuse optical tomography.," *Neuroimage*, vol. 85 Pt 1, pp. 104–16, Jan. 2014.
- [103] Q. Zou, T. J. Ross, H. Gu, X. Geng, X.-N. Zuo, L. E. Hong, J.-H. Gao, E. a Stein, Y.-F. Zang, and Y. Yang, "Intrinsic resting-state activity predicts working memory brain activation and behavioral performance.," *Hum. Brain Mapp.*, vol. 34, no. 12, pp. 3204–15, Dec. 2013.
- [104] M. E. Raichle and M. A. Mintun, "Brain work and brain imaging.," *Annu. Rev. Neurosci.*, vol. 29, pp. 449–476, 2006.
- [105] Z.-J. Lin, L. Li, M. Cazzell, and H. Liu, "Atlas-guided volumetric diffuse optical tomography enhanced by generalized linear model analysis to image risk decision-making responses in young adults.," *Hum. Brain Mapp.*, vol. 00, no. November 2013, Mar. 2014.
- [106] Y. Benjamini and Y. Hochberg, "Controlling the False Discovery Rate: A Practical and Powerful Approach to Multiple Testing," *J. R. Stat. Soc. Ser. B*, vol. 57, pp. 289 – 300, 1995.
- [107] H. Dehghani, B. R. White, B. W. Zeff, A. Tizzard, and J. P. Culver, "Depth sensitivity and image reconstruction analysis of dense imaging arrays for mapping brain function with diffuse optical tomography.," *Appl. Opt.*, vol. 48, no. 10, pp. D137–43, Apr. 2009.
- [108] A. T. Eggebrecht, B. R. White, S. L. Ferradal, C. Chen, Y. Zhan, A. Z. Snyder, H. Dehghani, and J. P. Culver, "A quantitative spatial comparison of high-density diffuse optical tomography and fMRI cortical mapping.," *Neuroimage*, vol. 61, no. 4, pp. 1120–8, Jul. 2012.
- [109] H. Niu, J. Wang, T. Zhao, N. Shu, and Y. He, "Revealing topological organization of human brain functional networks with resting-state functional near infrared spectroscopy.," *PLoS One*, vol. 7, no. 9, p. e45771, Jan. 2012.
- [110] F. Tian and H. Liu, "Depth-compensated diffuse optical tomography enhanced by general linear model analysis and an anatomical atlas of human head.," *Neuroimage*, Jul. 2013.
- [111] R. W. Homan, J. Herman, and P. Purdy, "Cerebral location of international 10-20 system electrode placement.," *Electroencephalogr. Clin. Neurophysiol.*, vol. 66, pp. 376–382, 1987.

- [112] A. Custo, D. A. Boas, D. Tsuzuki, I. Dan, R. Mesquita, B. Fischl, W. E. L. Grimson, and W. Wells, "Anatomical atlas-guided diffuse optical tomography of brain activation," *Neuroimage*, vol. 49, pp. 561–567, 2010.
- [113] N. M. Gregg, B. R. White, B. W. Zeff, A. J. Berger, and J. P. Culver, "Brain specificity of diffuse optical imaging: improvements from superficial signal regression and tomography.," *Front. Neuroenergetics*, vol. 2, 2010.
- [114] A. L. Booth and P. J. Nolen, "Gender Differences in Risk Behaviour : Does Nurture Matter ?," no. 4026, 2009.
- [115] B. J. Casey, A. Galvan, and T. A. Hare, "Changes in cerebral functional organization during cognitive development.," *Curr. Opin. Neurobiol.*, vol. 15, no. 2, pp. 239–44, Apr. 2005.
- [116] B. J. Casey, N. Tottenham, C. Liston, and S. Durston, "Imaging the developing brain: what have we learned about cognitive development?," *Trends Cogn. Sci.*, vol. 9, no. 3, pp. 104–10, Mar. 2005.
- [117] A. Christakou, S. J. Gershman, Y. Niv, A. Simmons, M. Brammer, and K. Rubia, "Neural and psychological maturation of decision-making in adolescence and young adulthood.," *J. Cogn. Neurosci.*, vol. 25, no. 11, pp. 1807–23, Nov. 2013.
- [118] J. M. Goldstein, M. Jerram, R. Poldrack, R. Anagnoson, H. C. Breiter, N. Makris, J. M. Goodman, M. T. Tsuang, and L. J. Seidman, "Sex differences in prefrontal cortical brain activity during fMRI of auditory verbal working memory.," *Neuropsychology*, vol. 19, no. 4, pp. 509–19, Jul. 2005.
- [119] D. Tomasi and N. D. Volkow, "Gender differences in brain functional connectivity density.," *Hum. Brain Mapp.*, vol. 33, no. 4, pp. 849–60, Apr. 2012.
- [120] E. Weiss, C. M. Siedentopf, A. Hofer, E. a. Deisenhammer, M. J. Hoptman, C. Kremser, S. Golaszewski, S. Felber, W. W. Fleischhacker, and M. Delazer, "Sex differences in brain activation pattern during a visuospatial cognitive task: a functional magnetic resonance imaging study in healthy volunteers," *Neurosci. Lett.*, vol. 344, no. 3, pp. 169–172, Jul. 2003.
- [121] M. D. De Bellis, M. S. Keshavan, S. R. Beers, J. Hall, K. Frustaci, A. Masalehdan, J. Noll, and A. M. Boring, "Sex differences in brain maturation during childhood and adolescence.," *Cereb. Cortex*, vol. 11, pp. 552–557, 2001.
- [122] C. E. Coffey, "Sex Differences in Brain Aging: A Quantitative Magnetic Resonance Imaging Study," *Archives of Neurology*, vol. 55, pp. 169–179, 1998.
- [123] A. Abraham, K. Thybusch, K. Pieritz, and C. Hermann, "Gender differences in creative thinking: Behavioral and fMRI findings," *Brain Imaging Behav.*, vol. 8, pp. 39–51, 2014.

- [124] G. Dong, X. Lin, H. Zhou, and X. Du, "Decision-making after continuous wins or losses in a randomized guessing task: implications for how the prior selection results affect subsequent decision-making.," *Behav. Brain Funct.*, vol. 10, no. 1, p. 11, 2014.
- [125] T. M. C. Lee, A. W. S. Leung, P. T. Fox, J.-H. Gao, and C. C. H. Chan, "Age-related differences in neural activities during risk taking as revealed by functional MRI.," *Soc. Cogn. Affect. Neurosci.*, vol. 3, pp. 7–15, 2008.
- [126] S. Pudas, J. Persson, M. Josefsson, X. de Luna, L.-G. Nilsson, and L. Nyberg, "Brain Characteristics of Individuals Resisting Age-Related Cognitive Decline over Two Decades," *J. Neurosci.*, vol. 33, no. 20, pp. 8668–8677, 2013.
- [127] G. R. Samanez-Larkin and M. D'Esposito, "Group comparisons: Imaging the aging brain," *Soc. Cogn. Affect. Neurosci.*, vol. 3, pp. 290–297, 2008.
- [128] J. L. Woodard, M. Seidenberg, K. a. Nielson, J. C. Smith, P. Antuono, S. Durgerian, L. Guidotti, Q. Zhang, A. Butts, N. Hantke, M. Lancaster, and S. M. Rao, "Prediction of cognitive decline in healthy older adults using fMRI," *J. Alzheimer's Dis.*, vol. 21, pp. 871–885, 2010.
- [129] N. R. Lighthall, M. Sakaki, S. Vasunilashorn, L. Nga, S. Somayajula, E. Y. Chen, N. Samii, and M. Mather, "Gender differences in reward-related decision processing under stress.," *Soc. Cogn. Affect. Neurosci.*, vol. 7, no. 4, pp. 476–84, Apr. 2012.
- [130] A. K. Y. Mak, Z. Hu, J. X. X. Zhang, Z. Xiao, and T. M. C. Lee, "Sex-related differences in neural activity during emotion regulation.," *Neuropsychologia*, vol. 47, pp. 2900–2908, 2009.
- [131] M. Izzetoglu, K. Izzetoglu, S. Bunce, H. Ayaz, A. Devaraj, B. Onaral, and K. Pourrezaei, "Functional near-infrared neuroimaging," *IEEE Trans. Neural Syst. Rehabil. Eng.*, vol. 13, pp. 153–159, 2005.
- [132] D. Yurgelun-Todd, "Emotional and cognitive changes during adolescence," *Current Opinion in Neurobiology*, vol. 17, pp. 251–257, 2007.
- [133] E. R. Sowell, B. S. Peterson, P. M. Thompson, S. E. Welcome, A. L. Henkenius, and A. W. Toga, "Mapping cortical change across the human life span.," *Nat. Neurosci.*, vol. 6, no. 3, pp. 309–15, Mar. 2003.
- [134] B. S. Folley and S. Park, "Verbal creativity and schizotypal personality in relation to prefrontal hemispheric laterality: A behavioral and near-infrared optical imaging study," *Schizophr. Res.*, vol. 80, pp. 271–282, 2005.
- [135] Z. S. Nasreddine, N. A. Phillips, V. Bédirian, S. Charbonneau, V. Whitehead, I. Collin, J. L. Cummings, and H. Chertkow, "The Montreal Cognitive Assessment,

- MoCA: A brief screening tool for mild cognitive impairment," *J. Am. Geriatr. Soc.*, vol. 53, pp. 695–699, 2005.
- [136] R. Elliott, "Executive functions and their disorders," *Br. Med. Bull.*, vol. 65, no. 1, pp. 49–59, Mar. 2003.
 - [137] J.-B. Pochon, "The Role of Dorsolateral Prefrontal Cortex in the Preparation of Forthcoming Actions: an fMRI Study," *Cereb. Cortex*, vol. 11, no. 3, pp. 260–266, Mar. 2001.
 - [138] P. N. C. Mohr, S.-C. Li, and H. R. Heekeren, "Neuroeconomics and aging: neuromodulation of economic decision making in old age.," *Neurosci. Biobehav. Rev.*, vol. 34, no. 5, pp. 678–88, Apr. 2010.
 - [139] A. Marschner, T. Mell, I. Wartenburger, A. Villringer, F. M. Reischies, and H. R. Heekeren, "Reward-based decision-making and aging.," *Brain Res. Bull.*, vol. 67, no. 5, pp. 382–90, Nov. 2005.
 - [140] M. Ernst, K. Bolla, M. Mouratidis, C. Contoreggi, J. A. Matochik, V. Kurian, J. L. Cadet, A. S. Kimes, and E. D. London, "Decision-making in a risk-taking task: a PET study.," *Neuropsychopharmacology*, vol. 26, no. 5, pp. 682–91, May 2002.
 - [141] L. Van Leijenhorst, B. Gunther Moor, Z. a Op de Macks, S. a R. B. Rombouts, P. M. Westenberg, and E. a Crone, "Adolescent risky decision-making: neurocognitive development of reward and control regions.," *Neuroimage*, vol. 51, no. 1, pp. 345–55, May 2010.
 - [142] R. Cabeza, "Cognitive neuroscience of aging: contributions of functional neuroimaging.," *Scand. J. Psychol.*, vol. 42, no. 3, pp. 277–86, Jul. 2001.
 - [143] A. C. Rosen, M. W. Prull, R. O'Hara, E. A. Race, J. E. Desmond, G. H. Glover, J. A. Yesavage, and J. D. E. Gabrieli, "Variable effects of aging on frontal lobe contributions to memory.," *Neuroreport*, vol. 13, pp. 2425–2428, 2002.
 - [144] D. Friedman, "Cognition and aging: a highly selective overview of event-related potential (ERP) data.," *J. Clin. Exp. Neuropsychol.*, vol. 25, pp. 702–720, 2003.
 - [145] R. Cabeza, S. M. Daselaar, F. Dolcos, S. E. Prince, M. Budde, and L. Nyberg, "Task-independent and task-specific age effects on brain activity during working memory, visual attention and episodic retrieval," *Cereb Cortex*, vol. 14, pp. 364–375, 2004.
 - [146] E. Koechlin and A. Hyafil, "Anterior prefrontal function and the limits of human decision-making.," *Science*, vol. 318, no. 5850, pp. 594–8, Oct. 2007.

- [147] P. W. Burgess, I. Dumontheil, and S. J. Gilbert, "The gateway hypothesis of rostral prefrontal cortex (area 10) function.," *Trends Cogn. Sci.*, vol. 11, no. 7, pp. 290–8, Jul. 2007.
- [148] L. K. Fellows, "Deciding how to decide: ventromedial frontal lobe damage affects information acquisition in multi-attribute decision making.," *Brain*, vol. 129, no. Pt 4, pp. 944–52, Apr. 2006.
- [149] L. K. Fellows and M. J. Farah, "The role of ventromedial prefrontal cortex in decision making: judgment under uncertainty or judgment per se?," *Cereb. Cortex*, vol. 17, no. 11, pp. 2669–74, Nov. 2007.
- [150] A. Hänsel and R. von Känel, "The ventro-medial prefrontal cortex: a major link between the autonomic nervous system, regulation of emotion, and stress reactivity?," *Biopsychosoc. Med.*, vol. 2, p. 21, Jan. 2008.
- [151] D. Knoch, L. R. R. Gianotti, A. Pascual-Leone, V. Treyer, M. Regard, M. Hohmann, and P. Brugger, "Disruption of right prefrontal cortex by low-frequency repetitive transcranial magnetic stimulation induces risk-taking behavior.," *J. Neurosci.*, vol. 26, pp. 6469–6472, 2006.
- [152] S. M. McClure, D. I. Laibson, G. Loewenstein, and J. D. Cohen, "Separate neural systems value immediate and delayed monetary rewards.," *Science*, vol. 306, pp. 503–507, 2004.
- [153] S. C. Tanaka, K. Doya, G. Okada, K. Ueda, Y. Okamoto, and S. Yamawaki, "Prediction of immediate and future rewards differentially recruits cortico-basal ganglia loops.," *Nat. Neurosci.*, vol. 7, pp. 887–893, 2004.
- [154] M. Gardner and L. Steinberg, "Peer influence on risk taking, risk preference, and risky decision making in adolescence and adulthood: an experimental study.," *Dev. Psychol.*, vol. 41, pp. 625–635, 2005.
- [155] M. Powell and D. Ansic, "Gender differences in risk behaviour in financial decision-making: An experimental analysis," *J. Econ. Psychol.*, vol. 18, no. 6, pp. 605–628, Nov. 1997.
- [156] C. Harris, M. Jenkins, and D. Glaser, "Gender differences in risk assessment: Why do women take fewer risks than men," *Judgm. Decis. Mak.*, vol. 1, no. 1, pp. 48–63, 2006.
- [157] S. Fecteau, A. Pascual-Leone, D. H. Zald, P. Liguori, H. Théoret, P. S. Boggio, and F. Fregni, "Activation of prefrontal cortex by transcranial direct current stimulation reduces appetite for risk during ambiguous decision making.," *J. Neurosci.*, vol. 27, pp. 6212–6218, 2007.

- [158] B. Eppinger, L. E. Nystrom, and J. D. Cohen, "Reduced sensitivity to immediate reward during decision-making in older than younger adults.," *PLoS One*, vol. 7, no. 5, p. e36953, Jan. 2012.
- [159] T. D. Wager, K. L. Phan, I. Liberzon, and S. F. Taylor, "Valence, gender, and lateralization of functional brain anatomy in emotion: A meta-analysis of findings from neuroimaging," *Neuroimage*, vol. 19, pp. 513–531, 2003.
- [160] J. Deakin, M. Aitken, T. Robbins, and B. J. Sahakian, "Risk taking during decision-making in normal volunteers changes with age.," *J. Int. Neuropsychol. Soc.*, vol. 10, no. 4, pp. 590–8, Jul. 2004.
- [161] G. Strangman, D. A. Boas, and J. P. Sutton, "Non-invasive neuroimaging using near-infrared light," *Biological Psychiatry*, vol. 52, pp. 679–693, 2002.
- [162] D. Meunier, S. Achard, A. Morcom, and E. Bullmore, "Age-related changes in modular organization of human brain functional networks.," *Neuroimage*, vol. 44, pp. 715–23, 2009.
- [163] J. S. Damoiseaux, C. F. Beckmann, E. J. S. Arigita, F. Barkhof, P. Scheltens, C. J. Stam, S. M. Smith, and S. A. R. B. Rombouts, "Reduced resting-state brain activity in the "default network" in normal aging," *Cerebral cortex (New York, NY : 1991)*, vol. 18, pp. 1856–1864, 2008.
- [164] Z. Liu, L. Ke, H. Liu, W. Huang, and Z. Hu, "Changes in topological organization of functional PET brain network with normal aging.," *PLoS One*, vol. 9, no. 2, p. e88690, Jan. 2014.
- [165] G. Gong, P. Rosa-Neto, F. Carbonell, Z. J. Chen, Y. He, and A. C. Evans, "Age- and gender-related differences in the cortical anatomical network.," *J. Neurosci.*, vol. 29, no. 50, pp. 15684–93, Dec. 2009.
- [166] Y. He and A. Evans, "Graph theoretical modeling of brain connectivity.," *Curr. Opin. Neurol.*, vol. 23, no. 4, pp. 341–50, Aug. 2010.
- [167] L. Astolfi, F. De Vico Fallani, F. Cincotti, D. Mattia, M. G. Marciani, S. Bufalari, S. Salinari, A. Colosimo, L. Ding, J. C. Edgar, W. Heller, G. A. Miller, B. He, and F. Babiloni, "Imaging functional brain connectivity patterns from high-resolution EEG and fMRI via graph theory," *Psychophysiology*, vol. 44, pp. 880–893, 2007.
- [168] J. D. Power, D. A. Fair, B. L. Schlaggar, and S. E. Petersen, "The Development of Human Functional Brain Networks," *Neuron*, vol. 67, pp. 735–748, 2010.
- [169] D. M. Long, "Networks of the Brain," *Neurosurgery Quarterly*, vol. 21, p. 144, 2011.

- [170] S. Achard, R. Salvador, B. Whitcher, J. Suckling, and E. Bullmore, "A resilient, low-frequency, small-world human brain functional network with highly connected association cortical hubs.," *J. Neurosci.*, vol. 26, pp. 63–72, 2006.
- [171] J. R. Andrews-Hanna, A. Z. Snyder, J. L. Vincent, C. Lustig, D. Head, M. E. Raichle, and R. L. Buckner, "Disruption of Large-Scale Brain Systems in Advanced Aging," *Neuron*, vol. 56, pp. 924–935, 2007.
- [172] C. L. Grady, M. V Springer, D. Hongwanishkul, A. R. McIntosh, and G. Winocur, "Age-related Changes in Brain Activity across the Adult Lifespan," *J. Cogn. Neurosci.*, vol. 18, pp. 227–241, 2006.
- [173] C. L. Grady, "Cognitive neuroscience of aging," *Annals of the New York Academy of Sciences*, vol. 1124. pp. 127–144, 2008.
- [174] E. Bullmore and O. Sporns, "The economy of brain network organization," *Nature Reviews Neuroscience*. 2012.
- [175] K. Hwang, M. N. Hallquist, and B. Luna, "The development of hub architecture in the human functional brain network," *Cereb. Cortex*, vol. 23, pp. 2380–2393, 2013.
- [176] M. Rubinov and O. Sporns, "Complex network measures of brain connectivity: uses and interpretations.," *Neuroimage*, vol. 52, no. 3, pp. 1059–69, Sep. 2010.
- [177] H. Niu and Y. He, "Resting-State Functional Brain Connectivity: Lessons from Functional Near-Infrared Spectroscopy.," *Neuroscientist*, 2013.
- [178] T. Fekete, F. D. C. C. Beacher, J. Cha, D. Rubin, and L. R. Mujica-Parodi, "Small-world network properties in prefrontal cortex correlate with predictors of psychopathology risk in young children: A NIRS study," *Neuroimage*, vol. 85, pp. 345–353, 2014.
- [179] N. Tzourio-Mazoyer, B. Landeau, D. Papathanassiou, F. Crivello, O. Etard, N. Delcroix, B. Mazoyer, and M. Joliot, "Automated anatomical labeling of activations in SPM using a macroscopic anatomical parcellation of the MNI MRI single-subject brain.," *Neuroimage*, vol. 15, no. 1, pp. 273–89, Jan. 2002.
- [180] G. K. Aguirre, E. Zarahn, and M. D'Esposito, "Empirical Analyses of BOLD fMRI Statistics," *Neuroimage*, vol. 5, no. 5, pp. 199–212, 1997.
- [181] N. U. F. Dosenbach, B. Nardos, A. L. Cohen, D. a Fair, J. D. Power, J. a Church, S. M. Nelson, G. S. Wig, A. C. Vogel, C. N. Lessov-Schlaggar, K. A. Barnes, J. W. Dubis, E. Feczko, R. S. Coalson, J. R. Pruett, D. M. Barch, S. E. Petersen, and B. L. Schlaggar, "Prediction of individual brain maturity using fMRI.," *Science*, vol. 329, no. November, pp. 1358–1361, 2010.

- [182] M. Xia, J. Wang, and Y. He, "BrainNet Viewer: a network visualization tool for human brain connectomics.," *PLoS One*, vol. 8, no. 7, p. e68910, Jan. 2013.
- [183] M. Rubinov and O. Sporns, "Complex network measures of brain connectivity: uses and interpretations.," *Neuroimage*, vol. 52, no. 3, pp. 1059–69, Sep. 2010.
- [184] M. E. J. Newman, "Modularity and community structure in networks.," *Proc. Natl. Acad. Sci. U. S. A.*, vol. 103, pp. 8577–8582, 2006.
- [185] A. Clauset, M. E. J. Newman, and C. Moore, "Finding community structure in very large networks," *Phys. Rev. E*, vol. 70, 2004.
- [186] L. C. Freeman, "A Set of Measures of Centrality Based on Betweenness," *Sociometry*, vol. 40, pp. 35–41, 1977.
- [187] S. Achard and E. Bullmore, "Efficiency and cost of economical brain functional networks.," *PLoS Comput. Biol.*, vol. 3, p. e17, 2007.
- [188] V. Latora and M. Marchiori, "Efficient Behavior of Small World Networks," *Phys. Rev. Lett.*, vol. 87, p. 198701, 2001.
- [189] C. J. Honey, O. Sporns, L. Cammoun, X. Gigandet, J. P. Thiran, R. Meuli, and P. Hagmann, "Predicting human resting-state functional connectivity from structural connectivity.," *Proc. Natl. Acad. Sci. U. S. A.*, vol. 106, pp. 2035–2040, 2009.
- [190] D. S. Bassett and E. Bullmore, "Small-world brain networks.," *Neuroscientist*, vol. 12, pp. 512–523, 2006.
- [191] S. L. Ferradal, a T. Eggebrecht, M. Hassanpour, a Z. Snyder, and J. P. Culver, "Atlas-based head modeling and spatial normalization for high-density diffuse optical tomography: In vivo validation against fMRI," *Neuroimage*, Apr. 2013.
- [192] O. Sporns, G. Tononi, and G. M. Edelman, "Theoretical neuroanatomy and the connectivity of the cerebral cortex," in *Behavioural Brain Research*, 2002, vol. 135, pp. 69–74.
- [193] O. Sporns, G. Tononi, and G. M. Edelman, "Theoretical neuroanatomy: relating anatomical and functional connectivity in graphs and cortical connection matrices.," *Cereb. Cortex*, vol. 10, pp. 127–141, 2000.
- [194] K. Wang, M. Liang, L. Wang, L. Tian, X. Zhang, K. Li, and T. Jiang, "Altered functional connectivity in early Alzheimer's disease: A resting-state fMRI study," *Hum. Brain Mapp.*, vol. 28, pp. 967–978, 2007.
- [195] T. Hedden, K. R. A. Van Dijk, J. A. Becker, A. Mehta, R. A. Sperling, K. A. Johnson, and R. L. Buckner, "Disruption of functional connectivity in clinically

normal older adults harboring amyloid burden.," *J. Neurosci.*, vol. 29, pp. 12686–12694, 2009.

Biographical Information

Lin Li was born on March 19, 1987 in Changde City, Hunan, China. He received the Bachelor of Science degree in Optoelectronic Engineering from Huazhong University of Science and Technology, Wuhan, China, in 2009. In Fall 2009, he started his Doctoral study in Bioengineering Department, the University of Texas at Arlington, Arlington, TX, USA. He is in medical imaging track and under the supervision of Dr. Hanli Liu. His plan is to complete his Doctor of Philosophy in Biomedical Engineering at the joint graduate program of the University of Texas at Arlington and the University of Texas Southwestern Medical Center at Dallas in May 2015. His research interests include functional brain imaging in fMRI, fNIRS and EEG/MEG. He is also interested in the development of image algorithms and image vision techniques.